CHARACTERISATION AND OPTIMISATION OF ALTERNATING CURRENT THIN FILM ELECTROLUMINESCENT DISPLAYS

CARLY FARROW

A thesis submitted in part fulfilment of the requirements of Nottingham Trent University for the degree of Doctor of Philosophy

January 2014

Abstract

This Thesis presents research undertaken to investigate the electro-optical characterisation and optimisation of Thin Film Electroluminescent (TFEL) devices and Laterally Emitting Thin Film Electroluminescent (LETFEL) devices with respect to device lifetime and aging.

Post deposition localised laser annealing as an alternative to thermal annealing has been previously described in the literature. The effects of laser annealing on various devices is investigated and described within this Thesis. In particular, the novel use of ArF laser annealing at a wavelength of 193nm as a post deposition annealing process for ZnS:Mn thin films deposited by RF magnetron sputtering has been presented and compared to KrF laser annealing (248nm wavelength). Additionally the use of KrF laser annealing on a new deposition method, High Target Utilisation Sputtering (HiTUS) is presented, with successful results obtained on heat sensitive substrates. Results presented show that the use of KrF produces slightly better performance in respect to maximum luminance, however the use of ArF laser annealing can allow for achievement of higher luminance at lower applied voltages.

Research is also presented regarding methods for tackling the issue of reduced performance of devices over time. Investigations are undertaken to determine the extent to which the burn-in parameters used affect the lifetime of devices. A series of experiments in which the step-time, voltage and therefore overall burn-in time are altered are described. Results show that the lifetime of the device can be significantly altered by small changes to these parameters, with significant improvements in lifetime observed and described.

As a result of the experiments and analysis described in this Thesis, areas for further research are suggested with the aim of further device optimisation in regards to post deposition heat treatment and the burn-in process.

Acknowledgements

I would first like to thank my director of studies Dr. Demosthenes Koutsogeorgis for not only giving me the opportunity to carry out this project but for also providing me with support, guidance and encouragement throughout, and for also challenging me to further myself. I shall be forever grateful for all that he has helped me to achieve.

I would also like to thank my second supervisors Prof. Wayne Cranton and Dr. Robert Ranson for their advice and guidance during my research, Prof. Clive Thomas for taking the time and interest in my work and for teaching me the fundamentals of solid state physics and Dr. Costas Tsakonas for continually changing his mind and confusing me.

My Colleagues in the Displays Research Group at NTU, Dr. Thomas Miller who was always willing to provide a distraction, Dr. Gabriel Boutaud for all his “helpful” advice, Dr. Sook Voon Yap and Dr. Sharron Wilson who contribute to the lab and office working environment.

Finally I must thank my parents for their encouragement throughout my studies and especially my husband Jonathan for his continuous love and support.

Table of Contents

List of Figures

List of Abbreviations and Symbols

Ω	Ohms
^oC	Degrees Celsius
AC	Alternating Current
ACTFEL	Alternating Current Thin Film Electroluminescence
Al	Aluminium
ALD	Atomic Layer Deposition
ALE	Atomic Layer Expitaxy
Al_2O_3	Aluminium Oxide
Ar	Argon
ArF	Argon Fluoride
ATO	Planar dielectric which consists of Al_2O_3 and TiO_2
BaS:Bi	Barium Sulphide doped with Bismuth
$BaSO_4$	Barium Sulphate
B-V	Brightness-Voltage
C	Coulomb
C_{ins}	Insulator capacitance
cd	Candela
CL	Cathodoluminescence
cm	Centimetre
C_{ph}	Phosphor capacitance
CRT	Cathode Ray Tube
C_s	Sense capacitor
CSC	Charge Storage Capacity
C_{tot}	Total capacitance
Cu	Copper
C-V	Capacitance Vs Voltage
CVD	Chemical Vapour Deposition
DC	Direct Current
D_{ph}	Phosphor thickness
DUT	Device Under Test

EBE	Electron Beam Evaporation
E_{BG}	Band gap
Ec	Conduction band
E_V	Valence band
EL	Electroluminescence
eV	Electron Volt
F	Farads
FED	Field Emission Display
FPD	Flat Panel Display
f_p	Phosphor field
GPIB	General Purpose Interface Bus
H	Hour
Hz	Hertz
ITO	Indium Tin Oxide
kΩ	Kilo ohms
kHz	Kilo hertz
KrF	Krypton fluoride
LA	Laser Annealed
LATA	Laser Annealed – Thermally Annealed
LCD	Liquid Crystal Display
LDBD	Localised Destructive Breakdown Defect
LE	Leading Edge
LED	Light-Emitting Diode
LETFEL	Laterally Emitting Thin-Film Electroluminescence
l(t)	Transient luminance
L-V	Luminance Vs Voltage
m^2	Meter squared
MBE	Molecular Beam Expitaxy
Mn	Manganese
MOCVD	Metal-Organic Chemical Vapour Deposition
MV	Mega volts
n-shift	Negative threshold voltage shift
Ne	Neon

nF	Nano farads
ns	Nano seconds
NTU	Nottingham Trent University
OLED	Organic Light-Emitting Diode
p-shift	Positive threshold voltage shift
Pa	Pascal
pA	Pico Ampere
PDP	Plasma Display Panel
PEN	Planarised Polyethylene Naphthalate
PFG	Programmable Function Generator
PL	Photoluminescence
PLS	Plasma Launch System
PQL	Plasma Quest Ltd.
PVD	Physical Vapour Deposition
R	Resistor
RAL	Rutherford Appleton Laboratory
RF	Radio Frequency
R_s	Sense resistor
RTA	Rapid Thermal Annealing
s	Seconds
SiC	Silicon carbide
SiO_2	Silicon oxide
SRELD	Sunlight Readable Electroluminescent Display
TA	Thermal Annealing
TE	Trailing Edge
TEM	Transmission Electron Microscopy
TFEL	Thin Film Electroluminescence
TFT	Thin Film Transistor
TiO_2	Titanium oxide
TV	Television
UV	Ultra-Violet
V_{app}	Applied voltage
V_{opp}	Opperating voltage

VFD	Vacuum Florescent Display
Vp-p	Peak to peak voltage
V_{th}	Threshold voltage
XeCl	Xenon chloride
Y_2O_3	Yttrium Oxide
ZnS	Zinc Sulphide
ZnS:Mn	Zinc Sulphide doped with Manganese

1. Introduction

1.1 Overview

The past century has seen vast advancements in display technology; electronic displays are now used in a wide range of products and applications from household appliances to watches, car dashboards, mobile devices and televisions (TV). Displays have become an indispensable part of modern day life as the amount of information people are required to process during the day increases. Advancements in technology mean that people are interacting with displays more and more with mobile technologies such as smart phones, hand-held game consoles, tablets and electronic book readers. With such a large market demand and wide usage requirements it is not surprising that a vast number of display technologies exist.

The cathode ray tube (CRT) is the oldest of the display technologies and for many years was the dominant leader in the TV and monitor market due to its reliability and low cost, but due to its limitations (limited screen size, not portable or robust) many flat panel display (FPD) technologies have emerged. FPD display technologies include liquid crystal displays (LCD), plasma display panels (PDP), Field emission displays (FED), Vacuum florescent displays (VFD), inorganic light-emitting diode (LED), organic light-emitting diode (OLED) and thin film electroluminescence (TFEL)(1). LCD technology currently holds the larger market share due to being inexpensive in comparison to other FPDs, however the demand for OLED and other electroluminescent displays is on the increase due to their comparatively superior visual characteristics and potential for low power consumption.

The main focus of this research will be alternating current thin film electroluminescence (ACTFEL); whilst this technology does not have a large presence in the displays market; it enjoys success in certain niche markets where its brightness, wide viewing angles, high contrast and robustness make it very popular for military and medical applications.

The conventional TFEL device structure consists of a light emitting phosphor layer sandwiched between two insulating layers which are in turn sandwiched between a top transparent and a bottom opaque electrode. An alternative device structure, using micro-mirrors, reflecting the lateral emission of the phosphor layer to the surface demonstrates the feasibility of high intensity light emission from miniature displays (2). These displays have the potential to be used in head mounted systems where the required luminance is in excess of 3000cd/m^2 and full graphics are not necessary. Such devices could be used in applications for personal sports trackers, motorbike helmets and even riot police to relay simple instructions. In order to maintain the high luminance required to be able to see the displayed information over bright sunlight, the device must be stable and therefore demonstrate minimal aging behaviour.

Technology	Advantages	Disadvantages
CRT	Mature Inexpensive Excellent colour and Contrast High resolution Stable pictures Bright and clear Reliable	High power consumption Heavy, bulky and large depth Prone to misconvergence which leads to poor contrast Produces harmful electromagnetic radiation Single electron beam can misfocus
PDP	Excellent colour reproduction High viewing angle Good contrast Suited for large displays, up to 2m	Fairly heavy Fragile High power consumption Screen burn in Poor going from black to white Limited life span (10,000 hours)
LCD	Thin and lightweight (LCD TFT being even thinner) Good colour and sharpness No screen burn in Excellent life span Low power consumption	Fixed resolution Poor contrast ratios Cannot display dark blacks Non emissive Slow refresh rate/pixel switching Narrowing viewing angle Limited operating environment
LED	Mature Bright	High power consumption High resolution - high cost Expensive blue light
OLED	High viewing angle Fast response times Excellent brightness & colour Low power consumption Very thin Inexpensive Possible flexible substrates	Poor life span Brightness reduces over life span Sensitive to environment (air and water) Blue pixel life span shorter than red and green pixels
VFD	Bright High efficiency High reliability Small displays - small cost	Monochrome Large displays mean large cost
TFEL	Very thin Long life span Bright High resolution Robust High Speed Solid State	Expensive Not full colour
LETFEL	High brightness Very thin Low Power consumption	Monochrome

Table 1.1 - Comparison of display technologies (1, 3, 4)

The first section of this thesis presents the results of a study of post deposition laser annealing of ZnS:Mn using different laser wavelengths, 193 and 248nm, and different deposition methods: RF magnetron sputtering and High Target Utilisation Sputtering (HiTUS). It presents the feasibility of producing high luminance transparent flexible displays using room temperature HiTUS deposition combined with localised post deposition laser annealing treatment.

The second section presents the results of a study into the effect of the burn-in parameters on the lifetime and aging of LETFEL displays, the optimal micro-mirror structure of LETFEL displays is also investigated. The step time interval and the voltage increment are altered in order to determine the optimal parameters in order to extend the lifetime of a device as well as reduce the aging in order to produce a more stable device.

1.2 Aim

The aim of the research undertaken for this thesis is to investigate the electro-optical characterisation and optimisation of thin film electroluminescent devices. This involves the study of the burn-in drive parameters in order to increase the lifetime and the effects on the aging behaviour. Also different post deposition heat treatments and deposition methods are studied.

1.3 Objectives

Determine the feasibility of laser annealing ZnS:Mn for use in ACTFEL devices at a wavelength of 193nm and compare the electrical device performance with devices laser annealed at 248nm.

Investigate the influence laser annealing has on the characteristics of devices grown by different deposition methods and with different dielectric materials deposited on transparent substrates.

Improve the understanding of ACTFEL device operation by developing experimental characterisation systems and protocols.

Identify the ideal LETFEL device structure as a function of device performance and aging. Investigate the effects of the electrical drive parameters in order to optimise the lifetime of the devices.

1.4 Thesis Structure

Chapter 2 will provide the background information required for the study undertaken. A brief history of electroluminescence (EL) is presented as well as ACTFEL device physics, deposition and annealing processes used and finally a review on aging and its causes.

Chapter 3 details the experimental equipment and techniques used during the undertaking of this research – these include the electrical and optical characterisation methods, deposition systems for ACTFEL device fabrication and laser annealing.

The fourth chapter presents and analyses the results obtained from samples fabricated by RF magnetron sputtering and laser annealed. The feasibility of laser annealing ZnS:Mn at a previously unreported wavelength of 193nm is demonstrated and directly compared to 248nm.

Chapter 5 presents an investigation on devices that have been fabricated using a new low temperature deposition method and demonstrates the potential to use laser annealing as a post deposition annealing process on temperature sensitive substrates.

The work presented in chapter 6 focuses upon the optimisation of the burn-in parameters of LETFEL displays in order to prolong the lifetime and reduce the aging characteristics in order to obtain a more stable device.

The final chapter describes the conclusions drawn for the research carried out, it summarises what achievements have been made during this time, and it also details how the body of work could potentially be continued.

2. Background

2.1 Introduction

As outlined in Chapter 1, this chapter presents the background information required to understand basic ACTFEL principles and the technical discussions that will follow. A history of luminescence is presented first along with the different types of electroluminescence (EL). Secondly, a typical ACTFEL structure and device physics are discussed, this will be followed by a description of various deposition methods and post deposition annealing techniques. Finally, there will be a review on aging and its causes.

2.2 Luminescence

2.2.1 A Short History

Naturally occurring luminance has been known of since the dawn of man, it was an amateur Italian alchemist Vincenzo Cascariolo, who heated in a coal furnace what is believed to be $BaSO_4$ in the hope of producing noble metals from base metals, he failed and instead produced the first creation of artificial luminance. He created a sun stone, BaS:Bi, that glowed blue at night and recharged in the sunlight (5), this material along with others being discovered were named phosphors, Greek for light bearer, and the glow was termed phosphorescence. The term *luminescenz* was first used by Eilhardt Wiedemann, a German physicist, in 1888 to describe the “development of light in which an illumination is produced through external causes without an apparent rise in temperature" (6). During the 1920s and 30s R. W. Pohl, a German solid state physicist, developed the configurational coordinate model of the luminescent centre, this model forms the basis of modern theory (7). There are three types of luminescence in respect to display technology; cathodoluminescence (CL), photoluminescence (PL) and electroluminescence (EL). It is EL that is of relevance to this study.

2.2.2 Electroluminescence

EL is described as the process by which a material generates non-thermal radiation from the excitation of an electron (8) as a result of the application of an electric field (9). EL was first observed in silicon carbide (SiC) by Captain Henry Joseph Round in 1907 (10), then in 1936 French physicist Georges Destriau observed the emission of light from Zinc Sulphide (ZnS) powder suspended in oil on glass sheets when an alternating current (AC) was passed through it (11). This method of producing light has been used as the basis of many modern phosphor based display panels. There are two classes of EL devices; with the first class, light is generated by electron-hole pair recombination near a pn junction, LEDs are an example of this kind of class. The second class of EL devices, which is the relevant class to this report, generates light by impact excitation of a light emitting centre called an activator, by high energy electrons. A high electric field is applied across the device, in the region of 10^8 V/m, in order for the electrons to gain the high energy required to generate light from impact excitation of a luminescent center, for this reason this type of EL is often referred to as high-field electroluminescence (9).

Four types of EL device have been developed, they are characterised by the drive voltage and the structure of the phosphor layer;

- Alternating current thin-film EL
- AC powder EL
- Direct current (DC) thin-film EL
- DC powder EL

As the name would suggest, the phosphor layer in the powder devices is exactly that, powder, whilst the phosphor layer in the thin-film devices is deposited using a thin-film deposition process. The development of a transparent electrode (SnO_2) in 1950 prompted worldwide research into powder devices which continued up until the early 60s when their limitations were realised; short lifetimes and low luminance. The research into powder devices at this point gave way to thin-film EL due to advancements in thin-film deposition methods which produced a ZnS device doped with manganese (Mn) with a greater luminance output with respect to voltage (12). In 1962 Edwin Soxman of Servomechanisms demonstrated the first TFEL display matrix, the single insulator ZnS:Mn based display, which is the predecessor to today's TFEL displays. Since Sharp demonstrated a stable EL display panel in 1974 a significant amount of research has been carried out into TFEL displays (13).

TFEL displays are solid state and as such are very robust; they demonstrate high contrast, large viewing angle, and high resolution and are capable of operating at extreme temperatures (-40 to +85°C) which makes them ideal for use in the military, medical and transport sectors.

2.3 Semiconductor Physics

The emitting layer in ACTFEL devices is typically a wide bandgap semiconductor. In order to aid in the understanding of the basic operation of ACTFEL devices some fundamental semiconductor physics must first be presented.

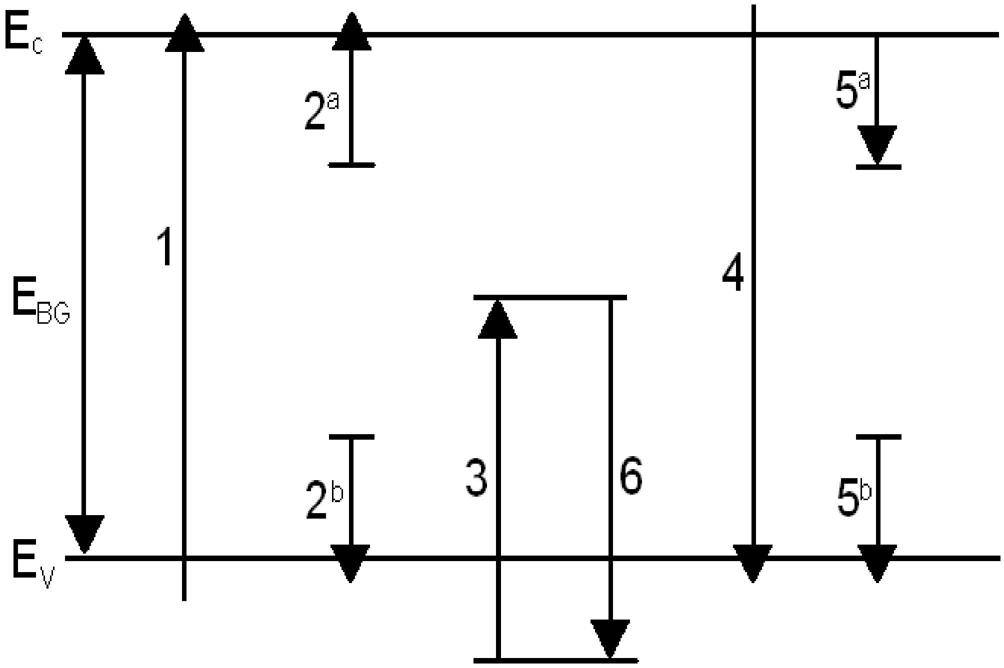

Figure 2.1 - Important electronic transitions in semiconductor devices; [1] band to band impact ionisation, [2] trap to band impact ionisation and [3] impact excitation

A simplified energy band diagram, as shown in Figure 2.1, can be used to show the operation of an ACTFEL device, where E_v is the maximum position of the valence band and E_c is the minimum position of the conduction band of the semiconductor as a function of position along an axis within the crystal. E_{BG} is the band gap energy and is shown as the difference of electron potential energy between the valence and the conduction band, with the energy increasing from E_v towards E_c.

Figure 2.1 shows three possible methods of electron transition, all of these methods require energy to be given to the electron, there are two possible sources of this energy. Firstly it can be absorbed from an impinging photon of light or an energetic electron or secondly it may come from the thermal energy associated with lattice vibrations which increase in amplitude as the temperature of the semiconductor increases.

Transition 1, as depicted in Figure 2.1, shows an electron travelling from the valence band straight to the conduction band, in order to do this the energy applied to the electron must be greater than E_{BG}. For the purpose of this study the value is 3.6eV, as the wide bandgap semiconductor material used is ZnS:Mn. Once the electron is in the conduction band it may move within it, either due to the application of an electric field, or, even if no electric charge is applied, by means of diffusion current which is generated by non-uniform densities of electrons or holes. Both forces act in a similar manner (14). When an electron vacates the valence band a hole is created, this positively charged vacancy can move within the valence band under the same mechanisms as the electron moves within the conduction band. When transition 1 is caused by a sufficiently energetic electron, it is known as ‘band to band impact ionisation’. This is a very common method, even with the typically large bandgap present in the semiconductors used for ACTFEL devices.

When impurities are introduced into the semiconductor crystal, whether intentional or not, additional states can be created within the forbidden band gap. Transition 2^a demonstrates this factor showing emission of an electron to the conduction band via a mid-band gap impurity, it also leaves behind an ionised trap.

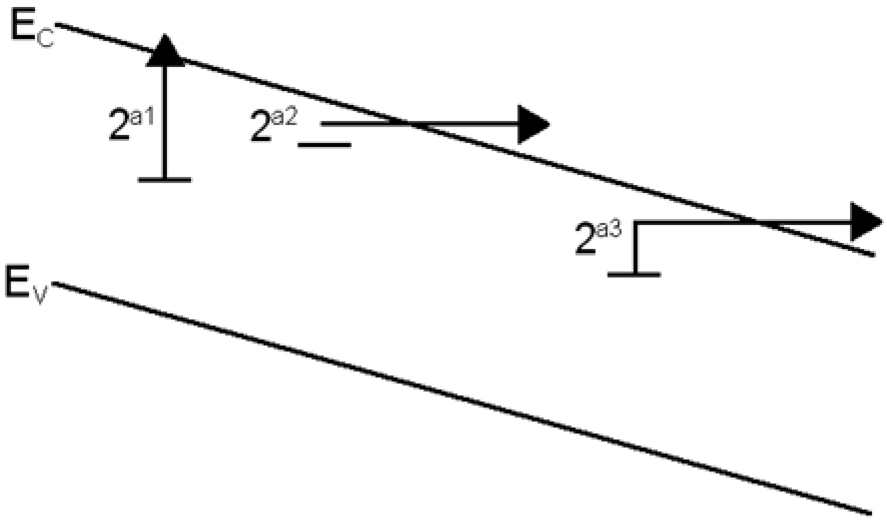

Figure 2.2 - Methods of electron emission from trap level to conduction band; (2^{a1}) thermal energy, (2^{a2}) tunnel horizontally and (2^{a3}) combination of thermal energy and horizontal tunnelling.

There are four possible ways that the electron transition can occur, as depicted in Figure 2.2. Firstly, through photon absorption; enough thermal energy could be gained in order to allow transition of the electron from the trap to the conduction band (2^{a1}). Secondly, the electron could tunnel horizontally to the conduction band (2^{a2}). Thirdly, a combination of the previous two could occur; the electron gaining thermally energy from the lattice vibrations and then tunnelling horizontally to the conduction band through a narrower barrier, this process is known as phonon assisted tunnelling (2^{a3})(15). Finally, it is also possible for emission to occur by an electron colliding with the trap, this method is known as the trap to band impact ionisation. The transition 2^b shows what can either be the emission of a hole from the trap level to the valence band or a trap capturing an electron from the valence band.

Transition 3 is different to the previous two transitions, as usually it involves a single atom; the electron. In an excited state the electron has enough energy to leave the valence band but is not emitted to the conduction band, instead it remains bound to the atom. When this occurs through absorption of energy from and excited electron it is known as impact excitation.

The other transitions denoted on Figure 2.1 are the reverse of the previous three transitions; transition 4 shows a conduction band electron recombining with a valence band hole, transition 5^a shows a conduction band electron being captured by a trap, while 5^b shows a valence band hole being captured by a trap and transition 6 shows the excited electron atom relaxing down back to the valence band.

2.4 Thin-Film Electroluminescence

2.4.1 ACTFEL Device Structure

The structure of an ACTFEL devices consists of, as the name would suggest, thin films stacked upon one another. These are deposited sequentially and usually form a symmetrical sandwich configuration. A simple ACTFEL device can be fabricated by sandwiching a phosphor layer between two electrodes, one of which is transparent, and applying a high electric field across them. This structure, however, is unreliable as any defects in the phosphor layer would cause a short circuit leading to a destructive amount of energy to be dissipated through the device (16). In order to overcome this limitation, a new device structure was proposed by Russ and Kennedy (17), a double insulating structure consisting of metal – insulator – phosphor – insulator – metal (MISIM), which can be seen in Figure 2.3. Since Inoguchi (18) reported devices with very long lifetimes using this structure it has gained wide acceptance and popularity. The insulating layers of this structure protect the phosphor layer and stop the device from short circuiting even if there are defects within the phosphor layer.

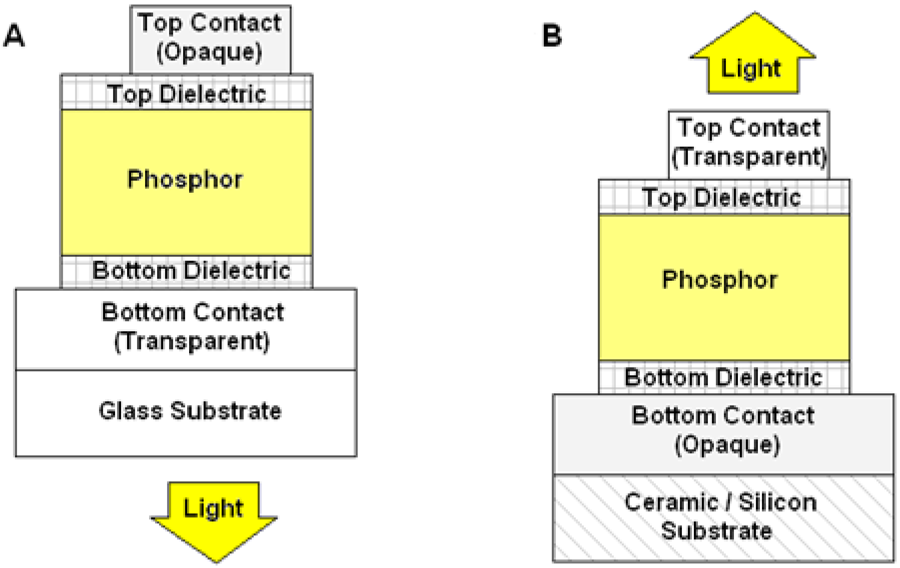

Figure 2.3 - TFEL Structure, (A) standard structure and (B) inverted structure

The standard structure, shown in Figure 2.3A, has the light emitting phosphor layer sandwiched in between the dielectric insulating layers which are then sandwiched by the two conducting electrode layers. This stack is deposited on a transparent substrate, usually glass; the bottom electrode is also transparent and is usually made from indium tin oxide (ITO). With the standard structure the emitted light is viewed through the transparent substrate. With the exception of the substrate, all the individual layers of the thin film have a thickness in the region of hundreds of nm. The standard structure can be inverted, as shown in Figure 2.3B, with the top electrode being transparent. The inverted structure is fabricated on an opaque substrate, usually silicon or ceramic, and the light is emitted from the top.

The requirements of the device will usually determine which of the structures is used, for this study it was the inverted structure, this was due in main to the post deposition annealing that was required which cannot be done with a glass substrate due to occurrences of deformation. The thermal annealing carried out during this study, at temperatures up to 550°C, can cause the surface of the glass substrates to warp and therefore creates rough uneven surfaces.

2.4.2 Laterally Emitting Thin-Film Electroluminescence

Most of the research carried out in the area of TFEL displays with a focus on improving the luminance have been done by investigating; alternative phosphors, deposition techniques and post deposition processes. The research group at Nottingham Trent University (NTU) in association with The Rutherford Appleton Laboratory (RAL) developed an alternative device structure. This device structure, known as laterally emitting thin-film electroluminescence (LETFEL) has demonstrated high intensity emission and is an improvement on the conventional TFEL structure (19, 20). In a conventional TFEL structure the emitted light is output perpendicular to the surface of the film, passing through the insulator and transparent electrode. In 1984 D. H. Smith discovered that a vast majority of the light generated within the phosphor layer of a TFEL device is trapped and is reflected sideways (21). The intensity of the light emitted at the edges of the phosphor layer is considerably greater that that emitted through the surface (22) this is due to the phosphor layer having a refractive index much higher than the insulating layers. This generates a step index structure that can be an efficient light guide. It is estimated that as much as 90% of the surface emission is lost due to internal reflections. The novel LETFEL structure makes use of this high intensity light by incorporating micro-mirrors into the structure which reflect the light towards the surface, as shown in Figure 2.4, resulting in significantly enhanced light output (23). By using the lateral emission of the device this novel structure can produce a light emission four times greater than that of a conventional TFEL device (24, 25).

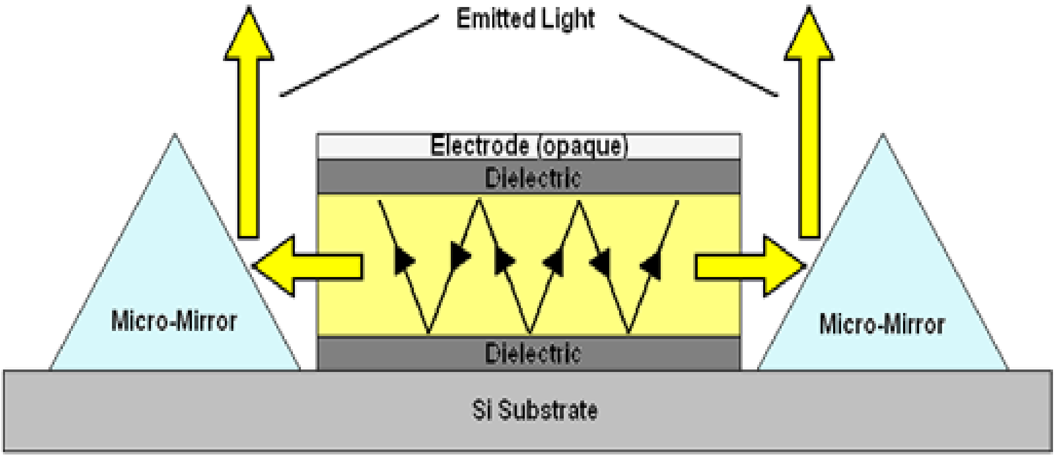

Figure 2.4 - LETFEL light emission schematic

2.4.3 Device Operation

Light is emitted from a device when a sufficient voltage, the threshold voltage (V_{TH}), is applied to the electrodes. Below this voltage the phosphor layer behaves like a dielectric, and as such, the device acts like a capacitor as there are no conduction charges flowing through the device. The total capacitance of the device is calculated by the phosphor (C_{ph}) and both the dielectric (C_{ins}) layers capacitances in series.

$$C\text{tot} = \frac{CinsCph}{Cins + Cph} \tag{2.1}$$

The electric field is dropped across the phosphor and dielectric layers in accordance to the voltage divider calculated by the capacitances of the individual layers. The field in the phosphor layer is calculated by:

$$fp = \frac{Cins}{Cins + Cph}\frac{Vapp}{Dph} \tag{2.2}$$

Where V_{app} is the applied voltage and D_{ph} is the thickness of the phosphor layer.

As the applied voltage is increased beyond the threshold voltage, the device no longer behaves as a capacitor and charge begins to flow within the phosphor layer and light emission may be observed. At this stage the operation of the device can be explained using the principles outlined in section 2.3, as Figure 2.5 demonstrates (26, 27).

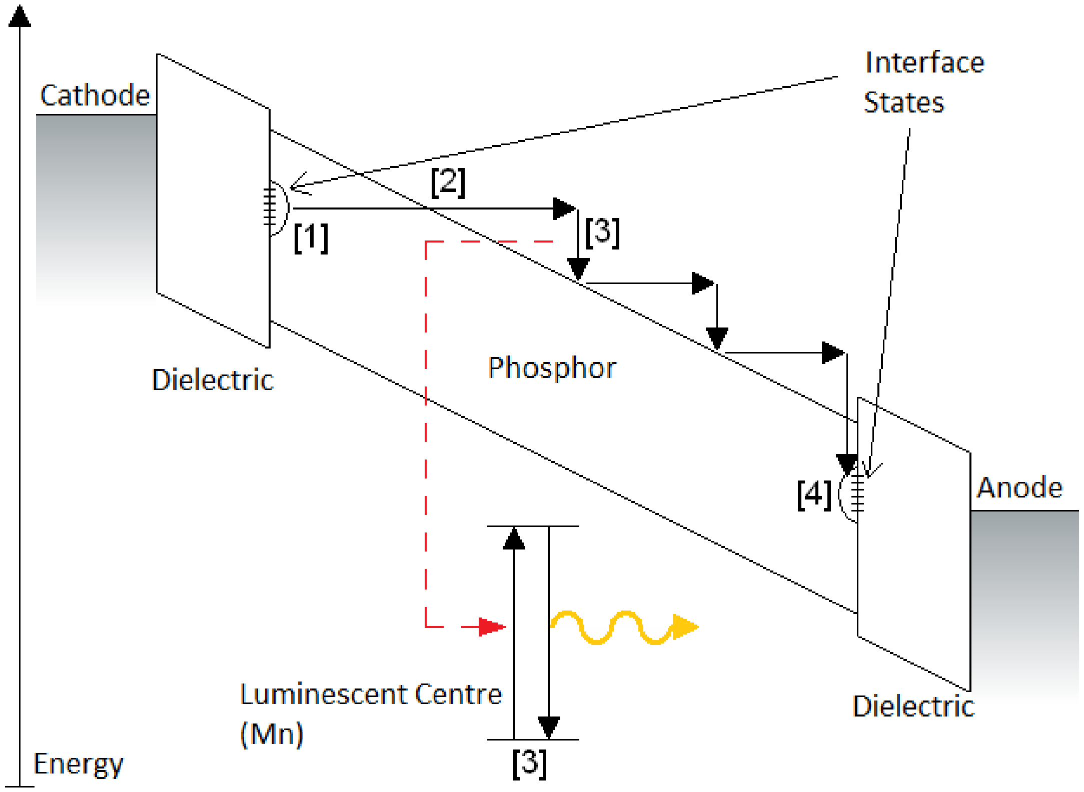

Figure 2.5 - Energy Band Diagram of Double Insulating TFEL Device

The main sources of electrons are located in the interface states situated between the phosphor and the insulator. These states are created in the phosphor band gap, due to the atomic level disorder between the two materials. Above the threshold voltage the phosphor field is large enough that electrons trapped in the cathode interface states are injected into the phosphor conduction band by means of high field assisted tunnelling as depicted by process [1] in Figure 2.5. The injected electrons drift across the phosphor layer gaining kinetic energy from the electric field. As these electrons accelerate through the phosphor, collisions may occur between the electrons and the luminescent centres of the added impurity. In this study the impurity is manganese, [2]. When these collisions occur, if the electron has sufficient kinetic energy to be a hot electron, energy will be transferred to the impurity and it will excite the luminescent centre from its ground state to its excited state [3]. This excitation is a result of direct impact excitation of a hot electron with the activator ion (Mn++) in the luminescent centres. Light is emitted through photon emission when the excited electron of the luminescent centre relaxes radiaitvely from its excited state back to the ground. Alternatively, a non-radiative process could occur when a phonon is instead emitted. The electron will continue to travel across the phosphor layer gaining more kinetic energy, and, possibly be subjected to more collisions before finally being trapped at the phosphor – insulator interface states at the anode [4]. The polarity of the alternating voltage is then reversed and the process begins again.

The processes outlined above are essential for continuous ACTFEL device operation and in an ideal device these processes would occur without any changes to the characteristics, efficiency and operation. The main cause of deviation from the theoretical operation is space charge which is discussed in section 2.7.

2.4.4 Material Requirements

The materials used for ACTFEL fabrication are an important factor to consider as they can determine the operational characteristics of the device and causes of device failure. The essential qualities that the insulator and phosphor materials should possess are discussed in this section.

2.4.4.1 Dielectric Materials

The primary role of the dielectric layer is to protect the phosphor layer from destructively large currents when electrical breakdown occurs; therefore it is important that there are no significant defects over large areas which could lead to breakdown (9). Dielectric breakdown has two modes of failure, the first is propagating breakdown where a small electrical breakdown occurs in the dielectric layer and propagates out causing catastrophic breakdown of the entire EL stack. The second mode is self-healing breakdown where again a small electrical breakdown occurs but with self-healing the breakdown remains localised, self-healing occurs as the leakage current in the defect channel produces heat which melts the surrounding material filling the void. The dielectric layer is a capacitor in series with the phosphor layer with a fraction of the voltage dropping across the dielectric; therefore the dielectric capacitance influences the threshold voltage required for tunnelling to occur (28). The dielectric layer provides the current limitation necessary for preventing device failure during normal operation and therefore prolongs the life of the device. As the stability of an ACTFEL device is directly related to the dielectric layer it is important to use a high quality insulating material. The properties of an optimal ACTFEL dielectric material required to produce a reliable and efficient device are as follows (9, 29):

- Large dielectric constant ε_r
- Large breakdown field E_{bd}
- Few pinholes and defects
- Good layer adhesion

Small loss tangent tanδ (measure of dissipative characteristics defined by 1/(2πfCR). f is the drive frequency, C is the capacitance and R is the resistance of the insulating layer). A large loss tangent implies that charge is leaking through the insulators therefore reducing efficiency by increasing power consumption (30).

There are several other desired properties for dielectric materials such as; high refractive index, high resistivity, good barrier properties, moisture resistance, to be able to withstand mechanical and thermal stress during device operation, good insulator/phosphor electronic interface properties and low leakage current in the order of picoAmpere at the operating voltage (31). The most important of all these requirements are the dielectric constant and breakdown strength; it is the product of these two properties that gives the charge storage capacity (CSC);

$$CSC = \varepsilon r \varepsilon o Ebd \tag{2.3}$$

Where ε_r is the relative dielectric constant of the material, ε_o is the permittivity of vacuum given to be 8.8542 x 10^{-12} F/m and E_{bd} is breakdown field strength of the material. The breakdown field strength is calculated by;

$$Ebd = \frac{Vbd}{d} \tag{2.4}$$

where V_{bd} is the breakdown voltage and d is the thickness of the dielectric layer.

The CSC value is one of the generally accepted figures of merit in deciding the best material for use as a dielectric, it needs to be at least 3 times that of the phosphor layer, therefore it must exceed 3µC cm^2 for ZnS:Mn which has a CSC of 1µC cm^2 (32). Table 2.1 consists of a summary of important parameters for some of the possible dielectric materials for use in ACTFEL devices.

During this study three dielectric materials have been used in the tested devices, these are yttrium oxide (Y_2O_3) and silicon oxide (SiO_2) both deposited using RF Magnetron sputtering. The third is a Planar dielectric which consists of titanium oxide (TiO_2) and aluminium oxide (Al_2O_3), known as ATO, which is deposited using ALD.

Material	Relative Dielectric Constant	Breakdown Strength (MV/cm)	Charge Storage Capacity (CSC)	Refractive Index	Energy Band gap (eV)
SiO_2	3.9	10	3.45	1.4 – 1.5	8.9
Si_3N_4	7.5	10	6.64	2.1	5.1
$BaTiO_3$	300 – 2000	0.42	42.77	2.4	2.5 – 3.9
Y_2O_3	10 – 18	3.85	4.77	1.9	5.6
Al_2O_3	8.5 – 10	7	5.73	1.5	8.7
Ta_2O_5	25	4.5	9.96	2.2 – 2.5	4.2
ZrO_2	25	4	8.85	1.27 – 1.92	7.8
TiO_2	80	3	21.25	1.95 – 2.5	3.5
HfO_2	25	1 - 2	3.32	2.1	5.7

Table 2.1 - A summary of electrical and optical properties for dielectric materials which can be used in ACTFEL devices (28, 33-35). The values listed are a guideline as they are dependent upon the deposition parameters.

2.4.4.2 Phosphor Materials

A phosphor layer within an ACTFEL device consists of the host material (ZnS) and an integrated light emitting dopant (Mn) known as an activator or luminescent centre. The requirements for these materials are summarised from Boutaud and Ono (9, 36).

Host Materials

- The material should have the best possible crystalline structure, for ZnS this would be a hexagonal wurtzite crystal structure, in order to permit the electrons to accelerate to a high enough kinetic energy for impact excitation. Also the material must be able to withstand post deposition annealing temperatures of 550^{o}C.
- In order for efficient light emission to arise, the luminescent centres should be incorporated into substitutional lattice sites. If this does not occur, the probability that the excited luminescent centre will lose its energy non-radiatively to a nearby lattice defect is increased.
- The material must have a large enough band gap to be able to emit visible light from the luminescent centres without significant absorption. Materials used in EL devices typically have a band gap of between 3 and 4.5eV.
- The material must be able to hold a high electric field in the order of 10^{8} V/m without electric breakdown and it must have insulating characteristics below the threshold voltage.
- The typical doping level of luminescent centres in an EL host material is in the order of 1%. In order to keep the high level crystalline structure it is important that both the geometric size and valence of the cation is matched with the dopant.

Luminescent Centres

- The luminescent centres must be properly incorporated into the host material and emit visible light.
- They should have a large enough cross section for impact excitation.
- They must be stable in high electric fields in the order of 10^8 V/m, dopants such as copper (Cu) that have previously been used successfully with ZnS in CRT applications are not suitable for TFEL. This is due to the shallow donor and acceptor levels associated with the Cu doping of ZnS being unstable in high electric fields because electrons can tunnel out, Mn levels are much deeper preventing this from occurring.

2.5 Deposition Methods

Production of ACTFEL devices is dependent upon the ability to manufacture the thin films by a controlled and repeatable process. The thickness, uniformity, surface roughness and crystallinity must meet with specific criteria. The deposition of the thin film layers involves the redistribution of matter from a source material onto a remote substrate; the process in which the material is removed from the source and transported to the substrate distinguishes the deposition method. The deposition methods can be categorised into two different groups, physical vapour deposition (PVD) and chemical vapour deposition (CVD). With PVD methods the source material generates a vapour by a physical process which is transported though vacuum onto the substrate, evaporation, molecular beam epitaxy (MBE), and sputtering are examples of PVD methods. With CVD the thin film is grown as a result of a chemical reaction from gases released into the chamber which react at the surface of the substrate, atomic layer deposition (ALD), metal-organic chemical vapour deposition (MOCVD) and plasma enhanced chemical vapour deposition (PECVD) are all types of CVD methods. The three methods used during this study; ALD, evaporation and sputtering are detailed in this section.

2.5.1 Atomic Layer Deposition (ALD)

Atomic layer deposition formerly known as atomic layer expitaxy (ALE) is a popular deposition method for ACTFEL thin films. The method was created by Tuomo Suntola in Finland 1974 for the deposition of ZnS (37). The principle of ALD is based upon the sequential pulsing of special precursor vapours; each pulse of the vapours creates one atomic layer. Two precursor vapours are used for each material deposited, for ZnS the two precursors commonly used are zinc chloride ($ZnCl_2$) and hydrogen sulphide (H_2S), doping is achieved by replacing a fraction of the $ZnCl_2$ pulses with a suitable manganese containing precursor such as $MnCl_2$ (38).

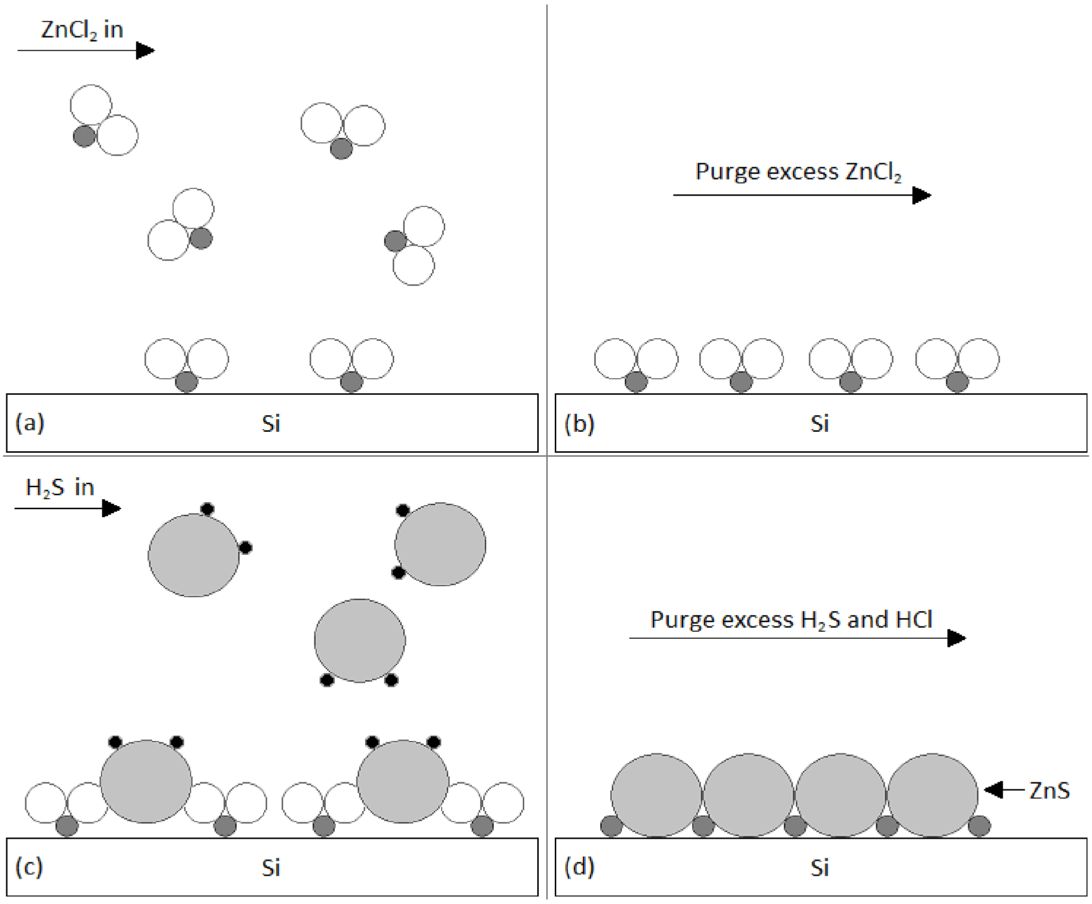

Figure 2.6 - Atomic layer deposition of a single monolayer of ZnS (9)

The ALD process uses reactant gases to deposit the thin films onto a heated substrate, but, unlike other CVD methods, the reactant precursors are pulsed sequentially into the reaction chamber. The ALD process for depositing a layer of ZnS is dependent upon the following reaction:

$$ZnCl_2 + H_2S \rightarrow ZnS + 2HCl \qquad (2.5)$$

The deposition, as shown in Figure 2.6 begins by pulsing $ZnCl_2$ vapour in the gaseous phase into the chamber (Figure 2.6a); this gas then reacts with the substrate and is absorbed onto the surface. Any remaining $ZnCl_2$ is then purged from the chamber using an inert gas such as Ar (Figure 2.6b). The precursors do not react with themselves therefore terminating the growth of the thin film after a single layer; this is the self-limiting process of ALD. After waste is pumped out the anionic H_2S is pulsed in which reacts with the cationic $ZnCl_2$ and some of the molecules are absorbed into the first monolayer (Figure 2.6c). The desired ZnS compound given in equation 2.5 is formed, and the bi-product, HCl, of the reaction is devolved from the deposited surface as a vapour. The remaining H_2S and the HCl are then purged from the chamber with a second pulse of inert gas (Figure 2.6d). The process is then repeated until the desired thickness is reached.

Unlike the following two methods, deposition is not affected by pressure, but rather by the temperature of the substrate which must be high enough for chemisorption, but not so high to cause desorption of the monolayer (9). The temperature of the substrate also affects the grain size and the crystal structure of the phosphor layer; layers grown at 500°C have hexagonal (wurtzite) structure whilst ZnS grown at the lower temperature of 350°C has cubic (zinc blende) structure (39).

The main benefits of ALD over other deposition techniques are that it is a self-limiting process which therefore gives precise thicknesses; it is also pin hole free and has excellent uniformity across large areas (40), it can also deposit the insulator/phosphor/insulator layers in a continual process eliminating the exposure of moisture sensitive materials to the atmosphere. The main disadvantages of ALD are its slow deposition rate and costs, start-up is expensive and some materials cannot yet be deposited cost effectively.

2.5.2 Evaporation

Evaporation is the simplest PVD method and occurs when a material is heated to its equilibrium vapour pressure; this pressure is defined as the pressure of the vapour in equilibrium in its condensed phase at a certain temperature (30). When sufficient heat is applied to the material in order to dissociate atoms, providing the pressure is low enough (1 x 10^{-4} Pa), the individual atoms will travel collision free to the substrate in a straight trajectory and condense on the surface as depicted in Figure 2.7. The two most common types of evaporation are thermal and electron beam evaporation (EBE).

Thermal evaporation involves vaporising the material by heat energy; this is done by placing the material in a crucible or wire basket that is connected to two electrodes and passing an electric current through it (41). This type of evaporation is only suitable for materials that have a melting point of less than 1400°C, for materials with a melting point of less than 2200°C, electron beam evaporation can be used (9).

EBE uses a focused beam of energetic electrons (~10 keV) to heat the material, which is usually placed in a water cooled copper (Cu) pocket. The electrons, typically from a hot filament, are accelerated electrostatically and then directed towards the material either by a variable electromagnet or by a combination of fixed magnets and a variable electric field. The localised nature of EBE means the chances of contamination and reaction between the material and the holder are greatly reduced compared to thermal annealing.

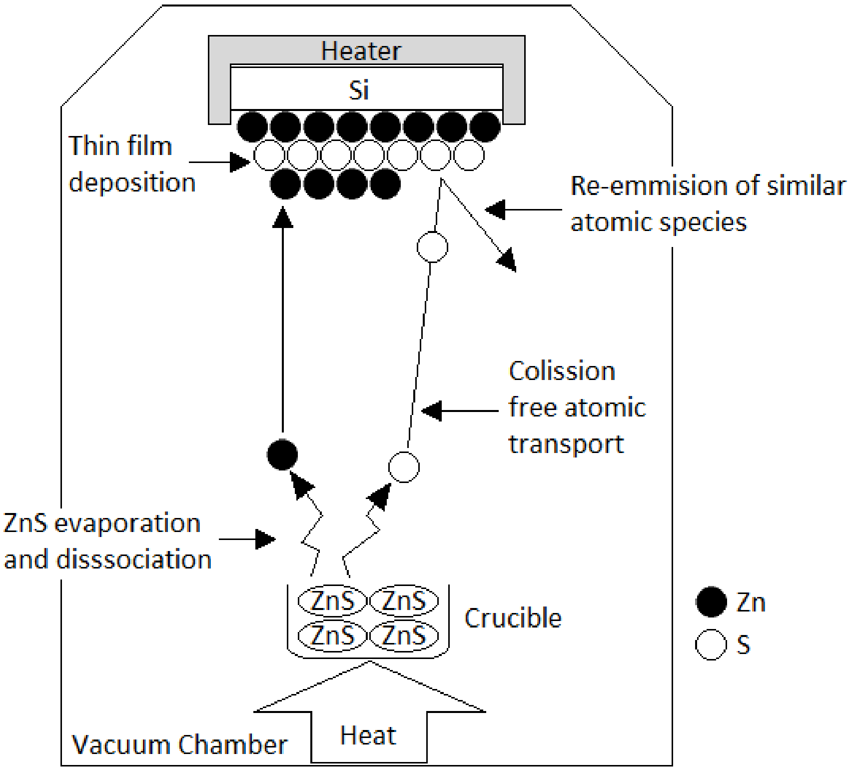

Figure 2.7 - Thermal evaporation of ZnS (9)

2.5.3 Sputtering

Sputtering is a very common deposition method used and involves bombarding the target material with energetic particles in order to dislodge atoms as depicted in Figure 2.8. The energetic particles are ions from the plasma that is generated by applying a large voltage across a low pressure argon gas; these ions are accelerated towards the negatively charged cathode. If the ions hit the target material with enough energy, one or more atoms can be dislodged, travel through the vacuum and deposit on the anodic substrate. Ions with energy of ~10eV and below will just bounce off the surface while those with energies of ~10 keV will become deeply imbedded in the surface of the target material (4).

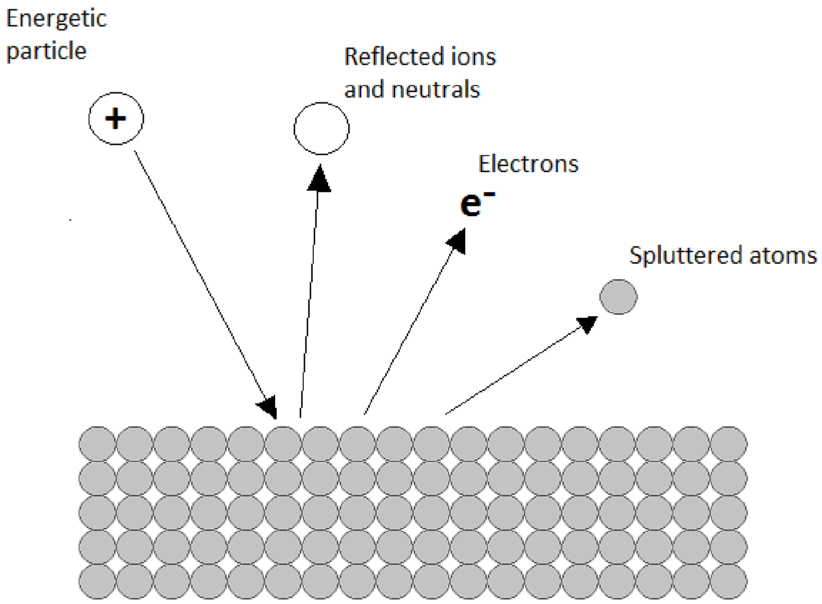

Figure 2.8 - Sputtering process

A benefit of sputtering systems is that they can fabricate entire ACTFEL stacks, insulators, phosphor and electrodes, without the need to remove the substrate from the chamber, therefore eliminating the risk of the surface coming into contact with the atmosphere and any potential defects settling on the surface such as dust particles.

2.6 Post deposition Annealing

The post deposition annealing of ACTFEL devices is a critical step in the fabrication process (42) as it enhances the luminescent properties of the phosphor layer by improving the crystallinity, removing strain and increasing the impurity diffusion into the host lattice.

2.6.1 Thermal Annealing

During the deposition of ACTFEL devices, the temperature of the substrate determines the crystalline quality of the thin film layers. If the temperature is too low, the atoms do not have the required energy to diffuse and few form crystallites. The critical temperature at which the resulting thin film quality is of an acceptable standard was found to be 190°C (43). At this temperature the energy of the atoms is higher and they are able to diffuse to the correct crystallographic sites, hence the quality of the layers is improved.

Post deposition annealing of the thin film further increases the crystalline quality. The more crystalline the thin film is the better the electron transport properties will be. This also activates the dopant in the phosphor layer by effectively incorporating the luminescent ions into the host lattice. Finally, it can remove any strain in the film that may cause reliability problems. The most common type of post deposition annealing used in thin film processing is thermal annealing (TA). This is typically carried out in a resistively heated chamber for one hour or longer usually at a temperature of around 500°C. It can be carried out under pressure or at atmosphere, in a gaseous environment with either an active or inert gas; the conditions of the chamber can be altered dependent upon the requirements of the sample being treated. TA however reduces the interface state density and limits performance and is not suitable for glass and plastic substrates prompting interest in more localised heat treatments.

One alternative to traditional TA is rapid thermal annealing (RTA). RTA is carried out in a chamber where the environment can be controlled in the same manner as for TA, pressure and gases. This is considered to be a clean process in that there is no risk of contamination, unlike with TA. RTA uses a tungsten-halogen quartz lamp to rapidly heat the sample using infrared radiation; the required temperature can be reached within a matter of seconds and the treatment itself lasts in the order of minutes making RTA a suitable heat treatment for glass substrates.

2.6.2 Laser Annealing

An alternative to thermal annealing is laser annealing. Although not widely used, an extensive research program has been carried out by NTU demonstrating the benefits of laser annealing of ZnS:Mn thin films (36, 43, 44). Laser annealing has been used since the late 1970s (45) and is now routinely used on Si for thin film transistor (TFT) display applications. Laser processing of Si converts amorphous silicon to polycrystalline silicon. Laser annealing of ZnS:Mn thin films was first reported in 1982 (46) in which RF magnetron sputtered ZnS, implanted with Mn to form films of ZnS:Mn (0.3 at%) were laser annealed using a xenon chloride (XeCl) laser (λ = 308nm = 4.025eV). The films were subjected to single pulse irradiations of 40ns up to a fluence of 3 J/cm^2 whilst in air and under a pressure of 100psi/6.9bar in neon (Ne). Although these initial laser annealing trials showed an improvement to the photoluminescent (PL) characteristics of the ZnS:Mn films it was unsuccessful at improving the EL (47).

Interest in laser annealing within the research group at NTU was renewed in 1997 using a krypton fluoride (KrF) laser (λ = 248nm = 4.98eV) and have since demonstrated a fourfold increase in EL emission when compared to devices that have been thermally annealed at 450°C, as shown in Figure 2.9.

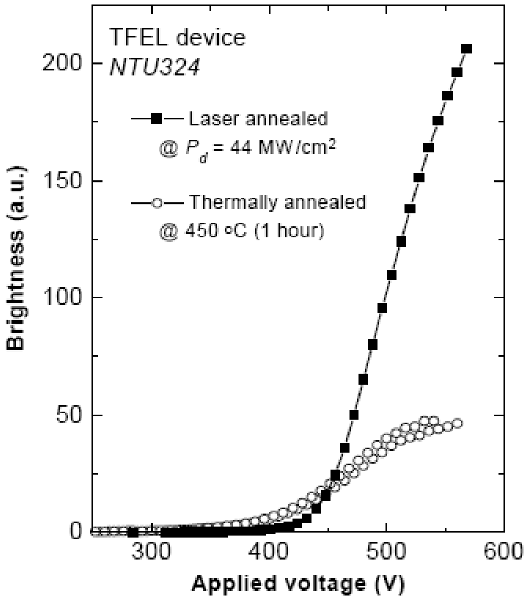

Figure 2.9 - Brightness Vs applied voltage for ACTFEL devices subjected to thermal annealing and laser annealing (26)

Excimer lasers are the preferred laser due to their high energy UV output and include the following lasers; XeCl, KrF, argon fluoride (ArF)(λ = 193nm = 6.4eV) and xenon fluoride (XeF)(λ = 351nm = 3.53eV) which have all been used for processing ZnS:Mn with varying results (44, 48-51). The wavelengths of KrF and ArF lasers are compatible with the absorption spectrum of ZnS:Mn. In order for the phosphor film to achieve efficient absorption of the laser pulse, it must be irradiated with photons of energy greater than that of the band gap of the phosphor material (3.66eV for ZnS), as, at lower energy, the films are optically transparent (52). The absorption coefficient (*α)* of ZnS at both wavelengths (193 & 248nm) is sufficient enough to prevent the laser irradiation from reaching the substrate and hence prevents any heat damage. X-ray diffraction has shown that a phase change occurs (53) within the top 200nm of the phosphor film, this is the approximate depth, depending on the fluence, that the laser penetrates into the phosphor (54), transforming from the deposited cubic to hexagonal.

Laser annealing has a very short processing time, the localised nature of the heat treatment make it an ideal process for temperature sensitive substrates such as glass and plastic.

2.7 Aging and Space Charge

The aging of ZnS:Mn ACTFEL devices is described as a softening and shifting of the luminance - Voltage (L-V) and/or Transferred Charge - Voltage (ΔQ-V) curves. The softening of the curve means that the rise in luminance as a function of the applied voltage becomes less steep and the shifting is a movement in either the positive or negative direction along the voltage axis (55) as can be seen in Figure 2.10. The lifetime of a device is the time it takes the device operated under constant conditions to reach 50% of its initial luminance.

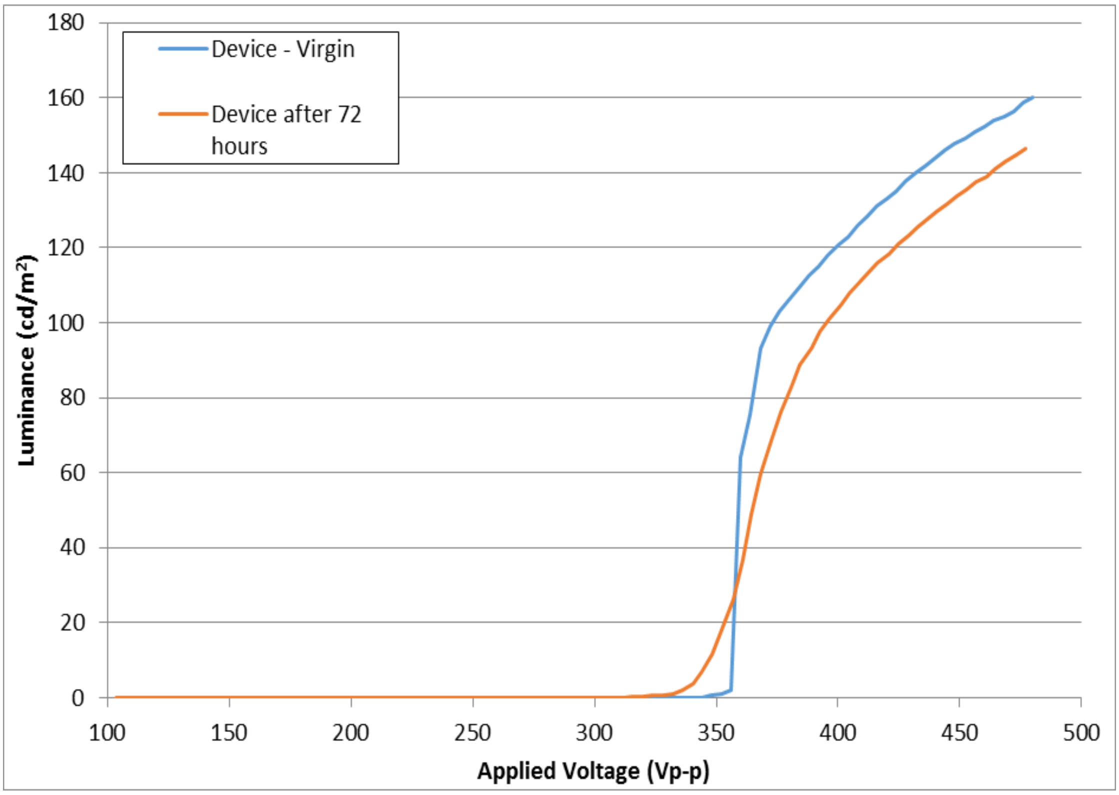

Figure 2.10 - Aging of ZnS:Mn ACTFEL device

The direction of the threshold shift along the voltage axis is mainly dependent upon the deposition method used, ALD devices show a negative shift (n shift) in which the threshold voltage decreases during aging, whereas sputtered devices have demonstrated a positive shift (p shift) in which the threshold voltage has increased during the aging process. The cause of the shift, in both directions has been attributed to the generation of positive space charge within the phosphor layer (56, 57). The space charge is assumed to be positive due to the wide band gap semiconductors used for ACTFEL devices being typically n-type. Space charge can be generated with the phosphor by one of the following two mechanisms, which are depicted in Figure 2.11;

[1] Band-to-band impact ionisation (58-60) in which an additional electron is promoted to the conduction band as a delocalised charge carrier. A hole is left in the valence band which may drift towards the cathode before becoming trapped, resulting in a positive localised charge which pulls the energy bands down.

[2] Trap-to-band which can occur either by impact ionisation (61, 62) or by [3] thermal or field emission of a trapped electron (63, 64), the removed electron is swept towards the anode whilst the ionised trap is now positively charged and locally pulls the energy bands down as above.

In an Ideal ACTFEL device the electric field is constant; this field is depicted as the slope of the valence and conduction bands in an energy band diagram, the presence of space charge within the phosphor layer of a device causes a non-uniform electric field which is illustrated by the bends shown if Figure 2.11. The band bending causes the electric field at the cathode to be greater than it would be under the same externally applied field compared to an ideal device; this in turn enhances the tunnel emission of electrons from the insulator/phosphor interface states and allows tunnel emission to occur at lower voltages resulting in a decreased threshold voltage. The electric field at the anode is reduced as a consequence of the space charge subsequently there are less energetic electrons in this area reducing the probability of impact excitation.

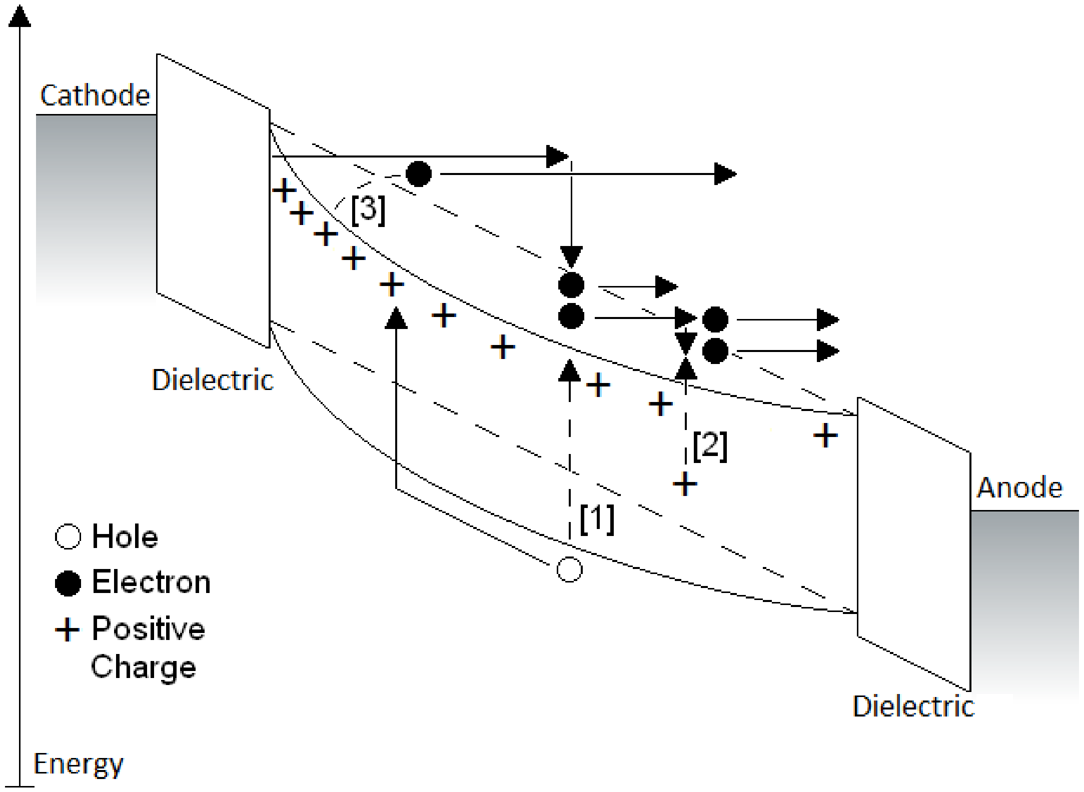

Figure 2.11 - Energy band diagram of an ACTFEL device depicting space charge generation and its effects on the bands.

2.8 Conclusion

The aging of ACTFEL devices remains one of the major problems to be solved in order to improve the quality of the displays (55, 65). Previous studies have shown that the stability of the devices depends upon the structure and materials (66-68) the deposition method (69) and the driving method used (70, 71). This study focuses upon the effects of the driving method with particular impetus being placed on the timing of taking a device from its virgin state to the operating point.

3. Experimental Methods

3.1 Introduction

This chapter describes the experimental equipment, the techniques and the theory used throughout this research project. This includes the electrical characterisation of individual thin film layers and complete devices, as well as post deposition annealing methods.

3.2 Experimental Set-up

Although a number of specialised configurations and equipment are available for ACTFEL device characterisation, it is the Sawyer-Tower method (22) that is preferred and is used throughout this project due to its simplicity. This set-up is shown in Figure 3.1. A computer controls a Tektronix AFG 5101 programmable function generator (PFG). The voltage signal from the PFG is amplified by a Trek PZD350A high voltage linear amplifier**,** this signal then passes through a resistor (R) before being applied to the device under test (DUT), which is placed on a purpose built probe station. It then passes through the sense box to ground. A Minolta 110 luminance meter with close up lens 122 is positioned above the DUT. The luminance along with the voltage across the ACTFEL device (V_2) and the voltage across the sense component (V_3) are monitored by a Tektronix TDS 3014B digital oscilloscope.

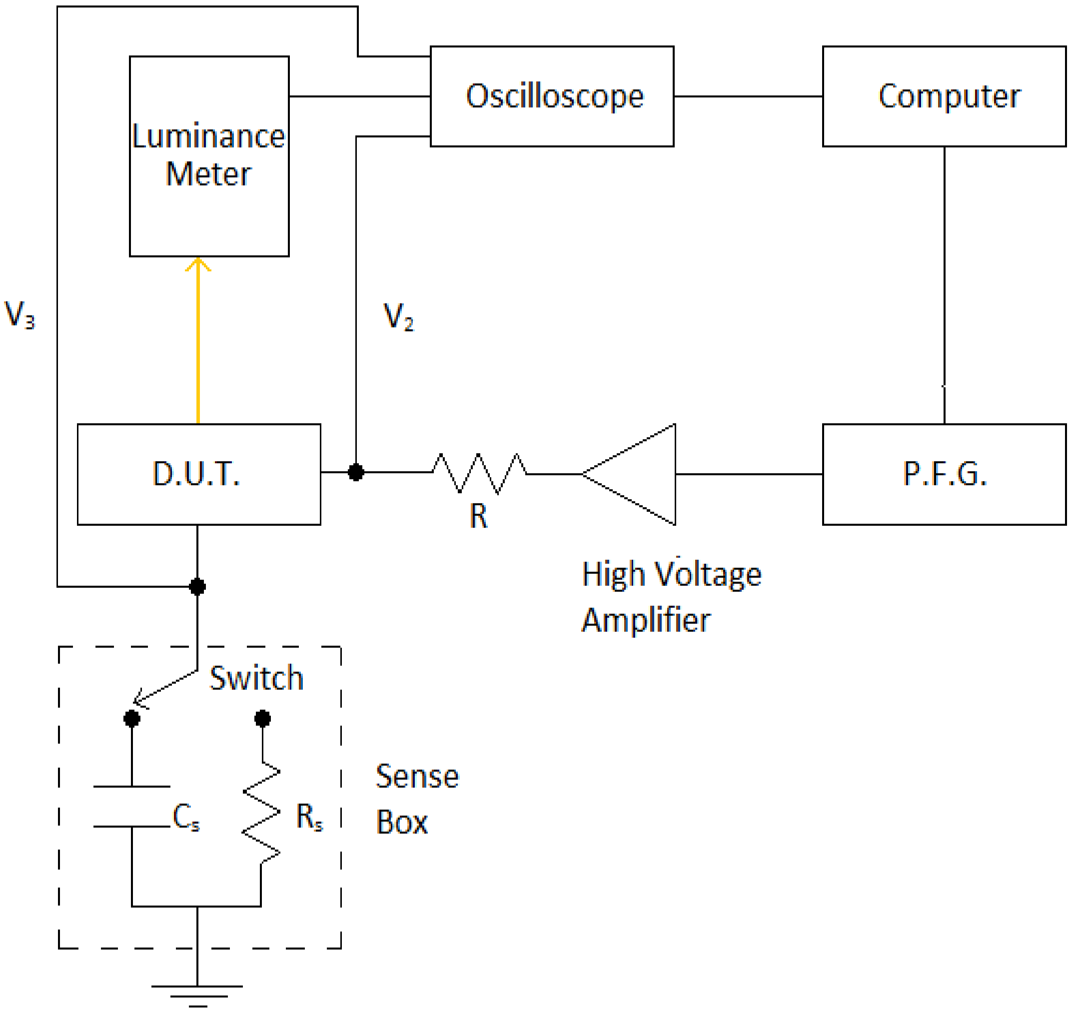

Figure 3.1 - Schematic diagram of equipment used for ACTFEL electrical and optical characterisation

The probe station is capable of being moved very accurately (0.01mm) in both the X and Y planes in order to probe the aluminium (Al) bond pads or ITO dots. In the case of the Al bond pads, which are difficult to distinguish with the naked eye, a microscope is used in order to ensure that proper contact is made with the pad for the required pixel. The microscope is moved out of position so that the luminance meter can be situated above the device, in order for the luminance meter to accurately measure the light emission from the ACTFEL device. The internal sensor must be positioned 323mm vertically from the surface of the device. The area measured by the close up lens on the luminance meter is a 1.1mm diameter circle, which fits inside the ITO dots, but is larger than the pixels measured on the fixed legend LETFEL devices. The internal lens system of the luminance meter has an acceptance cone angle of $1/3^{o}$; any emitted light outside of this angle is not detected.

The resistor R is included in the system in order to protect the ACTFEL DUT from catastrophic failure as it acts as a current limiter, and also to protect the equipment from a short condition should a catastrophic failure occur. The value of this resistor is 1.5kΩ, this is the maximum value that the resistor can be before it affects electrical characterisation. With the device acting as a capacitor, the inclusion of a resistor in the circuit creates an RC time delay and obscures observation of the dynamic response of the device. The V_3 voltage across the sense capacitor (C_S) is measured as a function of time and forms the basis of all the electrical characterisation measurements. The value of C_S needs to be significantly larger, up to a 100 times greater, than that of the device, so that the applied voltage drops across the device. The value of C_S is typically 100nF, this value of C_S is used in this study. The sense resister (R_S) is used in place of a sense capacitor to in order to measure the current through the ACTFEL by monitoring the voltage V_3. R_S usually has a very small value, for this study it is 10Ω.

The whole system is automated and controlled by a computer program which was created by the author in collaboration with Dr. Costas Tsakonas using National Instruments LabVIEW Version 7.0. The program communicates with the PFG and the oscilloscope via a General Purpose Interface Bus (GPIB). The program is capable of recording the voltage and luminance then displaying the luminance – voltage (L-V) curve graphically. It also records the V_2 and V_3 voltages as a function of time over 10,000 points. This is only recorded for each step on the L-V curve above the designated threshold voltage (V_{th}), which was 1cd/m^2. The following parameters can be controlled by the program with the typical values and options shown in parenthesis;

- Waveform (trapezoidal, sinusoidal, square, triangle).
- Frequency (100Hz to 5kHz) although due to the trapezoidal waveform being user programmed it was only available at 1kHz.
- Applied voltage (100Vp-p to 800Vp-p).
- Applied voltage step size (4, 5, 10 & 20Vp-p).
- Step duration (3, 5, 10 & 20s).
- Number of B-Vs to be carried out (12).
- Aging duration between B-Vs (6H).
- The duration between V_2 and V_3 recordings during aging (1H).

The waveform employed during this device characterisation study is a pulsed bipolar trapezoidal waveform. Sinusoidal waveforms are a popular choice due to their smooth transition reducing the amount of stress placed on the device and their ability to be produced easily by inexpensive equipment. This waveform is acceptable if luminance is the only interest but for more detailed characterisation bipolar trapezoidal pulses are preferred as the shape allows greater level of detail to be gained on the devices internal and external operation. The waveform at 1kHz, shown in Figure 3.2, has a rise and fall time of 5µs and a pulse width of 30µs. The labels A-J denote important points in the applied waveform and will be used to match points in the plotted data, points B and G indicate when charge begins to flow in the phosphor layer, this is also referred to as the threshold voltage.

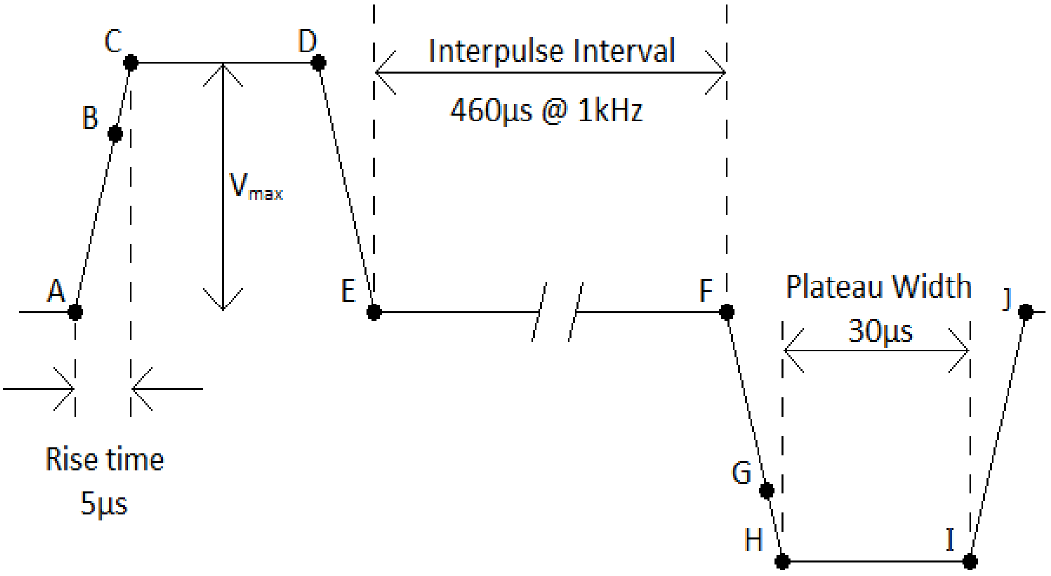

Figure 3.2 - Bipolar trapezoidal pulsed waveform.

3.3 Electrical Characterisation

Measuring the luminous output of an ACTFEL device is a useful indication of the potential, but no profound information can be gained in regards to the physics of the device. For this reason the electrical behaviour is studied in order to develop a greater understanding of the device physics. This section details the common electrical characterisation methods used for ACTFEL devices.

3.3.1 Charge – Voltage Characterisation (Q-V)

The charge – voltage (Q-V) (72-74) is the most common and straight forward of the electrical characterisation methods used for ACTFEL devices and the data obtained forms the basis of the other methods. The Q-V curve is acquired by plotting the charge on the sense capacitor $q_{ext}(t)$ against the voltage measured across the device $V_a(t)$. The external charge and applied voltage are given by;

$$q_{ext}\;t\;\;=C_sV_3\;t \tag{3.1}$$

and

$$V_a\;t\;\;=V_2\;t\;\;-\;V_3\;t \tag{3.2}$$

where C_s, V_2 and V_3 are shown in Figure 3.1. The charge plotted in a Q-V curve is the external charge that is measured as a voltage across the sense capacitor which is why the Q-V is sometimes referred to as the Q_e-V_e. The voltage, V_a, plotted is not the applied voltage but the voltage drop across the ACTFEL device; this is because some of the applied voltage drops across the series resister and the sense capacitor.

Figure 3.3 shows a family of Q-V curves of a RF magnetron sputtered device, typically curves for several voltages above threshold are measured, below threshold the Q-V is a straight line due to the completely capacitive nature of the device up until that point. As the voltage is increased above the threshold the plot starts to open up and form a hysteric loop, curves at voltage 20, 40, 60 and 80V above threshold are shown.

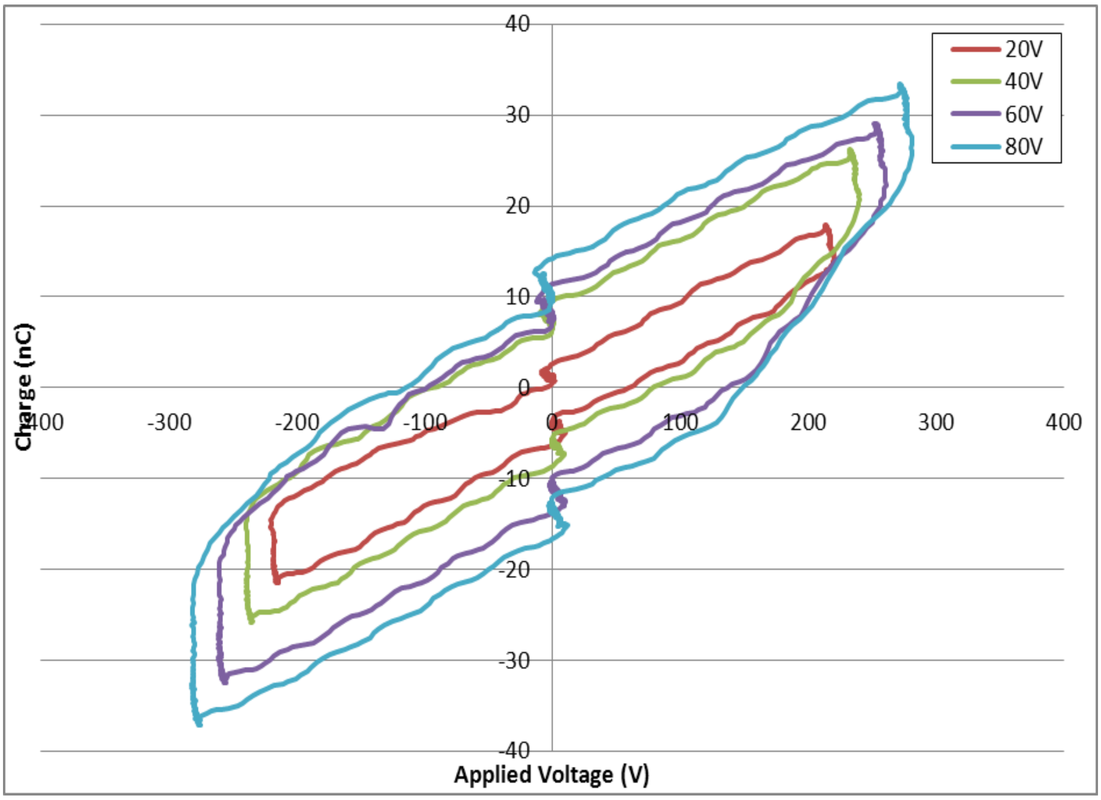

Figure 3.3 - A family of Q-V curves for a RF magnetron sputtered ZnS:Mn device driven at 1kHz.

The Q-V curves presented above are offset from the origin, this is a common occurrence for certain types of ACTFEL devices, for the purposes of electrical characterisation these can be offset adjusted (75) to allow for comparison.

The Q-V curves are evaluated once a steady state has been established with the ACTFEL device and the driving waveform; this typically takes 3 – 4 periods of the applied waveform.

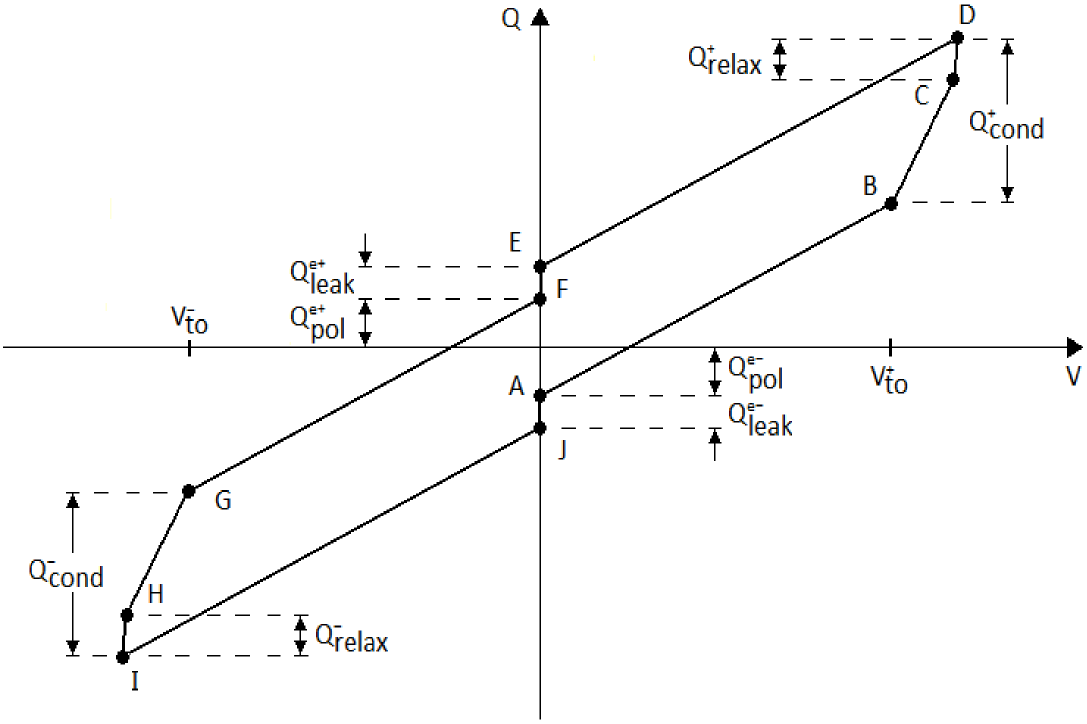

Figure 3.4 - An Idealised Q-V curve detailing the important information which may be obtained.

A somewhat idealised Q-V curve is shown in Figure 3.4 presenting the main features that are observed during ACTFEL device operation. The Q-V curves progresses in a counter clockwise direction, the A-J labelling correspond to those on the driving waveform in Figure 3.2. The following behaviour described at points A-J has been summarised from the work of J. F. Wager and P. D. Keir (76). Point A corresponds to the onset of a positive voltage pulse on the top electrode, this is a non-zero value due to the polarisation charge, Q_{pol}, active in the phosphor-insulator interface as a result of the previous negative polarity pulse. As the voltage increases towards V_{max} between points A and B, the voltage is divided between all the layers of the stack, as the electric field at the bottom phosphor-insulator interface is not sufficient for charge injection into the phosphor layer. As no charge moves within the device, the slope of the Q-V plot between points A and B is the capacitance of the total stack, i.e the series combination of the phosphor and both insulating layers.

At point B the required electric field for charge to begin to be injected into the phosphor layer is reached. This point is denoted as the turn on voltage, V_{to}. The value of V_{to} is determined by the threshold voltage minus any terms that arise due to space charge and polarisation charge that may be present within the device. As these two charges increase with the maximum applied voltage, the value of V_{to} will decrease in response to the increase in V_{max} while the threshold voltage remains constant and independent of V_{max}. As the phosphor layer is now conducting it is effectively shorted out, so the slope of the Q-V plot between points B and C is equal to the capacitance of the series combination of the two insulating layers.

At point C, the maximum voltage is reached and injection into the phosphor layer ceases. The driving waveform remains constant at the maximum amplitude up to point D. Between points C and D a small amount of charge transverses the phosphor layer, this charge is known as relaxation charge, Q_{relax}. As the phosphor electric field decreases, this charge occurs without an increase in the external field.

From Point D to E is the trailing edge of the voltage pulse and the applied voltage decreases from its maximum to zero. During this time the phosphor field is reduced and no charge moves within the device, so the slope once again is equal to the total capacitance of the device. Finally from point E to F shows the period between the end of the positive pulse and the onset of the negative pulse. No voltage is applied to the device during this section. During this sector of the waveform leakage charge, Q_{leak}, is transferred across the phosphor layer, the precise physical process for this event is not known but it is thought that it arises from electrons returning from the cathode to the anodic phosphor-insulator interface. The process is repeated for the remaining points, F to J, relating to the negative half of the cycle.

Figure 3.4 details important charges that can be ascertained from a Q-V curve, the charge across the capacitor at particular sections of the plot has physical meaning. Q_{pol} is the polarisation charge which is the stored charge remaining in the phosphor-insulator interface just prior to the onset of the opposite polarity pulse Q_{cond} is the conduction charge transported across the phosphor layer during the voltage pulse, it is this charge that is responsible for impact excitation of the luminescent impurities which are the source of light emission. Q_{relax} is the relaxation charge that flows across the phosphor layer when the applied waveform is constant at its maximum voltage, the phosphor field decreases during this time, hence the term relaxation charge. Q_{leak} is the leakage charge that arises during the zero applied voltage sections of the waveform; it occurs due to the emission of electrons from shallow interface states. The scale of this charge is dependent upon the depth of the interface states and the magnitude of the polarisation field.

3.3.2 Capacitance – Voltage Characterisation (C-V)

Capacitance – voltage curves (77-79) are produced by plotting the dynamic capacitance as a function of the dynamic voltage drop across the ACTFEL device, it is the rising edge portion of the waveform that plotted for both the positive and negative pulses. The dynamic capacitance is the slope of the Q-V curve and can be obtained by two different methods, the experimental system used allows for both methods to be used. The first method involves measuring the current using the sense resistor R_s;

$$C\ \ t\ \ = \frac{i(t)}{\frac{\delta V_a(t)}{\delta t}} \tag{3.3}$$

where

$$i\ \ t\ \ = \frac{V_3(t)}{R_s} \tag{3.4}$$

The second method and the one used during this study simply involves calculating the derivative of the Q-V curve as the dynamic capacitance, given by;

$$C\ \ t\ \ = C_s \frac{\delta V_3}{\delta V_a} \cong \frac{\delta q_{ext}\ \ t}{\delta V_a\ \ t} \tag{3.5}$$

The C-V curve is then generated by plotting C against V_a(t). Figure 3.5 shows an idealised C-V curve. Initially at the lower voltages the capacitance is equal to the capacitance of the entire ACTFEL device, C_{tot}, (series combination of the capacitances of the phosphor layer and the two insulating layers). As the voltage reaches the turn-on voltage, the capacitance rises to equal the series combination of the capacitances of both the insulating layers, C_{ins}.

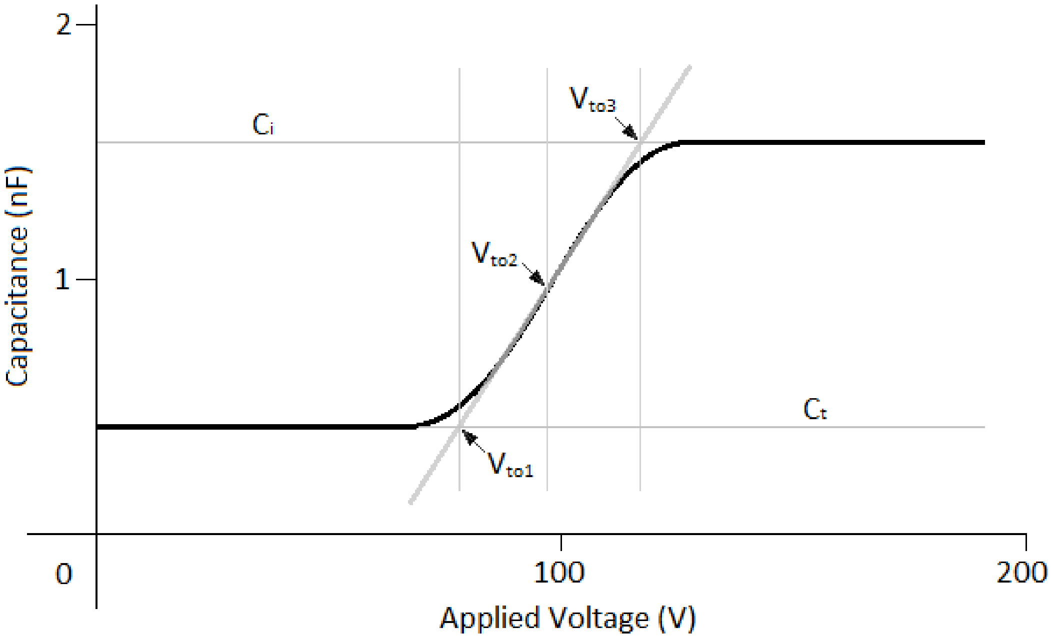

Figure 3.5 – Idealised C-V curve.

Once the C-V curve has transitioned to C_{ins} it does not always remain flat at this value, experimental curves often display overshoot, this is due to positive dynamic space charge within the phosphor layer. In practice there are very few C-V curves where the physical capacitance, that is the calculated capacitance from the thickness and the dielectric constant, equal those of the C-V curve. In the case of the total capacitance, the physical and experimental values are usually in good agreement and any disparities are usually down to an inaccuracy in the thickness of one or more of the layers. If the experimental insulator capacitance is less than the physical capacitance then the conduction current from the rising edge of the applied voltage waveform is insufficient to completely shunt the phosphor capacitance. This is attributed to inadequate density of interface states (76). The interface state density can be calculated from the slope of the C-V curve using the equation:

$$Q_{ss} = \frac{C_i^2}{2qA} \frac{C_t}{C_p} \frac{\Delta C}{\Delta V}^{-1} \tag{3.6}$$

where A is the area of the device and the term in brackets is the slope of the C-V transition.

3.4 Optical Characterisation

3.4.1 Luminance – Voltage Characterisation (L-V)

One of the most important figures of merit for an ACTFEL device is its luminance; this is typically quantified using luminance Vs voltage (L-V) curves sometimes referred to as brightness Vs voltage (B-V) curves. An L-V curve is accomplished by applying a voltage to the ACTFEL device well below the threshold voltage, the applied voltage is then increased to a predetermined maximum voltage. The luminance is measured at each point by a Minolta 110 luminance meter and is recorded, along with the peak to peak (Vp-p) voltage. The system is fully automated and controlled via a LabView program as described in section 3.2. The L-V curve is achieved by plotting the luminance as a function of the applied voltage, Figure 3.6 shows a typical L-V curve for a sputtered ZnS:Mn ACTFEL device driven by a 1kHz trapezoidal waveform.

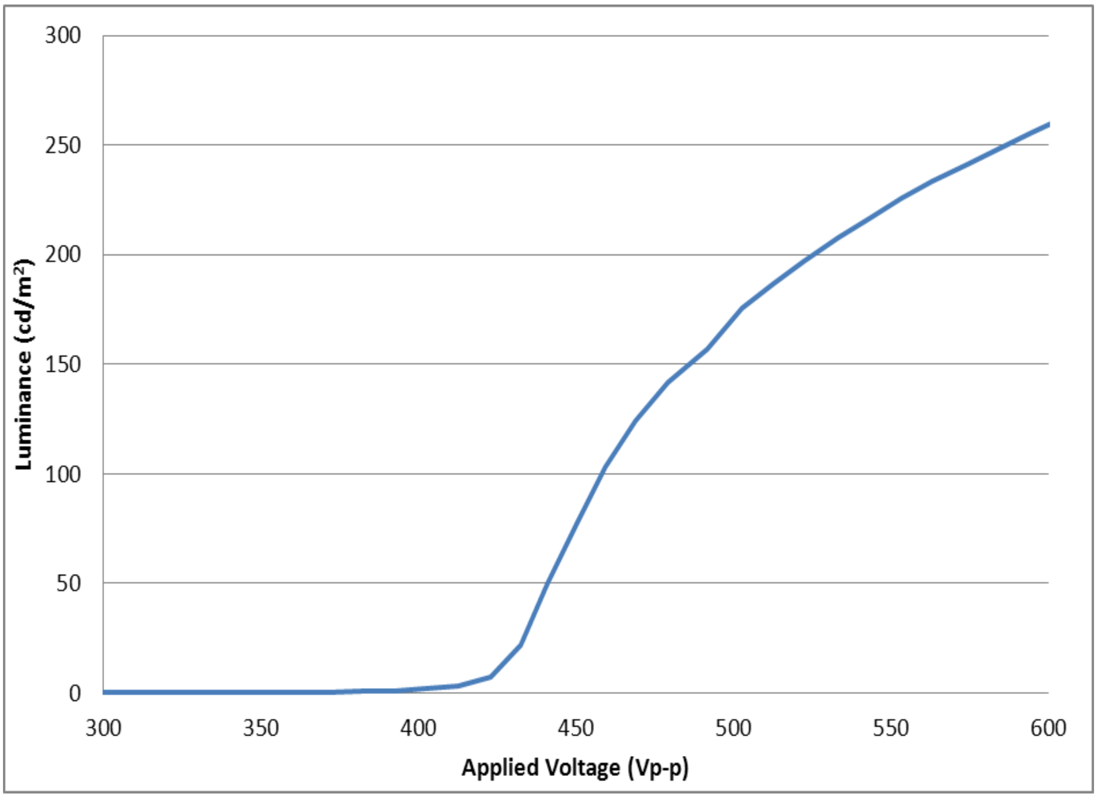

Figure 3.6 - L-V curve for a sputtered ZnS:Mn ACTFEL device driven by a 1kHz trapezoidal waveform.

The luminance of an ACTFEL device is dependent upon several key factors associated with the driving waveform; the type of waveform, its shape and the frequency at which it is being driven. The time that the waveform spends above the threshold voltage determines the luminance therefore a 5 kHz square wave will have a higher luminance than a 1 kHz sinusoidal waveform. The temperature also has an effect on the device luminance as at high temperatures the probability is increased that excited electrons will relax non radiatively. Space charge generation is also dependent on temperature and could cause a shift in the threshold voltage.

The type of waveform and the frequency must be reported with any L-V curve, for this study a 1 kHz trapezoidal waveform has been used unless otherwise stated.

3.4.2 Transient Analysis

A less common optical characterisation method is the transient luminance measurement (l(t)), which can often reveal more about the physical operation of an ACTFEL device than an L-V curve. The luminescent output of the device is measured using a fibre optic connected to a photomultiplier tube (PMT). The light emission is observed as a function of time and can therefore be compared to key features of the applied voltage waveform yielding information on device operation. The experimental set-up shown in Figure 3.1 was used with the addition of the PMT replacing the luminance meter, and with the fibre optic positioned above the device under test. The resistor R was removed from the system.

l(t) measurements for a sputtered ZnS:Mn device for both voltage polarities can be seen in Figure 3.7, the peaks of the curves can be matched to the corresponding portion of the applied voltage waveform. As the voltage pulse reaches the turn-on voltage, a sharp rise in luminance is observed as the excited luminescent centres decay back to their ground state. This initial peak is termed the leading edge (LE) emission as it is caused by the leading edge of the voltage waveform. Once the applied voltage waveform has reached its maximum value the luminance ceases to increase and begins to decay exponentially with the lifetime of the associated excited luminescent centre.

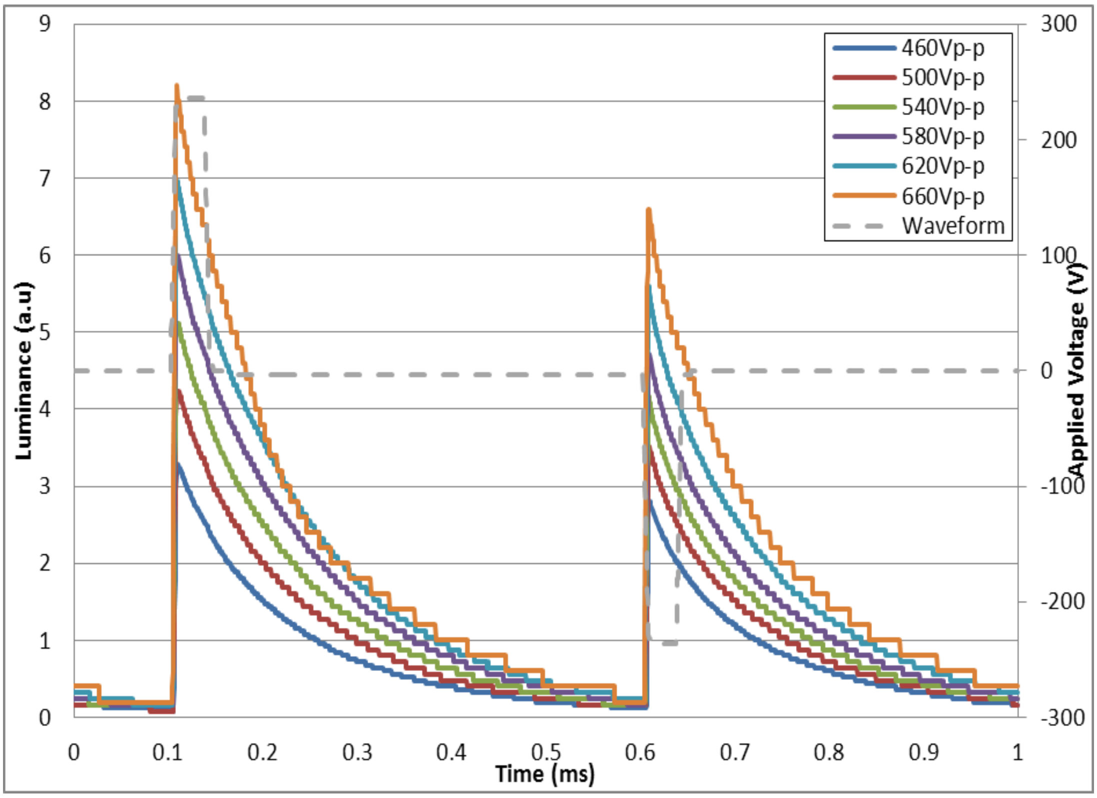

Figure 3.7 - Transient luminance curves for a sputtered ZnS:Mn device driven at 100Hz

A second luminance peak can sometimes be observed as the applied voltage waveform is decreased down to zero, this peak is termed the trailing edge (TE) emission. Although common for phosphors such as SrS:Ce (80) TE emission is very rarely seen in ZnS:Mn and when it does occur the peak is always smaller than the LE emission.

Due to the long decay time of Mn^{2+}, transient measurements were taken using a bipolar trapezoidal waveform at 100Hz as seen in Figure 3.7.

3.5 Laser Annealing

Laser annealing was carried out using a Lambda Physik LPX 305i excimer laser charged with Krypton Fluoride (KrF) to give a wavelength of 248nm and Argon Fluoride (ArF) to give a wavelength of 193nm, the laser emits pulses of 20ns duration for both wavelengths. The laser annealing experimental set up is shown in Figure 3.8. The laser beam first passes through a variable number of Hoya plates that are used to attenuate the intensity of the beam, (each plate can reduce it by ~ 8%), next the beam travels through the an Excitech homogeniser EX-HS-700D which is used to convert the non-uniform rectangular beam into the top hat profile required for a uniform density profile. The sample is held in a pressure cell with a UV grade window on an X – Y translation stage controlled via a PC to enable accurate positioning. The pressure cell is used to minimise ablation which can result in material loss (81), the pressure cell is filled with argon gas to achieve a pressure of 150psi (~10bar)

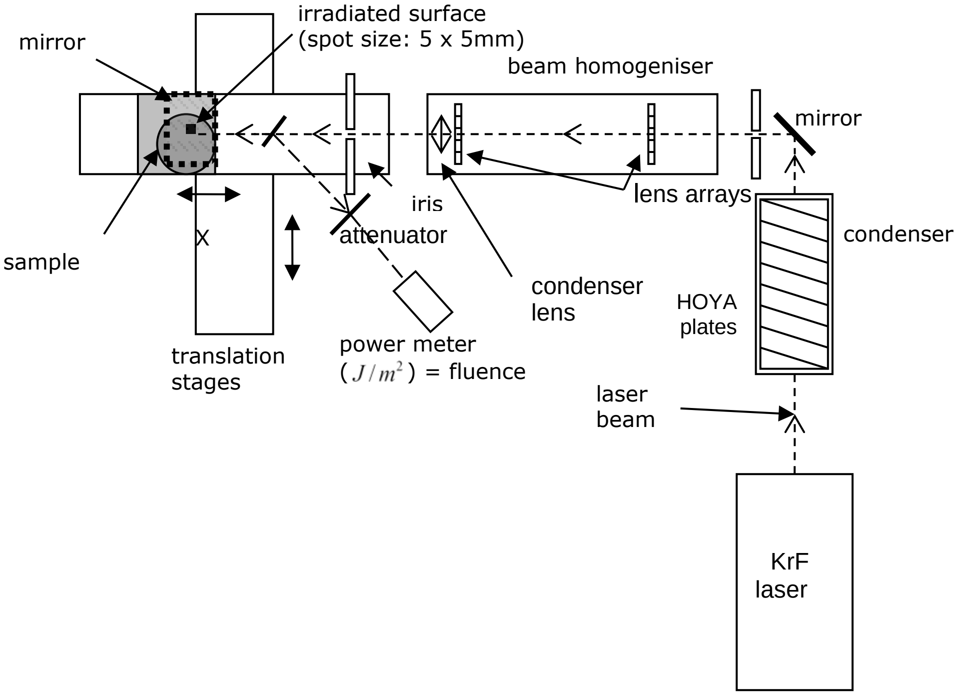

Figure 3.8 - Experimental set up of laser annealing equipment

3.6 Thin Film Deposition

The fabrication of ACTFEL devices requires the sequential deposition of the individual layers onto a substrate. For the samples grown at NTU, radio frequency (RF) magnetron sputtering was used to grow the insulating and phosphor layers as well as the transparent electrodes. Thermal evaporation was used for devices requiring aluminium (Al) electrodes.

3.6.1 RF Magnetron Sputtering

Radio Frequency magnetron sputtering was used to deposit the ZnS:Mn phosphor, the Y_2O_3 and SiO_2 insulating materials and the indium tin oxide (ITO) top electrodes. In order to ensure the films are clean and free from outside particulate contaminats, the Si substrate is loaded into the chamber via a class 100 clean room. The chamber, shown in Figure 3.9, is vacuum pumped down to a pressure below 10^{-6} mbar (1×10^{-4} Pa) by an oil diffusion pump backed up by a rotary pump. Prior to deposition the substrate is prebaked for one hour at 550°C to remove any moisture that may be present on the surface. An inert gas (argon Ar) is supplied into the chamber. The initial plasma needed for deposition is created by supplying the required RF power electric field with a frequency of 13.56 MHz to the magnetron material target, set to 40 W and increasing the relative chamber pressure to 25mTorr. The pressure is then gradually reduced to 3 mTorr (0.4Pa) for deposition to begin.

By reducing the pressure and increasing the power the Ar turns into a plasma made of positive $Ar+$ ions and electrons, the target attracts the positive ions as it is situated on top of the RF electrode that accumulates negative charge and becomes the cathode (82). The attracted ions then sputter off surface atoms which are deposited onto the anodic substrate situated approximately 15cm away. The substrate is rotated (~10rpm) during deposition in order to improve the uniformity; the layers are deposited at a temperature of 190^{o}C.

The multipurpose chamber was also used for thermal annealing under vacuum (2.0×10^{-7} mbar).

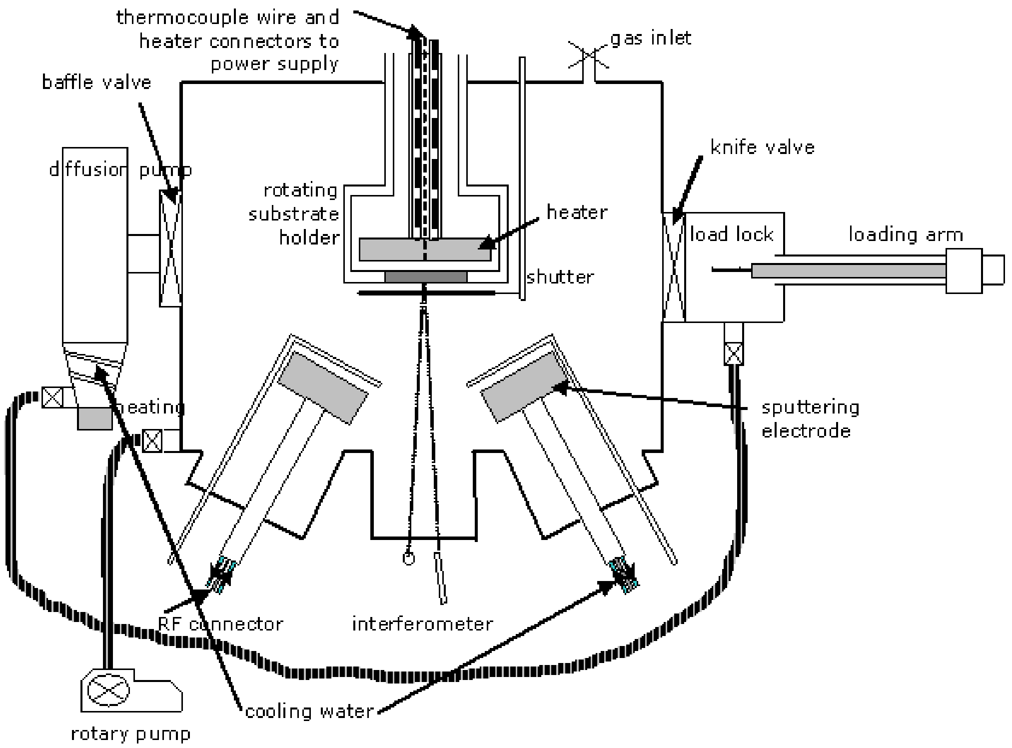

Figure 3.9 - Cross section schematic of RF Magnetron sputtering system.

3.6.2 Thermal Evaporation

During this project, samples required front (dots) and back Al electrodes to be deposited on to them. A vacuum evaporator, shown in Figure 3.10, was used for these depositions. The evaporation of the Al wire is a result of energy being delivered to a solid in order to raise its temperature to the point where atoms obtain enough energy to leave the surface of the solid (83).

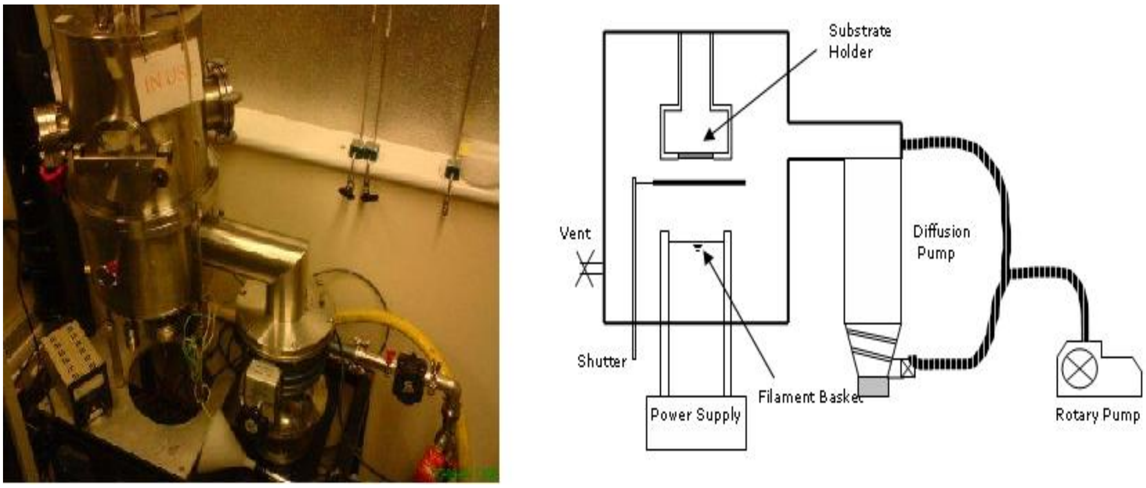

Figure 3.10 - Left – Photograph of evaporation system. Right – Schematic of evaporation system

The Al is placed in the filament basket which is heated by passing a high current through it. Once the evaporator has been pumped down to the required pressure, by first the rotary pump to 2 x 10^{-1} mbar and then the diffusion pump to below 1.5 x 10^{-5} mbar, the filament current is slowly increased until the Al starts to evaporate. The onset of this evaporation is observed by a sudden increase in current. The evaporated Al then condenses on to the surface of the wafer in order to form the electrode. In order to create the dots for the front electrode, a stainless steel contact mask with a series of 1mm holes, shown in Figure 3.11, is put in front of the wafer in the evaporator.

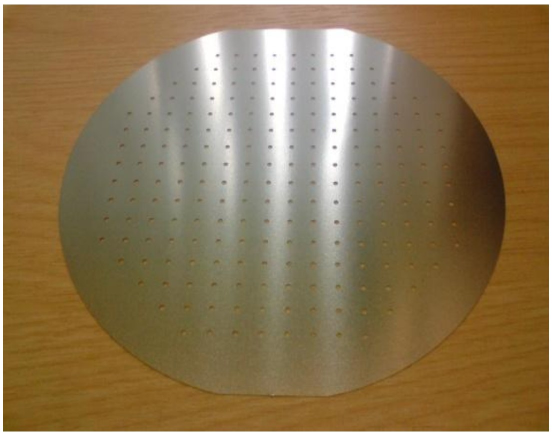

Figure 3.11 - Stainless steel contact mask used for depositing 1mm aluminium top electrodes on thin films.

3.7 Transmission Electron Microscopy

Transmission Electron Microscopy (TEM) was used to examine a cross sectional area of the as deposited and laser annealed HiTUS plastic devices, the analysis was carried on a Joel 2100F at Nottingham University. The samples are required to be so thin that they are transparent to the electron beam. The thickness is dependent upon the material, the higher the atomic number of elements the greater the electron scattering factor is therefore the thinner the sample needs to be (84), samples usually range from tens of µm to hundreds of nm. Samples are often coated with carbon or other highly conductive materials in order to enable or improve the imaging, further information on the general techniques of TEM can be found in Transmission Electron Microscopy: A Textbook for Materials Science (85).

The prepared sample sits on a small copper grid ~3mm in diameter; electrons are accelerated from a field emission electron gun at high voltages, 100-200kV, which are then imaged on the sample by a condensing lens. The sample is the magnified several hundred times which forms an intermediary image which is further magnified by a projection lens on to a fluorescent screen where it can be viewed (86). TEM images can be magnified tens of thousands of times; this is possible due to the wavelength associated with an electron being much smaller than that associated with light. The wavelength associated with a 200kV electron is approximately 0.0028nm (87).

3.8 Conclusion

This chapter has presented the experimental methods used during the research project and also the theory behind them. The equipment used to obtain the characterisation data has been described as well as the setup used for the KrF and ArF laser annealing of thin film ZnS:Mn. Finally there is an overview of the equipment used in order to fabricate the different layers of the thin film devices.

4. Characterisation of ZnS:Mn ACTFEL Devices Laser Annealed at 193nm

4.1 Introduction

It is well known that a critical step in the TFEL fabrication process is the annealing of the phosphor layer. This is required to activate the dopant by effectively incorporating the luminescent ions into the host lattice (88-90) as discussed in Chapter 2. It also serves to improve the crystallinity of the phosphor layer. The annealing process is typically carried out as a post deposition thermal treatment in vacuum for 1 hour at 500°C (91), as this was found to be the optimum temperature for EL performance (26). Thermal Annealing has been shown to modify the electron transport properties within the device limiting performance by reducing excitation efficiency (92). Thermal annealing also has other limitations due to the substrates used; an alternative to thermal annealing is laser annealing.

The Laser annealing of ZnS:Mn films was first reported in 1983 (48). Since then, the NTU displays research group has demonstrated the benefits of post deposition laser processing in regards to the EL characteristics. It is thought that laser annealing at 248nm promotes a phase transition in the ZnS which goes from cubic to what appears to be a mixed phase of hexagonal and cubic, this suggests a re-ordering and possible removal of defects (36). The main advantage of laser annealing over thermal annealing is the localisation of the heat treatment. This chapter details the effects of laser annealing on the optical characteristics of devices, a direct comparison of the novel 193nm wavelength is made with 248nm.

4.2 Experimental Details

4.2.1 RF Magnetron Sputtering Thin Film Deposition

All the depositions for the RF magnetron sputtered devices were carried out at the NTU displays research facility by Dr. Demos Koutsogeorgis using a custom built Kurt Lesker Torus four electrode magnetron system as described in section 3.6.1. The thin film layers of Y_2O_3 and ZnS:Mn (0.45wt.%) were deposited from solid targets onto a rotating 4 inch diameter (100) n type Si wafer that had been pre-baked for one hour at 550°C to remove any moisture from the surface. The temperature of the substrate was maintained at 190°C in 0.4 Pa of Ar during the deposition of both the dielectric and phosphor layers, the depositions were carried out under a base pressure of 1×10^{-4} Pa. The thickness of the layers were 300nm and 800nm for both dielectrics and the phosphor layer respectively, these thicknesses were determined by using an interferometer during the deposition process. One half of each wafer was thermally annealed under vacuum for 1 hour 20 minutes at 550°C in the sputtering chamber, this temperature is used as it has shown to produce the best device performance when followed by laser annealing (93).

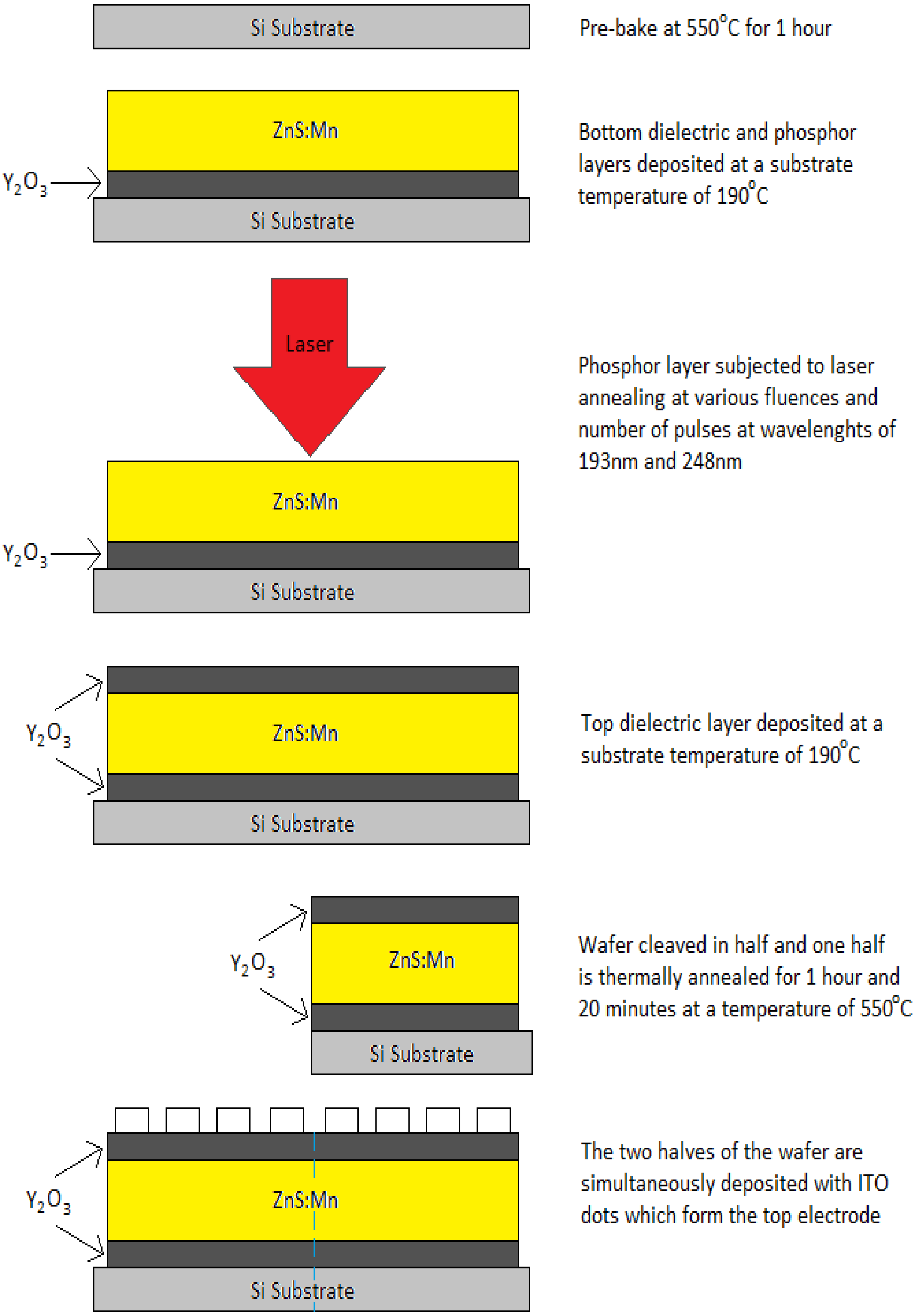

Pre-bake at 550°C for 1 hour

Bottom dielectric and phosphor layers deposited at a substrate temperature of 190°C

Phosphor layer subjected to laser annealing at various fluences and number of pulses at wavelenghts of 193nm and 248nm

Top dielectric layer deposited at a substrate temperature of 190°C

Wafer cleaved in half and one half is thermally annealed for 1 hour and 20 minutes at a temperature of 550°C

The two halves of the wafer are simultaneously deposited with ITO dots which form the top electrode

Figure 12 - Fabrication process

4.2.2 Laser Annealing

Laser annealing at 248nm has previously demonstrated an improvement to the luminescent characteristics of ACTFEL devices, and more so when followed by thermal annealing (93). The effect of laser annealing and the combination of laser followed by thermal annealing on electro-optical characteristics of ACTFEL devices is examined using various configurations of irradiated 5 by 5mm squares. The combination of the fluence used, the number of pulses and the wavelength are presented in Figure 4.13, this wafer also contains devices that have been laser annealed at a previously unreported wavelength of 193nm allowing for a direct comparison of 248nm and 193nm to be made.

The laser used during this study was a Lambda Physik LPX 305i excimer laser charged with Argon Fluoride (ArF) for 193nm and Krypton Fluoride (KrF) for 248nm. The laser emits 20ns pulses at a frequency of 1kHz when more than one pulse is applied. The laser annealing of the NTU grown devices was carried out in collaboration with Dr. Demos Koutsogeorgis.

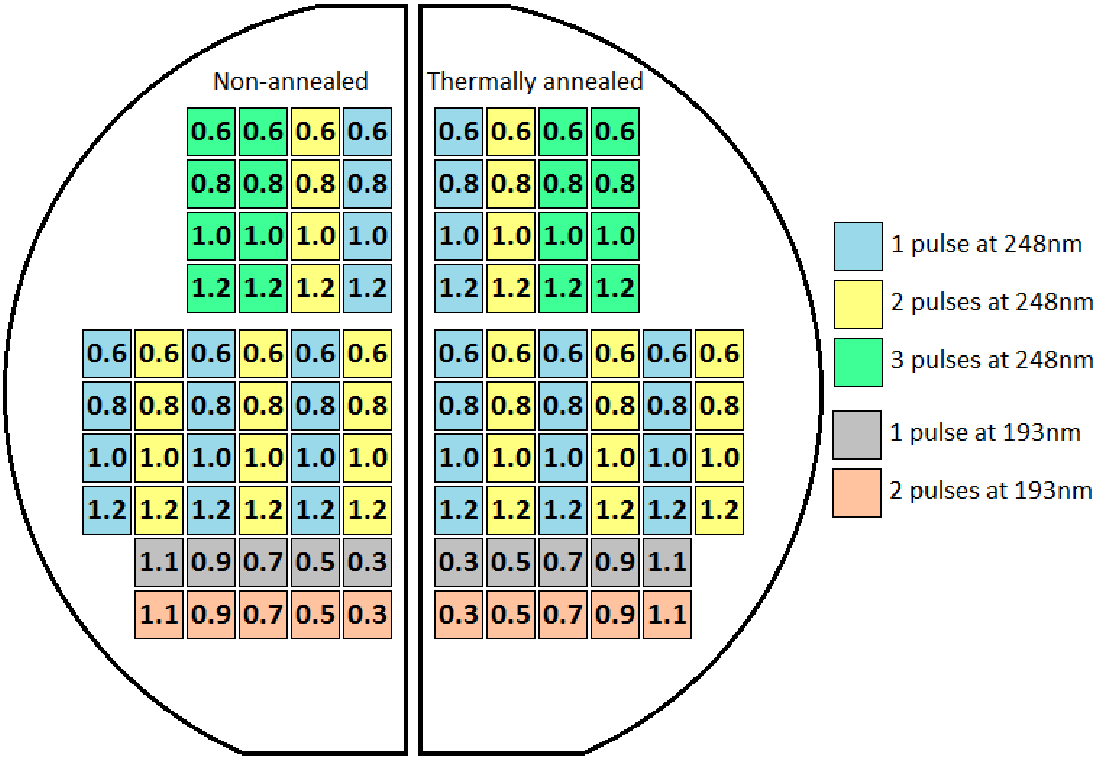

Figure 4.13 - Layout of laser processed ACTFEL devices on Si wafer, number indicates fluence in J/cm^2

4.2.3 Optical Characterisation

The luminance vs Voltage curves for the devices laser annealed at 193nm and those laser annealed followed by thermal annealing are shown in Figure 4.14. A non-annealed and a thermally annealed only device are also shown as a reference. The devices were driven using a 1kHz bipolar trapezoidal waveform with a 5Vp-p increase every 5 seconds, a 1.5kΩ series resistor was used for current protection.

4.3 Results and Discussion

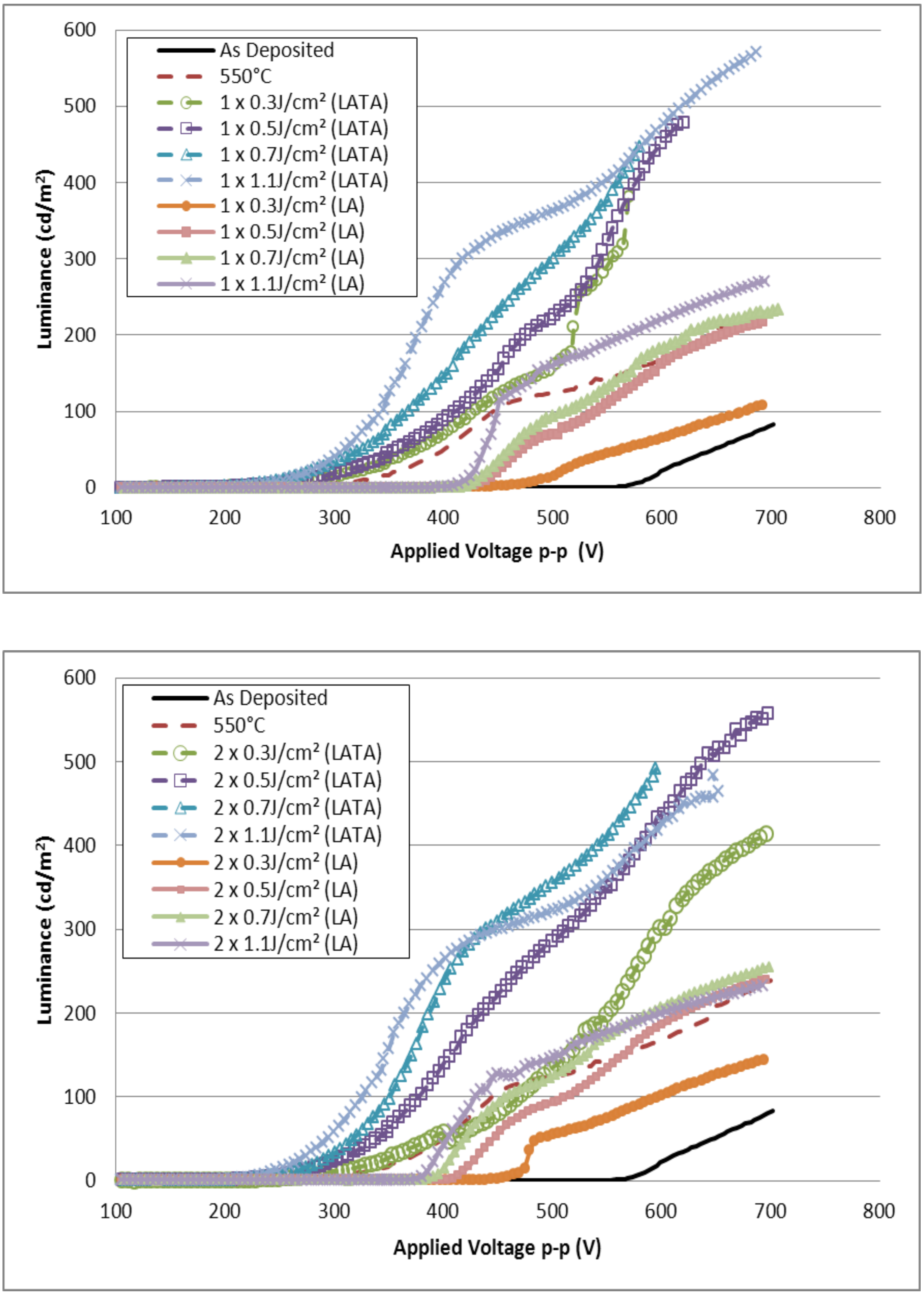

Figure 4.14 - Luminance vs voltage curves for devices laser annealed (LA) at 193nm and laser followed by thermal annealing (LATA) at 550°C at various fluences with 1 pulse (top) and 2 pulses (bottom)

The L-V results clearly demonstrate that laser annealing at 193nm is of benefit to the luminescent characteristics of ZnS:Mn thin films as with 248nm. The results are further improved when laser annealing is followed by thermal annealing. The maximum achievable luminance of a device laser annealed at 1.1J/cm^2 and then thermally annealed is improved by as much as 8 times that of the non-annealed devices and double that of a device subjected to either laser or thermal annealing.

The use of laser annealing only to the devices yields similar results to thermal annealing, with the exception of 0.3J/cm^2. The increasing of the fluence has little effect on the maximum achievable luminance, with only a small increase noticeable. The increase in luminance as a function of the applied voltage becomes steeper as the fluence is increased for both one and two pulses, this is a common occurrence and a result of the structural reordering that occurs during the annealing process. The threshold voltage decreases with increasing fluence, this is due to the ablation that occurs during processing. The pressure cell which the device is held in limits the amount of material removed but does not stop it completely. The higher the fluence and the number of pulses the more material is ablated therefore lowering the threshold voltage as the phosphor layer becomes thinner requiring a lower electric field for emission to ensue. Ablation may not be the only cause of the threshold drop however as the reduction is greater than would be expected for the amount of material that is removed. Another possible cause is that the interface trap states are altered by laser annealing. A continuous distribution of interface trap states could be formed at the phosphor/insulator interfaces which have been shown theoretically to have a lower threshold voltage than for discrete state distribution. The density of the continuous states can also affect the sharpness of the L-V curves, the lower the distribution the lower the energy the electrons are likely to have, therefore they are less likely to achieve the energy required to cause impact excitation of the luminescent centres. This leads to shallow L-V curves (94).

Laser annealing followed by thermal annealing demonstrates a large improvement on the L-V characteristics, the luminance achieved is greater and the turn on is much sharper. For the one pulse devices at the lower voltages, below 500Vp-p, the luminance increases with the increasing fluence. Above 500Vp-p, the luminance of the lower fluence devices gradually attain almost the same luminance as the highest fluence device; 1.1J/cm^2, while the L-V curves become steeper and shallower respectively. The two pulse curves follow a similar pattern, but below 400Vp-p. Above this value the three lower fluences, 0.3, 0.5 and 0.7J/cm^2, all continue to steadily increase with the higher fluences having the higher luminance values. However, regarding the highest fluence; whilst the luminance is still increasing with the rising applied voltage, the L-V curve becomes shallower and gradually the lower fluences become brighter. As with the laser annealed only devices, there is a negative shift in the threshold voltage, with increasing fluence due to the phosphor ablation. There is a substantial shift in the threshold voltage for the devices that are subjected to thermal annealing, they have a very shallow rise in luminance as a function of the applied voltage initially. This has been attributed to the creation of shallow interface states during the thermal annealing process.

For the results shown in Figure 4.14 not all the curves reach the maximum applied voltage of 700Vp-p, this is due to these devices suffering a catastrophic breakdown during the turn on process. These devices, along with the other devices shown in Figure 4.13 that are not included in Figure 4.14, demonstrated the same turn on behaviour and the shape of the L-V curves. There is a certain amount error between each device; this was however no greater than 10% of the luminance at a given voltage.

One of the most noticeable characteristics of the L-V curves is the double plateau that the laser followed by thermal annealing devices exhibit. This becomes more prominent the higher the fluence. One possible explanation for this is the existence of two different trap distributions of the top and bottom phosphor/insulator interfaces (95). The first plateau can be attributed to the effects of the laser annealing at the top interface region as it is subjected to higher temperatures during the laser annealing process. The second plateau is due to the bottom insulator/phosphor interface, which is not affected by the laser processing. This is due to the laser energy only penetrating approximately 100 nm in to the phosphor layer, due to optical absorption. This is corroborated by the fact that the samples that were treated to only one annealing process do not display a double plateau. Another possible explanation for the double plateau is that as the applied voltage is increased and therefore the electric field across the phosphor is increased electrons could be emitted from deeper interface states (96). The depth of the interface states can be found using the Poole-Frenkel emission (97);

$$\Delta\emptyset_{PF} = \frac{e^{3}}{\pi\varepsilon_{o}\varepsilon_{r}}^{\frac{1}{2}} E^{\frac{1}{2}} \tag{4.1}$$

Where e is the elementary charge (1.602 x 10^{-19}), ε_o is the permittivity of vacuum (8.85 x 10^{-12} F/m), ε_r is the dielectric constant of the phosphor layer and E is the electric field. Unfortunately in order to calculate the electric field (equation 2.2) the thickness of the phosphor layer is required which due to the laser ablation is unknown. An estimated material ablation of the devices has been made using the study carried out by Mastio et al (98) on 248nm, the ablation has been estimated to be 25nm for 0.3J/cm^2, 35nm for 0.5J/cm^2 and then 50nm, 55nm and 60nm for 0.7, 0.9 and 1.1Jcm^2 respectively. However until this can be verified by an ablation study of 193nm as detailed in the future work section these are a best guess estimate and therefore any calculations based on them would be unreliable and prone to error.

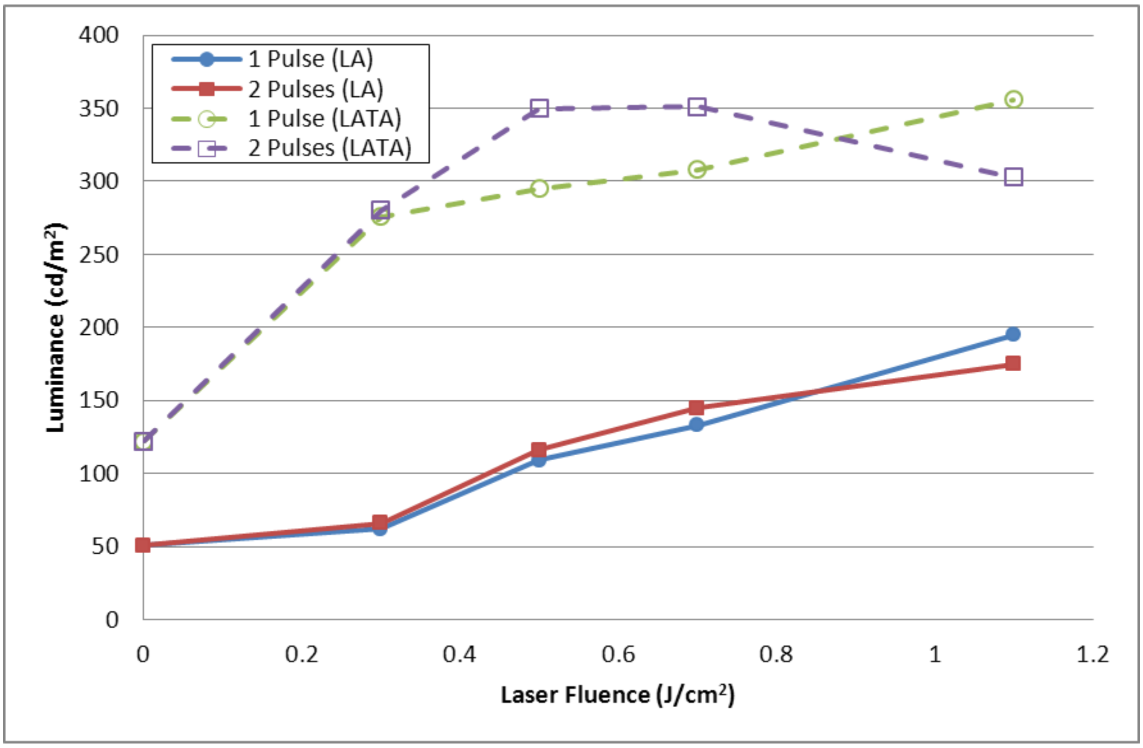

Figure 4.15 - Luminance 100Vp-p above knee as a function of laser fluence for devices laser annealed at 193nm and laser followed by thermal annealed at 550°C for single and double pulses at various fluences.

Figure 4.15 shows the luminance as a function of the laser fluence at a voltage of 100Vp-p above the knee; where there is a double plateau the first knee point is used. The knee point is where a 45° line, moving positively along the x-axis, first intersects with the L-V curve and 100Vp-p is used as this would be the operating voltage of the device. This method is used, opposed to the threshold voltage +100Vp-p, due to the initial shallow turn on of the devices. The laser annealing alone sees an almost fourfold increase in the luminance when compared to an as deposited device. At a fluence of 0.7J/cm^2, the luminance is comparable to devices thermally annealed. At higher fluences the luminance is increased further. The number of pulses has little effect on the luminance of the laser annealed only devices, with the luminance being almost identical for the one and two pulses at all fluences. A slight improvement is seen in the one pulse at the highest fluence compared to the two pulse device. For the devices which are laser annealed then thermally annealed; for the lowest fluence, the luminance is virtually equal for the one and the 2 pulses. For the next two fluences, 0.5 and 0.7J/cm^2, the 2 pulse luminance is brighter than for the one pulse, although there is little or no improvement in luminance between the two fluences for both pulses. For the highest fluence, two pulses has a detrimental effect on the luminance as it is reduced from the value achieved by 0.7J/cm^2. Annealing at a wavelength of 248nm also has a similar detrimental effect on the luminance when two pluses are used at higher fluences (36).

The best results obtained for both annealing processes used 1 pulse at 1.1J/cm^2, with the laser annealed alone device having an almost fourfold increase in luminance at 680Vp-p when compared to an as deposited device. The luminance was slightly improved in comparison to a thermally annealed device. The laser followed by thermal annealing shows a sevenfold increase in luminance compared to an as deposited device at 680Vp-p, and a two and a half times increase in luminance in comparison to a device thermally annealed. The sharpness of the L-V curves is also improved by laser annealing.

The benefits of laser annealing at 248nm on the electroluminescence of ACTFEL devices has been demonstrated by NTU resulting in the award of 3 doctorates (36, 43, 44). More recently, the benefits of laser followed by thermal annealing has been demonstrated (93). For this reason, only the key results of 248nm are presented in order to allow for a comparison between the two wavelengths.

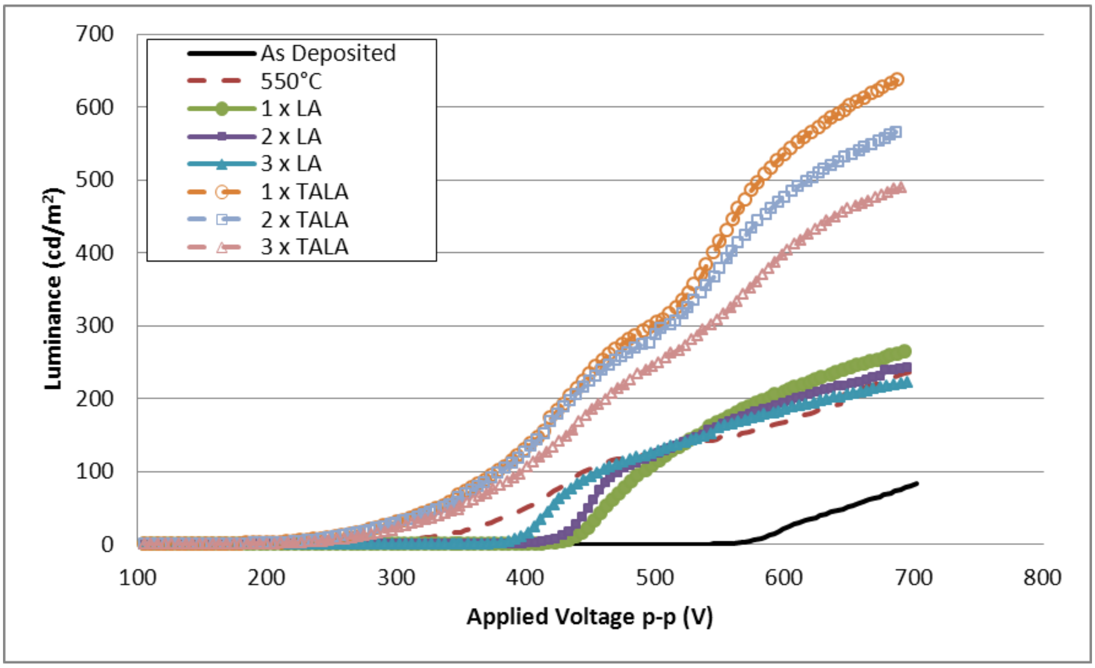

Figure 4.16 - Luminance vs voltage curves for devices laser annealed (LA) at 248 nm and laser followed by thermal annealing (LATA) at 550°C at 1J/cm^2 for 1, 2 and 3 pulses.

Figure 4.16 shows the L-V curves of devices that have been laser annealed at 1J/cm^2 using a wavelength of 248nm for one, two and three pulses. It also shows results from devices laser annealed under the same conditions that have then been thermally annealed. Both the annealing treatments demonstrate the same behaviour, that is, the maximum achievable luminance decreases with increasing pulses. It is also observed that the initial rise in luminance as a function of the applied voltage is steeper. As with the 193nm devices, the threshold voltage is reduced by the thermal annealing due to the creation of shallow traps, where the higher the anneal temperature and duration the larger the threshold voltage decrease (95). Again, the further reduction in threshold voltage due to the laser annealing can be attributed to surface ablation that occurs during the laser annealing process; three pulses at $1J/cm^2$ can ablate as much as 150 nm (54) from the phosphor layer, the threshold voltage reduces with increasing pulses.

The luminance as a function of the laser fluence is shown in Figure 4.17 for all fluences and number of pulses for the devices subjected to laser annealing at 248nm when operating at a voltage 100Vp-p above the knee point (V_{opp}). Unlike for those at 193nm, the laser annealed only devices show a distinct difference in luminance between the number of pulses applied for each fluence. Also, all laser annealed devices have a higher luminance than thermally annealed devices, although 193nm starts at a lower fluence. Use of two pulses gives the best luminance across all fluences, although there is little difference between the four fluences. After a slight increase from 0.6 to $0.8J/cm^{2,}$ annealing at higher fluences has a detrimental effect. Use of three pulses yields the lowest luminance for all four fluences, the peak performance being at $1J/cm^2$, which is the same for the one pulse devices. The highest fluence of $1.2J/cm^2$ had a detrimental effect on the luminance for both single and triple pulses, for the triple pulse this is most likely due to a combination of material ablation (98) and the heat that is dissipated through the phosphor layer during the laser annealing process. The triple pulse at the higher fluences could generate enough heat (99) to alter electrical properties of the bottom insulator.

The results for the devices that were laser annealed followed by thermal annealing show that the one pulse device performed the best with regards to luminance. The performance of the one pulse dips slightly form the 0.6 to the $0.8J/cm^2$ device before the $1J/cm^2$ equals the $0.6J/cm^2$ device performance, the $1.2J/cm^2$ then exceeds them all. The two pulse devices steadily increase in luminance before the final fluence, 1.2J/cm^2, causes a detrimental effect and the luminance achieved is the lowest of the two pulse devices. Three pulses followed by thermal annealing demonstrates no obvious trend. The 0.6J/cm^2 device luminance is only slightly lower than that for two pulses, the device subjected to 0.8J/cm^2 however has a large drop in luminance, ~ 40cd/m^2 unlike the two pulses which improved. For the other two fluences, 1 and 1.2J/cm^2, the luminance increases slightly before the highest fluence results in another decrease. The 0.6J/cm^2 luminance is the highest achieved for the three pulse devices followed by thermal annealing.

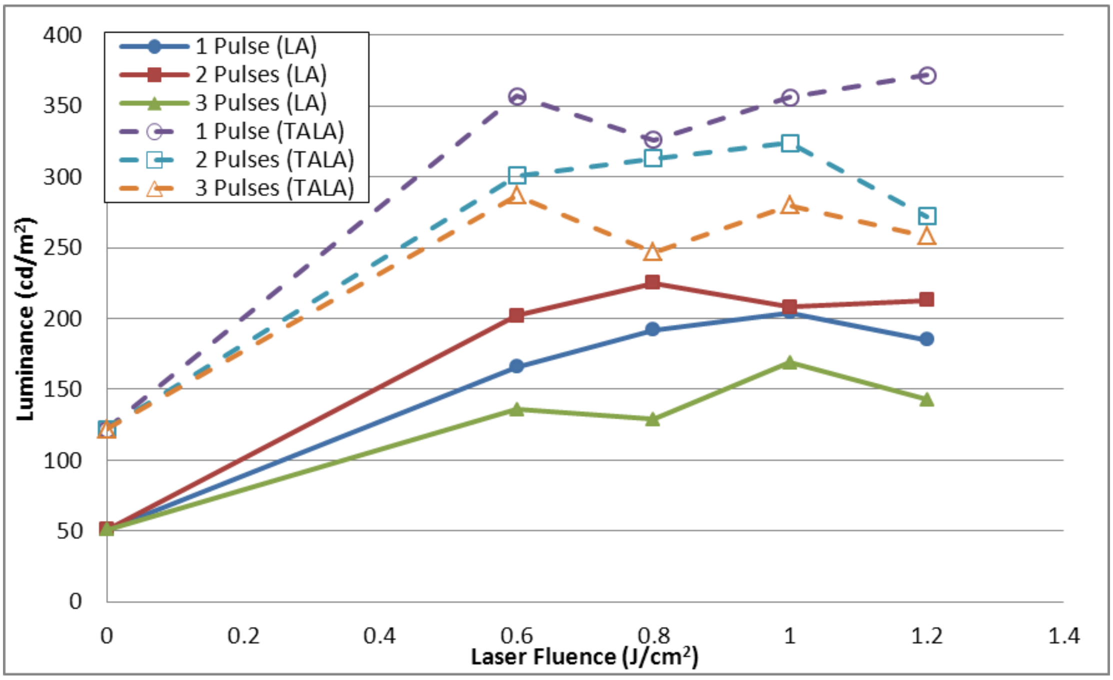

Figure 4.17 - Luminance as a function of laser fluence at V_{opp} for devices laser annealed at 248nm and laser followed by thermal annealed at 550°C for single and double pulses at various fluences.

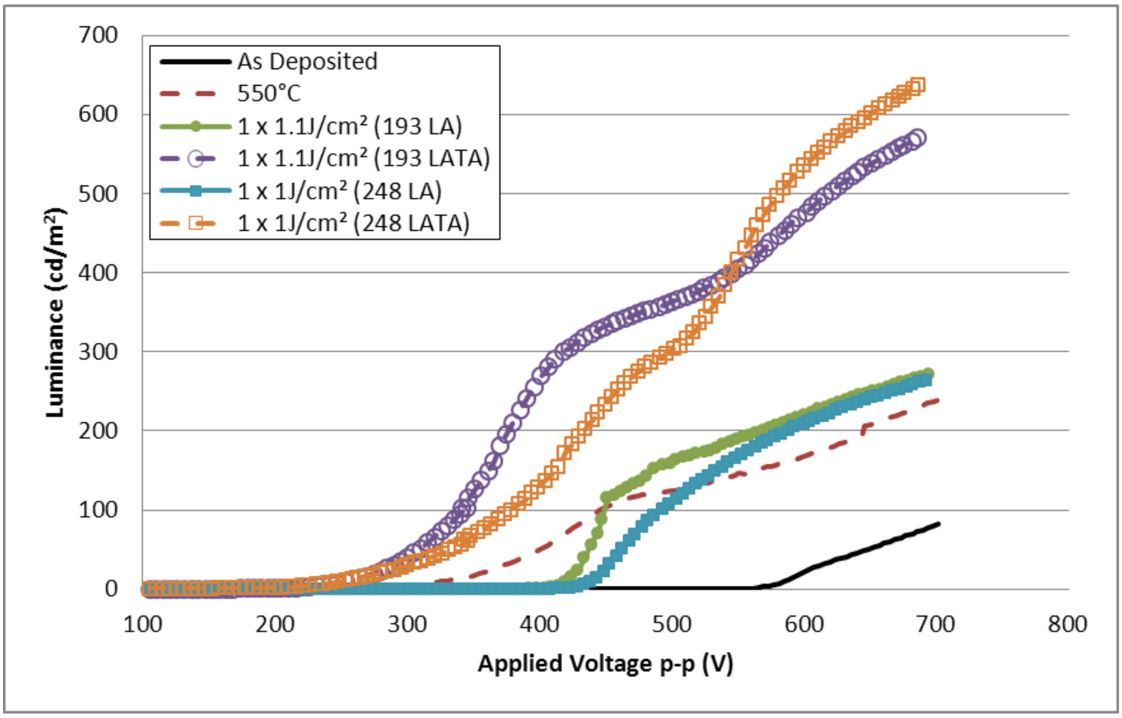

Figure 4.18 - Luminance vs. voltage curves for devices laser annealed at 193nm and 248nm and laser followed by thermal annealing at 550°C.

The L-V curves for samples laser annealed and those laser followed by thermally annealed at 1.1J/cm^2 and 1J/cm^2 for ArF and KrF excimer emission respectively (single pulse) are shown in Figure 4.18. Whilst the KrF laser followed by thermal annealing device may have a higher maximum achievable luminance, by 12%, the ArF sample has a sharper turn on. The laser annealed only devices have almost identical maximum luminance, however, the ArF device again has a sharper turn on characteristic. Both outperform the thermally annealed sample. Table 4.1 details the key information of the devices compared in Figure 4.18.

Device	V_{th}	V_{opp}	L_{opp}	Maximum Luminance	Comment
As Deposited	560	650	51	69	Low luminance, shallow turn-on, high threshold voltage.
550°C	240	488	122	226	Moderate luminance, shallow turn-on, low threshold voltage.
KrF	400	592	204	259	Moderate luminance, moderate turn-on, moderate threshold voltage.
ArF	418	558	195	265	Moderate luminance, sharpest turn-on, moderate threshold voltage.
KrF + 550°C	184	530	356	631	Highest luminance, moderate turn-on, low threshold voltage.
ArF + 550°C	199	488	356	565	High luminance, sharp turn-on, low threshold voltage.

Table 4.1 - Summary of results presented in Figure 4.18, where V_{th} is $1cd/m^2$, V_{opp} is the operating voltage (100Vp-p above the knee point), L_{opp} is the luminance at this point and the maximum luminance is taken at 680Vp-p.

4.4 ITO Failure

The main aim of this study was to examine the characteristics of devices with novel structures and processing methods over their lifetime. The laser annealed devices discussed previously were fabricated with the intention of carrying out such experiments. Unfortunately, despite several attempts, this was not possible due to the failure of the top transparent indium tin oxide (ITO) electrode.

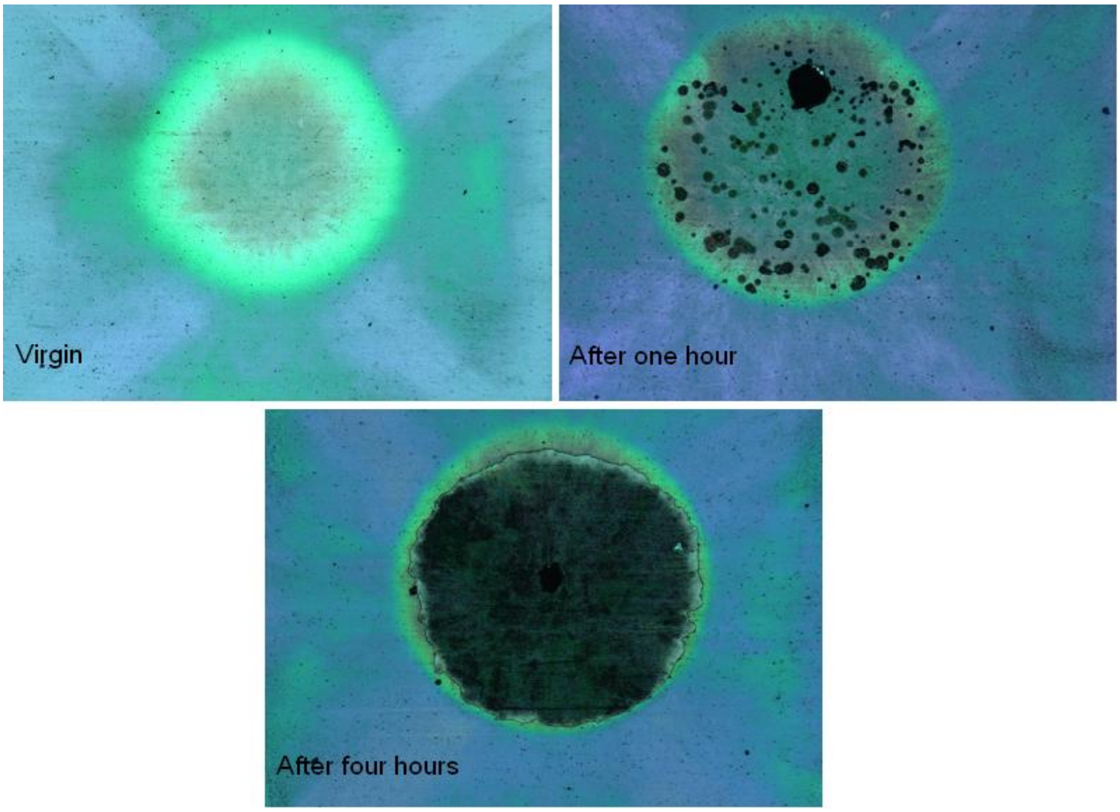

Figure 4.19 - Pictures of the top ITO layer after device operation

The pictures shown in Figure 4.19 detail the total failure of the ITO as a transparent electrode, the ITO has not broken down electrically as light could be seen around the edge of the dot which is not shown in the pictures as the device was off. During the first hour of operation tiny dark spots slowly appear on the surface, as shown in the top right photo, as the time of operation is increased the spots gradually increase in size joining up to create large dark patches. After four hours of operation the entire surface of the electrode is opaque and no light can be seen through it, as shown in the bottom photo. The cause for the discolouration is unclear as the system has previously produced high quality ITO that has not demonstrated the same failure, contamination of the chamber is the most likely cause.

4.5 Conclusions and Discussion

The use of ArF laser annealing as a post deposition annealing process for ZnS:Mn thin films deposited by RF magnetron sputtering has been presented and compared to KrF laser annealing. All samples tested were fabricated on the same wafer allowing for direct comparison. The effects of KrF and ArF pulsed UV laser annealing with multiple irradiations at various fluences, as well as the combination laser and thermal annealing has been demonstrated. The optimum result was found to be the combination of thermal and laser annealing, with a single KrF pulse at 1J/cm^2. Laser annealing with KrF or ArF was found to yield very similar maximum achievable luminance results, with a marginally better performance from KrF laser annealing. However, the main benefit of using ArF is the sharpness of the first plateau, resulting in a higher luminance at lower applied voltages. For example, if the samples were driven at 450Vp-p the ArF sample would yield a luminance over 40% brighter than the equivalent KrF sample. Investigation into the feasibility of combining the two laser emissions in order to fabricate a device with high luminance and a sharp turn on characteristic is required.

Unsuccessful lifetime experiments were carried out on the devices for both laser wavelengths, ACTFEL devices that have been subjected to laser annealing at 248nm have previously demonstrated an improved lifetime characteristic (93), and one of the key aims of this study was to investigate this further. However due to the discolouration of the ITO layer this was not possible. The chamber was opened up and cleaned as the probable cause was contamination Once cleaned several ITO depositions were made prior to deposition on devices that were clear and assumed to be of good quality, unfortunately this process made no difference to the quality. In order to try and combat the discolouration specialised silicon sprays and oils were purchased in order to protect the ITO during operation as it was believed that the ambient gases were reacting with the ITO during current conduction. While this slowed the process down it did not eliminate it. A possible solution to the issue is to have overlapping aluminium and ITO electrodes allowing the ITO to be coated with silicon immediately after deposition in order to eliminate any reactions. This was not pursued due to time constraints but is a consideration to be taken forward as the quality of the ITO cannot be guaranteed.

5. Laser Annealing of High Target Utilisation Sputtering (HiTUS) Devices

5.1 Introduction

High target utilisation sputtering (HiTUS) is a form of physical vapour deposition (PVD) developed by Plasma Quest Limited (PQL). Unlike RF magnetron sputtering the plasma is generated away from the target removing the need for local magnets that cause a non-uniform material distribution from the surface. As the name would suggest, HiTUS uses 90% of the target compared to just ~35% for Magnetron sputtering. A schematic of the deposition system can be seen in Figure 5.1. The high density plasma (10^{13} ions/cm^3) (100) is generated in a side arm adjacent to the chamber, known as the plasma launch system (PLS), this consists of a quartz tube surrounded by a copper RF coil antenna. The plasma is then enhanced by an electromagnet at the exit of the PLS, where it is directed on to the target by the steering electromagnet located behind it. This produces a high density of argon ions in the region directly above the target. In order for the argon ions to have sufficient energy to sputter, a negative DC bias is applied to the target. This results in a high current density over the full surface of the target, allowing uniform material loss across the entire surface area. HiTUS virtually eliminates target poisoning resulting in a more stable process, allowing for higher deposition rates of dielectrics and semiconductor materials.

The following chapter details experiments carried out as part of a NTU collaborative project with PQL, it focuses on the use of an alternative sputtering method that can produce ACTFEL devices at low temperatures on transparent flexible substrates and the enhancement of the luminescent properties when processed with laser annealing. Presented first is a study carried out on a hybrid wafer followed by a series of experiments carried out on glass and plastic samples.

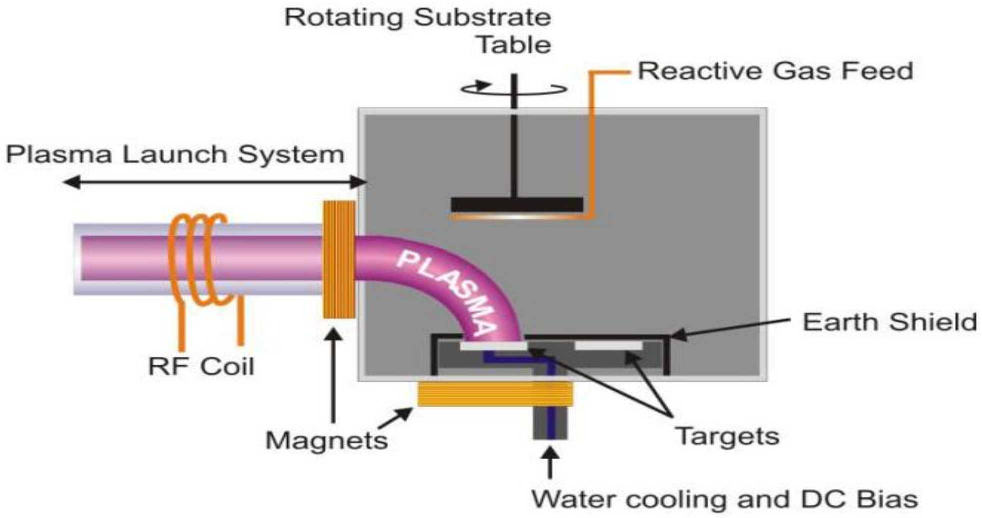

Figure 5.1 - Schematic diagram of the HiTUS system (101)

5.2 NTU – HiTUS Hybrid Wafer

The hybrid wafer consists of devices that have a ZnS:Mn layer deposited by HiTUS and Y_2O_3 and ITO deposited by RF magnetron sputtering.

5.2.1 Experimental Details

5.2.1.1 Deposition Parameters

The HiTUS ZnS:Mn deposition was executed by Dr. Steve Wakeham at PQL who provided the deposition parameters, the base pressure was set at 4.5 x

10^{-5} mbar, the RF and DC power was 1.2 and 0.2 kW respectively, the substrate temperature was less than 40°C and the deposition rate was 44nm/min. The Hybrid dielectric layers were deposited at NTU at a temperature of 190°C in 0.4 Pa of Ar under a base pressure of 1 x 10^{-4} Pa, ITO electrodes for all devices were deposited at RF power 50Watt under 2mTorr sputtering pressure and in 0.2% oxygen in Argon at room temperature. The bottom dielectric layer only was thermally annealed for one hour at 500°C prior to being sent to PQL for the HiTUS deposition. The fabricated devices were of the structure Y_2O_3/ZnS:Mn/Y_2O_3/ITO with the thicknesses 300/800/300/100nm respectively. This is a continuation of the work presented in (94).

5.2.1.2 Laser Annealing

The laser used for the HiTUS samples was a Lambda Physik LPX 305i excimer laser charged with Krypton Fluoride (KrF) for 248nm. The laser emits 20ns pulses at a frequency of 1kHz when more than one pulse is applied. The laser annealing was undertaken by Dr. Costas Tsakonas at the NTU research facility. The devices were laser annealed at 248nm at fluences of 0.4, 0.8, 1, 1.2, 1.4, 1.6 J/cm^2 for single, double, triple and quadruple laser irradiations, as shown in Figure 5.2. The laser annealing of the phosphor layer was carried out prior to the deposition of the top dielectric.

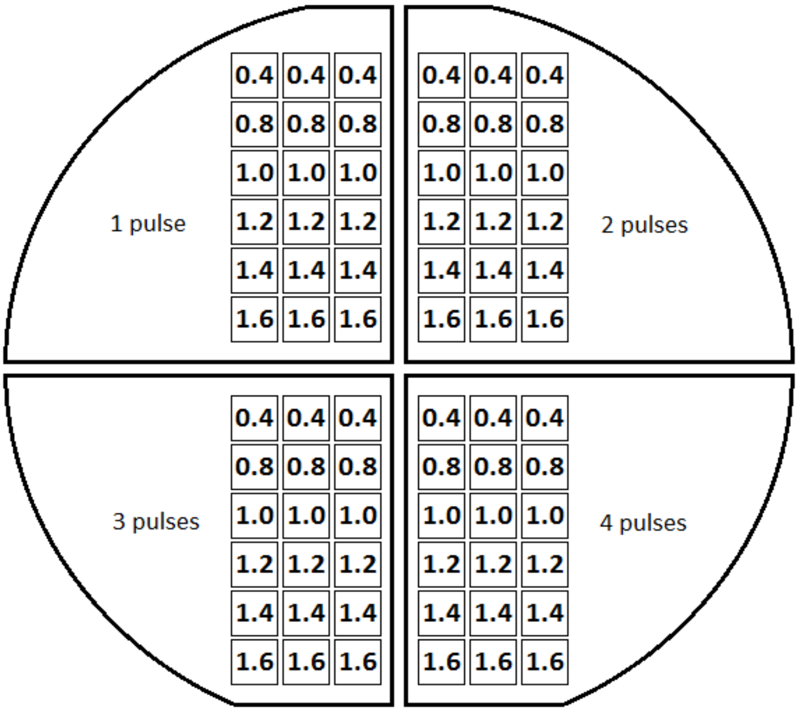

Figure 5.2 - Layout of laser processed hybrid devices on Si wafer, number indicates fluence in J/cm^2

5.2.1.3 Optical Characterisation

The L-V results are shown in Figure 5.3, the devices were driven using a 1kHz bipolar trapezoidal waveform with a 10Vp-p increase every 3 seconds, a 1.5kΩ series resistor was used for current protection. There are no results for 1.6 J/cm^2 for three and four pulses as they were damaged during the fabrication process. An as deposited device is included in all graphs for reference, please note in this instance it refers to a device with the bottom dielectric layer that has been thermally annealed.

5.2.2 Results and Discussion

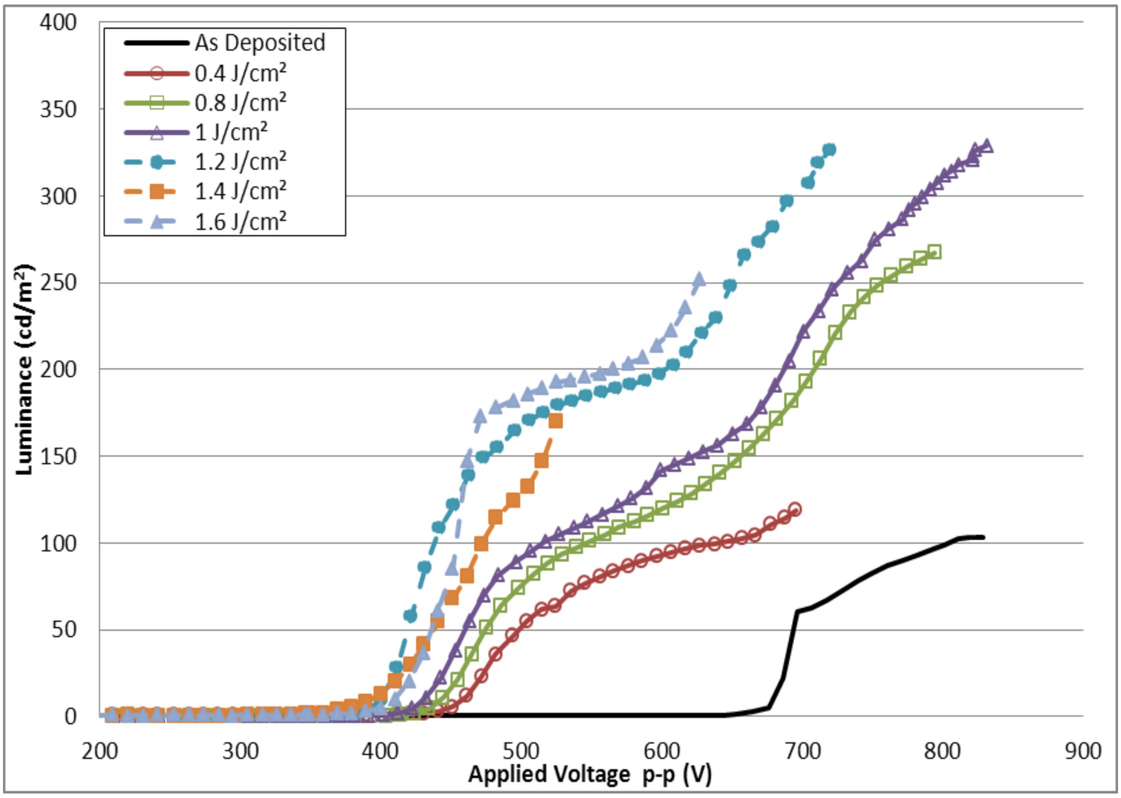

Single Pulse

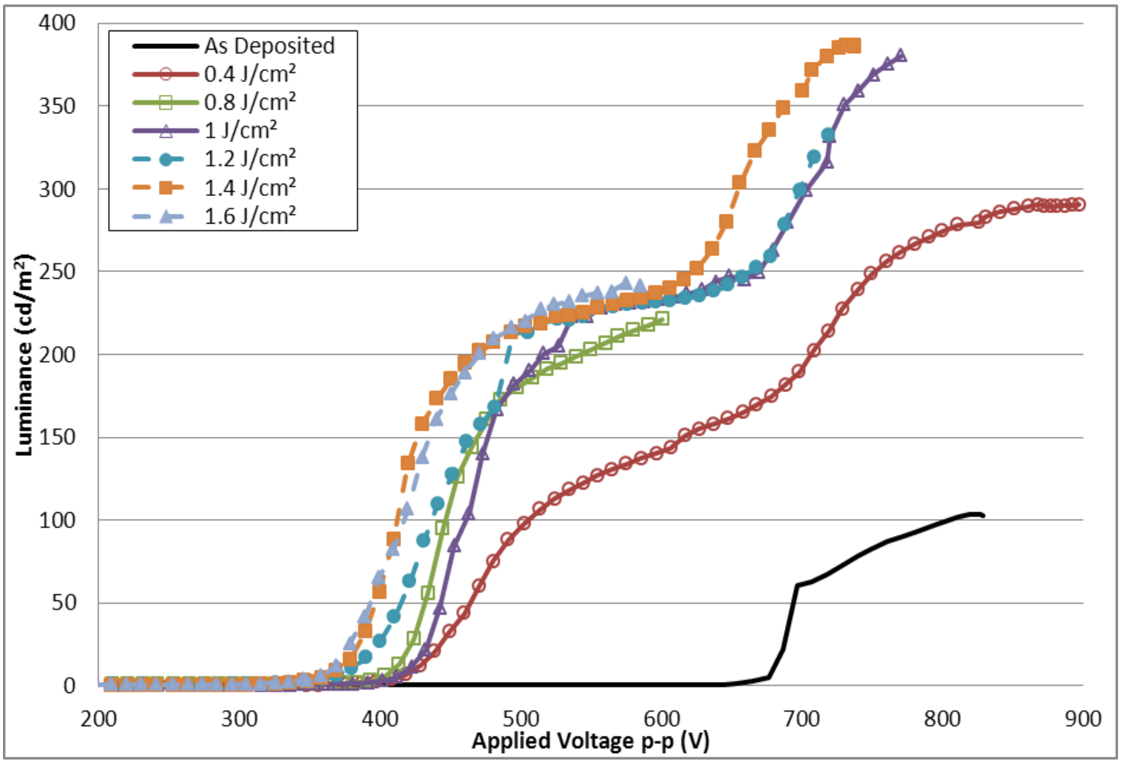

Double Pulse

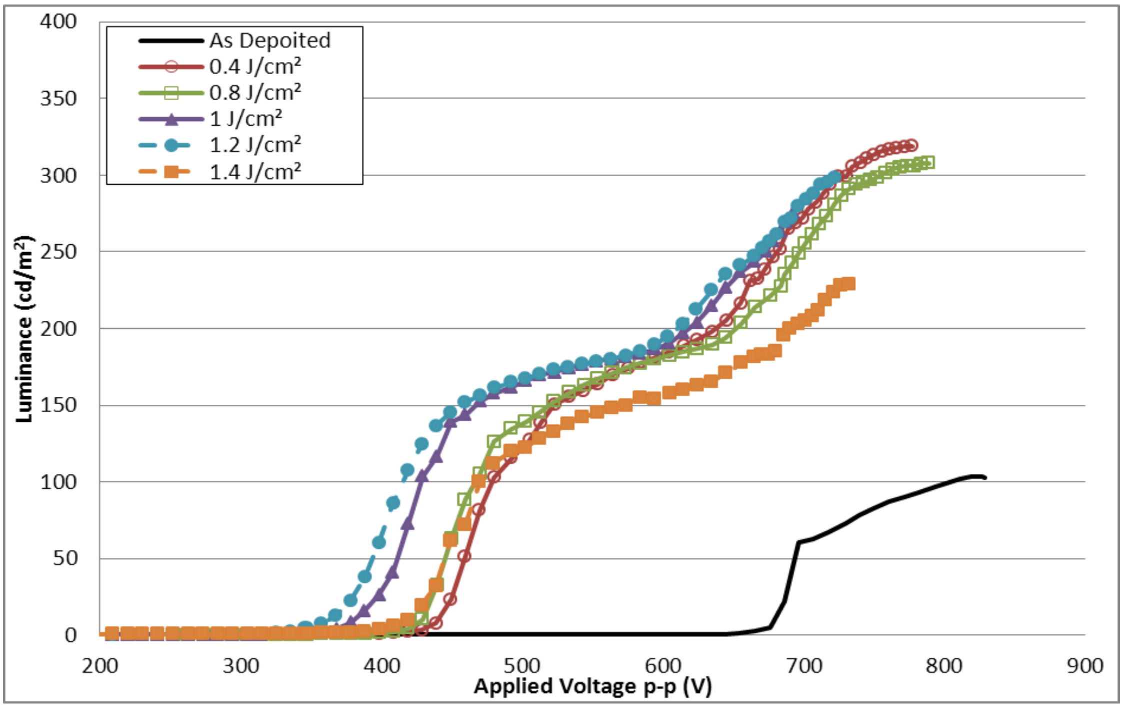

Triple Pulse

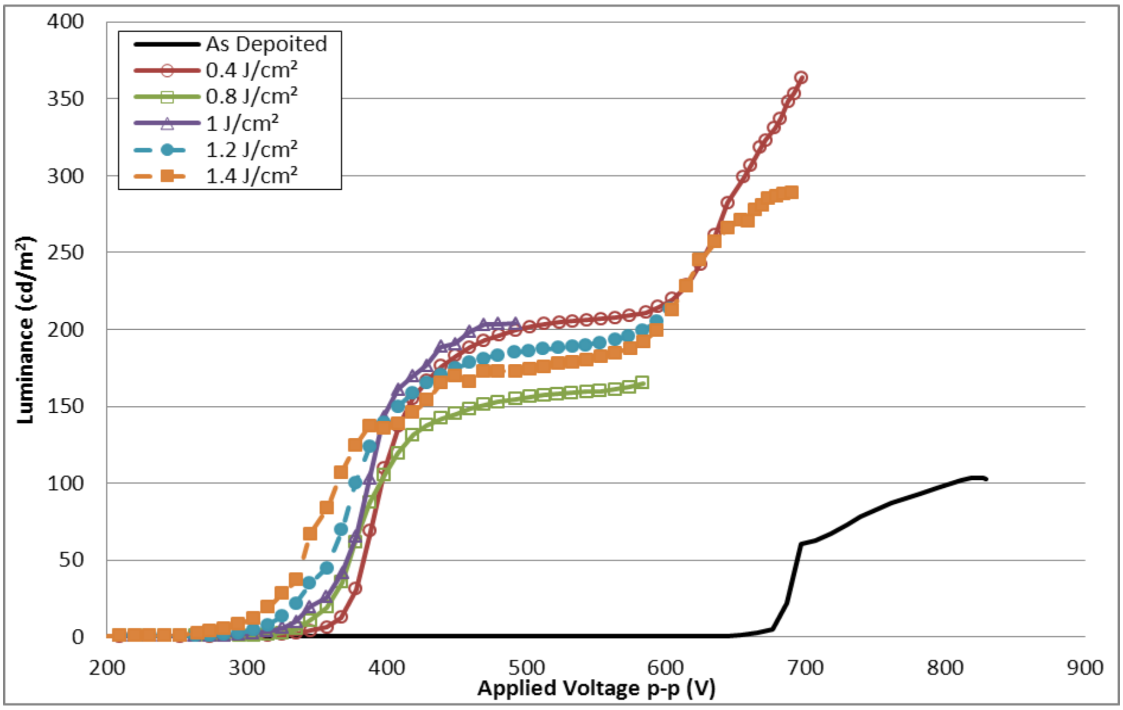

Quadruple Pulse

Figure 5.3 - Luminance vs voltage curves for hybrid ACTFEL devices laser annealed at various fluences for single, double, triple and quadruple irradiations.

There is an undisputable rise in luminance for all the laser annealed devices when compared to an as deposited device. For the single and double pulses, the L-V characteristics tend to improve with the increasing laser fluence. For the triple irradiation devices, with the exception of the 1.4 J/cm^2 device, this is initially also the case, for the quadruple pulse there is no clear trend. These devices also show a double plateau which becomes more prominent the higher the fluence and the number of pulses. The four pulse devices clearly demonstrate an initial rise in luminance with increasing applied voltage before plateauing off for ~150Vp-p and then rising again as the applied voltage is further increased. The double plateau is more evident in the hybrid devices than the previous NTU fabricated devices. With the phosphor/insulator interfaces being subjected to two very different heat treatments, it would suggest the explanation discussed previously is correct; that the two distinct rises in luminance are down to the different heat treatments of the interfaces. Although this characteristic is still not fully understood, work is still on going to determine the underlying mechanism. For the one and two pulse devices, the sharpness of the initial rise in luminance is improved with increasing laser fluence. For the three pulse devices, the sharpness is consistent throughout the range of fluences. For the four pulse devices, the rise becomes shallower as the fluence is increased. The second rise in luminance tends to be slightly shallower for all the devices in comparison to their initial rise.

The best result in regards to maximum achieved luminance at 700Vp-p is observed for 0.4 J/cm^2 and four pulses at 363 cd/m^2. The one pulse achieved 307 cd/m^2 at 1.2 J/cm^2, the two pulse achieved 359 cd/m^2 at 1.4

J/cm^2, the three pulse achieved 284 cd/m^2 at 1.2 J/cm^2 and the as deposited devices had an average luminance of 59 cd/m^2.

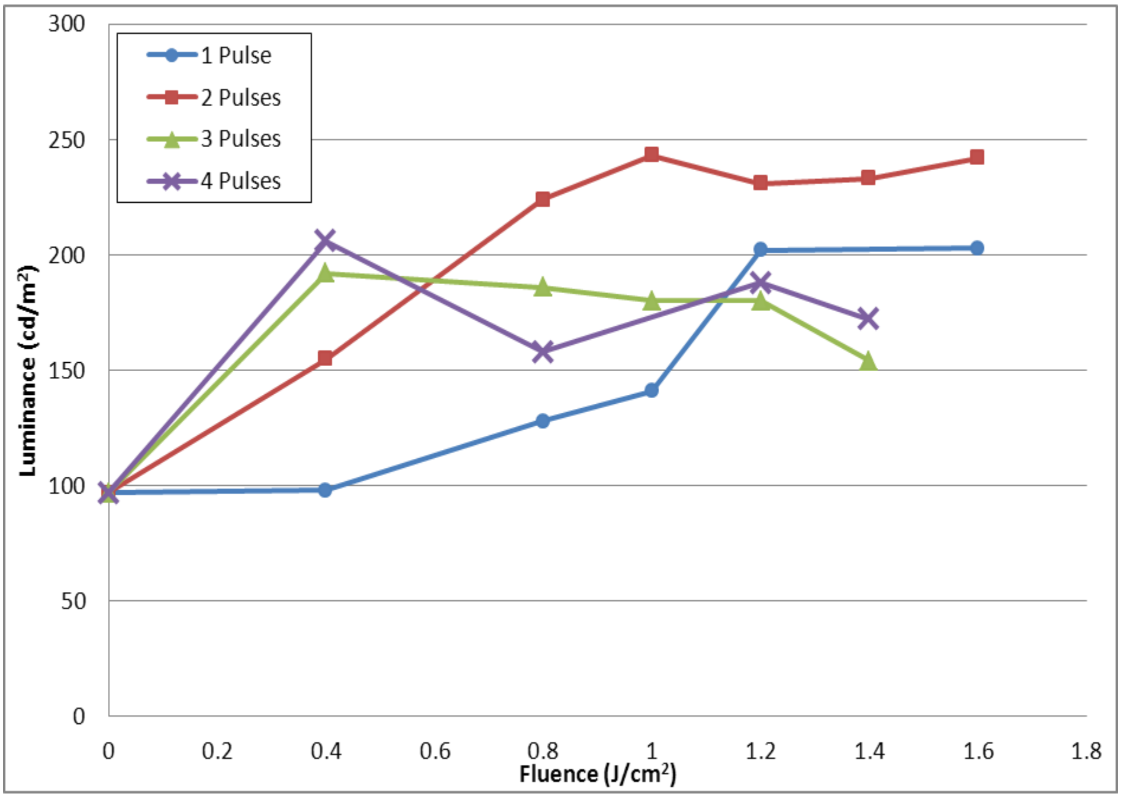

Figure 5.4 - Luminance as a function of laser fluence when driven at Vopp for hybrid devices processed with single, double, triple and quadruple irradiations.

Although the four pulse device achieved a higher luminance when the operating voltage is taken into consideration, the two pulse devices clearly yield the best results as demonstrated in Figure 5.4. The one pulse devices show an increase in luminance with increasing fluence, but annealing higher than 1.2 J/cm^2 shows little benefit. The two pulse devices peak at 1J/cm^2 with the higher fluences showing to have a slightly detrimental effect on the luminance. The three and four pulse devices both yield the best result at 0.4

J/cm^2, with the three pulse devices gradually deteriorating as the fluence is increased.

5.3 HiTUS Glass and Plastic Substrates

After a series of successful experiments depositing HiTUS materials at room temperature, full EL stacks were then deposited on temperature sensitive substrates: glass and plastic. The plastic substrate used was planarised polyethylene naphthalate (PEN) with a thickness of 125 µm supplied by Dupont Teijin Films. The devices grown on these substrates use a different dielectric material, hafnium oxide (HfO_2) and aluminium oxide (Al_2O_3) nano-laminate layers. The nano-laminate structure, which consists of alternating layers of two dielectric materials with different strengths, HfO_2 with a high dielectric constant and Al_2O_3 with a high breakdown strength, can be used together to produce a better performing dielectric layer (102).

5.3.1 Experimental Details

5.3.1.1 Deposition Parameters

All HiTUS depositions were carried out by Dr. Steve Wakeham at PQL, the details of which can be found in table 5.1 for the three materials, ZnS:Mn (0.6wt%), HfO_2 and Al_2O_3.

Material	Base Pressure (mbar)	RF Power (kW)	DC Power (kW)	Substrate Temp. (°C)	Dep. Rate (nm/min)
ZnS:Mn	4.5×10^{-5}	1.2	0.2	< 40	44
Al_2O_3	2.0×10^{-5}	1.5	0.9	< 40	22
HfO_2	2.0×10^{-5}	1.25	0.5	< 40	22

Table 5.1 - HiTUS deposition Parameters

The ITO was deposited at NTU by Dr. Costas Taskonas under the following conditions; RF power 50Watt, 2mTorr sputtering pressure and in 0.2% oxygen in Argon at room temperature.

The structure of the two samples can be seen in Figure 5.5. The configuration of the devices is the standard double insulating structure (ITO/dielectrics/ZnS:Mn/dielectrics/ITO), the thickness of the layers as deposited on to the substrates are 205/340/710/340/100nm respectively as verified by TEM, 340nm is the total thickness of the dielectric layer which is comprised of four layers of ~85nm. The devices were laser annealed at a wavelength of 248nm.

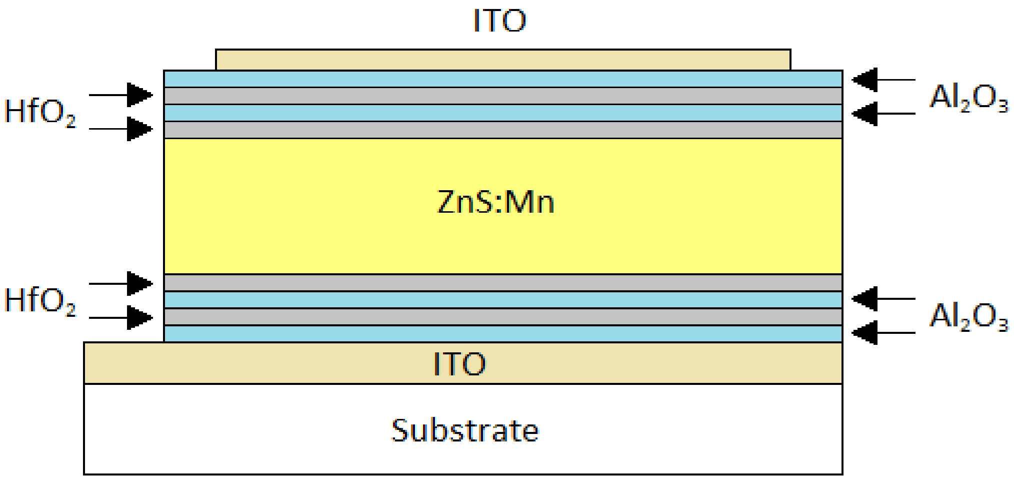

Figure 5.5 - Structural diagram of HiTUS ACTFEL devices grown on glass and plastic

5.3.1.2 Laser Annealing

The laser annealing was carried as detailed previously in section 5.2.1.2. The glass sample was laser annealed at fluences of 1 J/cm^2 for one and two pulses, two pulses at 1.17 J/cm^2 and single pulses at 1.22 J/cm^2 and 1.37 J/cm^2. The plastic sample was laser annealed at fluences of 0.4, 0.6 and 0.8 J/cm^2 for single and double pulses. The layout for both samples can be seen in Figure 5.6, with the top image being the glass sample.

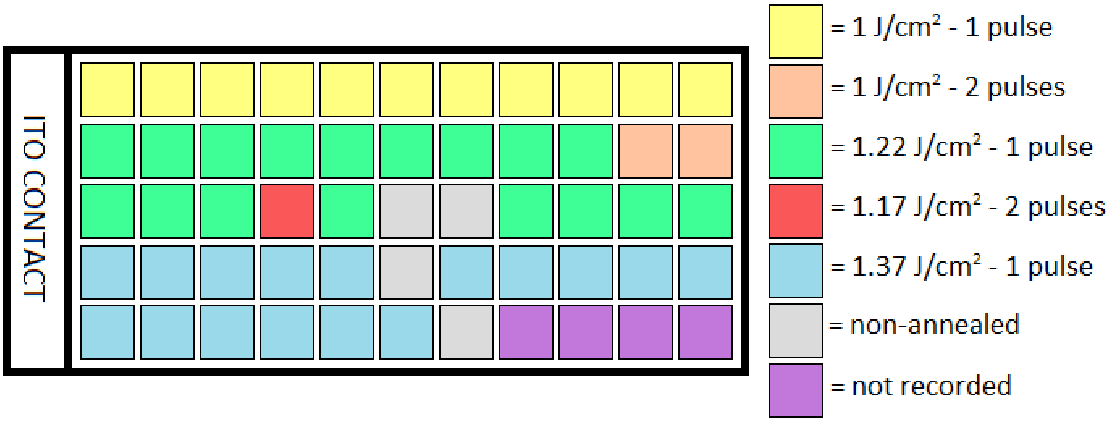

🟨	🟨	🟨	🟨	🟨	🟨	🟨	🟨	🟨	🟨	🟨
🟩	🟩	🟩	🟩	🟩	🟩	🟩	🟩	🟩	🟧	🟧
🟩	🟩	🟩	🟥	🟩	⬜	⬜	🟩	🟩	🟩	🟩
🟦	🟦	🟦	🟦	🟦	⬜	🟦	🟦	🟦	🟦	🟦
🟦	🟦	🟦	🟦	🟦	🟦	⬜	🟪	🟪	🟪	🟪

🟨 = 1 J/cm^2 - 1 pulse
🟧 = 1 J/cm^2 - 2 pulses
🟩 = 1.22 J/cm^2 - 1 pulse
🟥 = 1.17 J/cm^2 - 2 pulses
🟦 = 1.37 J/cm^2 - 1 pulse
⬜ = non-annealed
🟪 = not recorded

Glass Sample

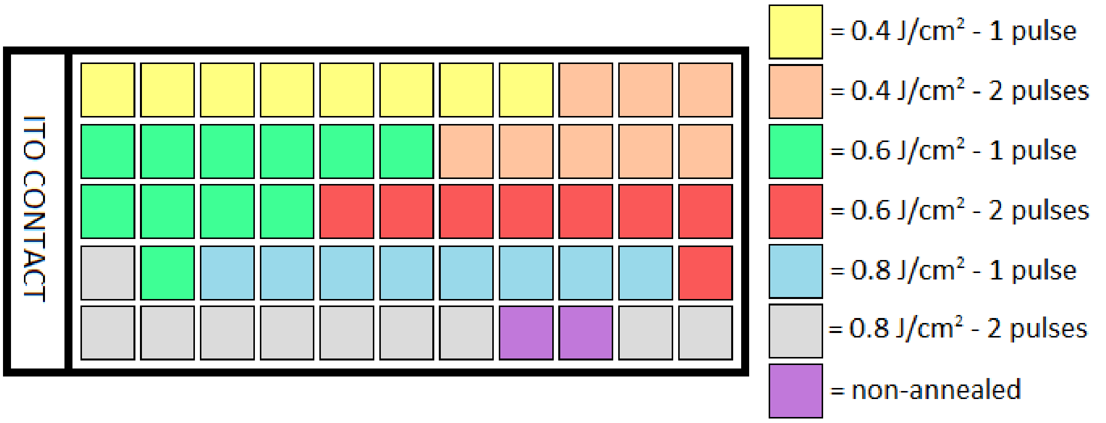

🟨	🟨	🟨	🟨	🟨	🟨	🟨	🟨	🟧	🟧	🟧
🟩	🟩	🟩	🟩	🟩	🟩	🟧	🟧	🟧	🟧	🟧
🟩	🟩	🟩	🟩	🟥	🟥	🟥	🟥	🟥	🟥	🟥
⬜	🟩	🟦	🟦	🟦	🟦	🟦	🟦	🟦	🟦	🟥
⬜	⬜	⬜	⬜	⬜	⬜	⬜	🟪	🟪	⬜	⬜

🟨 = 0.4 J/cm^2 - 1 pulse
🟧 = 0.4 J/cm^2 - 2 pulses
🟩 = 0.6 J/cm^2 - 1 pulse
🟥 = 0.6 J/cm^2 - 2 pulses
🟦 = 0.8 J/cm^2 - 1 pulse
⬜ = 0.8 J/cm^2 - 2 pulses
🟪 = non-annealed

Plastic Sample

Figure 5.6 - Layout of HiTUS ACTFEL devices on glass (top) and plastic (bottom) substrates

5.3.1.3 Optical Characterisation

The devices on both samples were driven with a 1kHz sinusoidal waveform with a 10Vp-p increase every 3 seconds, and had a 100kΩ current limiting resistor in series with the device to help prevent breakdown, the resulting L-V curves are presented in Figure 5.7 (glass) and Figure 5.8(plastic). Not all the devices were tested as a proportion were required for other purposes such as TEM.

5.3.2 Results and Discussion

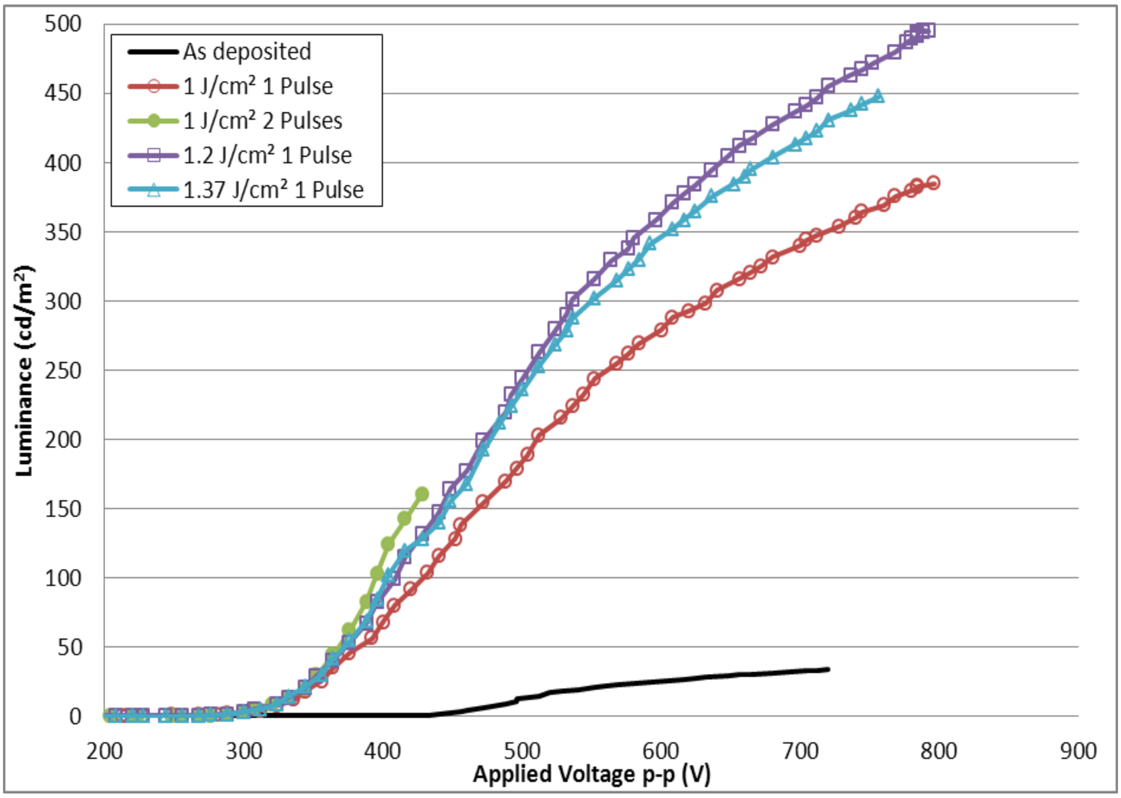

Figure 5.7 - Luminance as a function of applied voltage for ACTFEL devices laser annealed at various fluences deposited on glass.

The luminance characteristics of ACTFEL devices grown on a glass substrate are shown in Figure 5.7. The benefit of the laser annealing on the luminance is particularly evident. The maximum achievable luminance of a laser annealed device is observed to be 441 cd/m^2 for a single pulse at a fluence of 1.2 J/cm^2 when driven at a voltage of 700Vp-p. When compared to the as deposited device at the same applied voltage, which emits just 33 cd/m^2, this gives an improvement of over 1200%. The L-V curves have a moderate rise in luminance with increasing applied voltage which improves slightly with increasing fluence and number of pulses. The threshold voltage remained constant for all the laser annealed devices at 278Vp-p (± 10Vp-p).

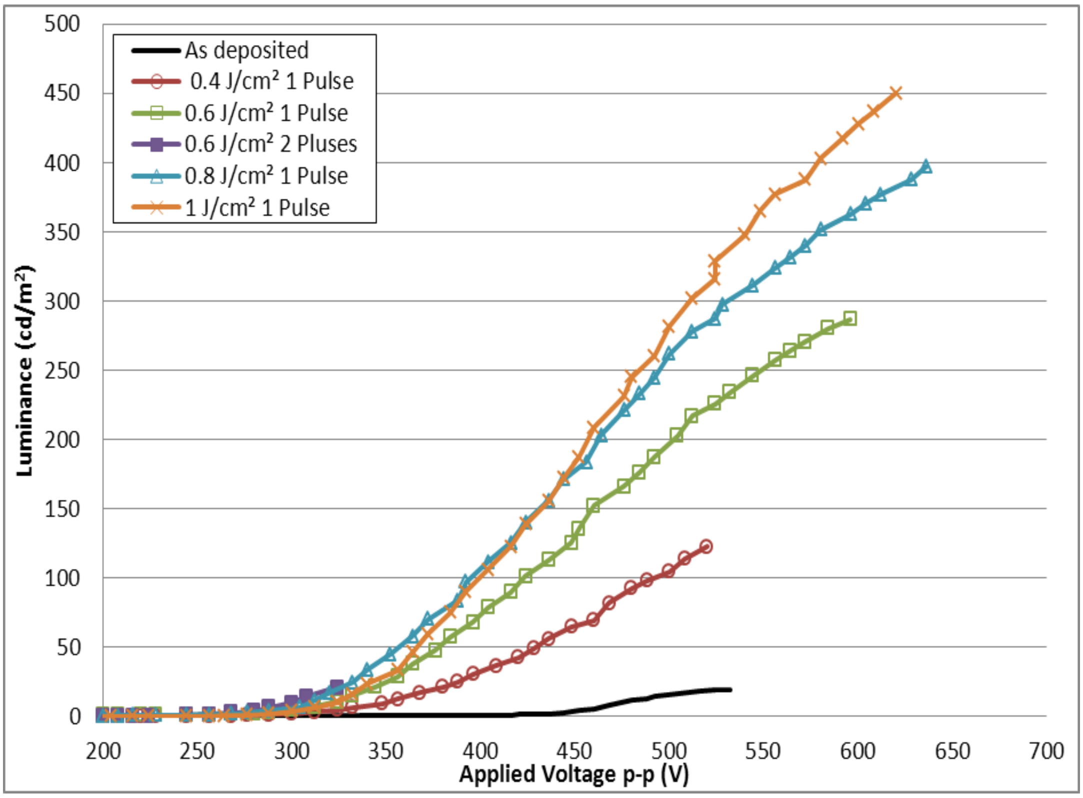

Figure 5.8 - Luminance as a function of applied voltage for ACTFEL devices laser annealed at various fluences deposited on plastic.

Figure 5.8 shows the L-V curves for the devices deposited on plastic. Again, the benefit of laser annealing on the luminescent properties is clear as there is an undisputable rise in luminance for all laser annealed devices when compared to the as deposited. The lowest fluence has a very shallow rise in luminance, this improves with increasing fluence but even at the highest fluence this is still only moderately sharp. The threshold voltage does decrease with increasing fluence, with the exception of the 1 J/cm^2 device. This is more than likely due to the device being from another sample that could possibly have a slightly thicker phosphor layer. The highest luminance observed at 500Vp-p was 281 cd/m^2 for the 1 J/cm^2 device, this is more than a 1500% increase from the as deposited 17 cd/m^2.

Figure 5.9 shows the performance of the devices for both substrates, the plastic devices are evidently superior even when processed at a lower fluence. The reason for the difference in performance is unclear, whilst this could be due to different depositions, the plastic sample containing the 1 J/cm^2 device was deposited alongside the glass sample, excluding the ITO layers. The difference could be due to the ITO layers, as was shown in section 4.4 the ITO depositions had been unreliable and a difference in the quality of depositions could account for the difference in luminance. The ITO may also adhere better to the plastic at the low temperatures deposition was taking place at; poor adhesion could lead to cracks and other defects such as bubbles reducing the quality and therefore the performance.

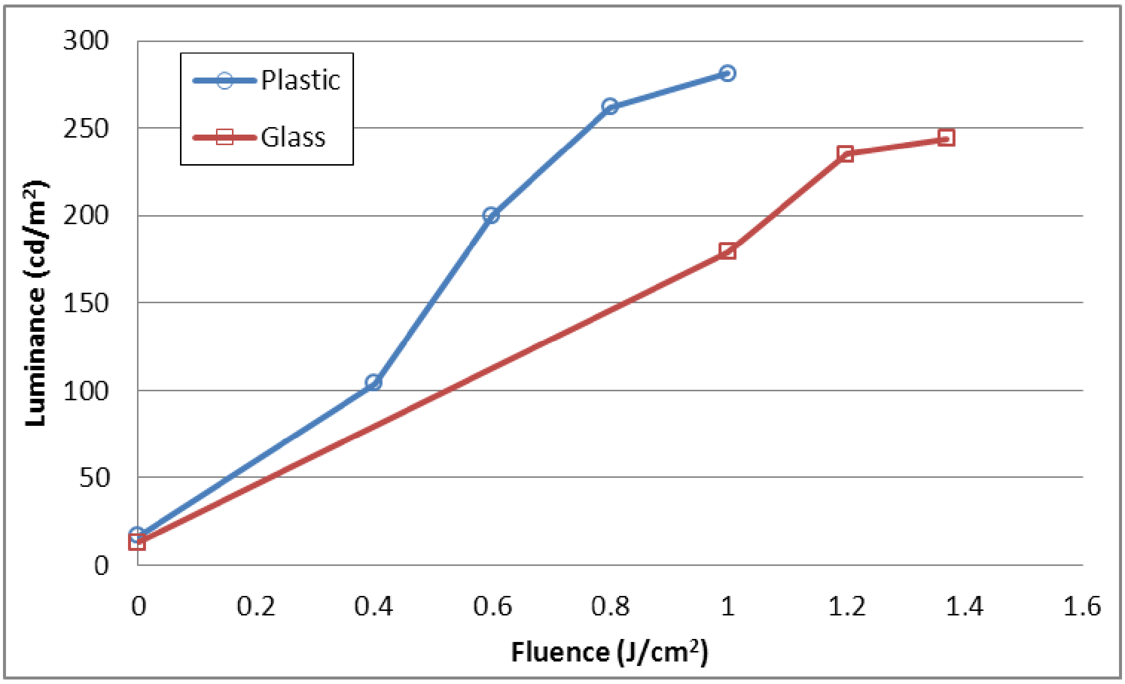

Figure 5.9 - Luminance as a function of fluence driven at a voltage of 500Vp-p for the HiTUS devices deposited on glass and plastic.

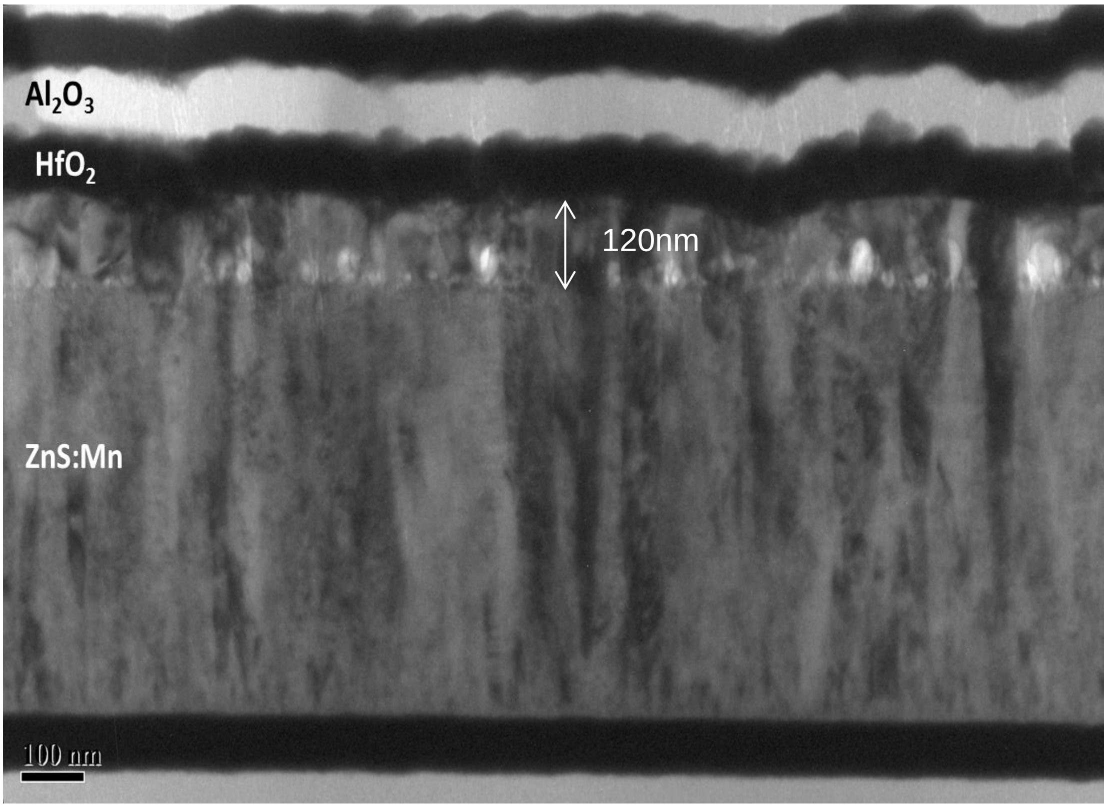

Figure 5.10 - TEM of laser annealed HiTUS device.

Figure 5.10 shows a TEM image of a device deposited on plastic and laser annealed at 0.4 J/cm^2. The upper region of the phosphor layer shows a modified region of ~120nm, this relates to the depth that the laser penetrates. Unlike with RF magnetron sputtered devices where the as deposited devices are of a cubic structure (103) and annealing promotes a phase change to a mixed phase of hexagonal and cubic (36) which is partially attributed as the reason for the increased luminescent performance. The HiTUS as deposited samples, like ALD, are already demonstrating the formation of the hexagonal phase as is shown in Figure 5.11 and Table 5.2. The rise in luminance that is seen between the as deposited samples and the laser annealed samples can be attributed in this case to a reduction in defects in the modified laser annealed section of the phosphor as shown in Figure 5.12.

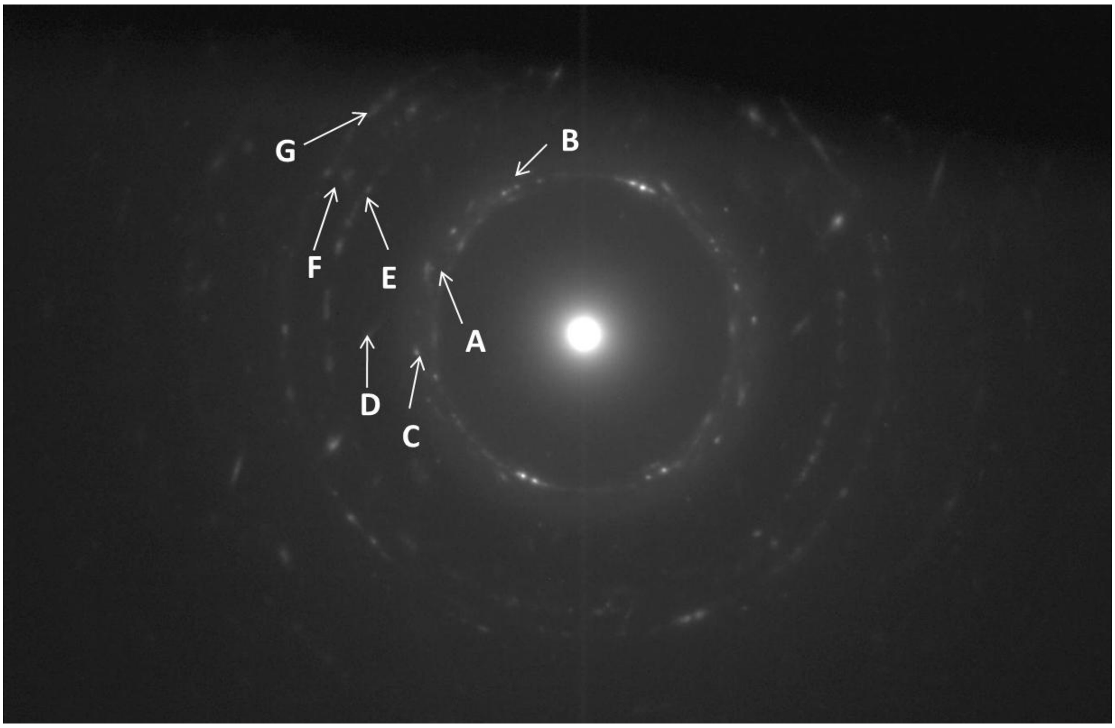

Figure 5.11 - TEM image showing the diffraction pattern of an as deposited device, the measured d-spacing of rings A – G are listed in Table 5.2

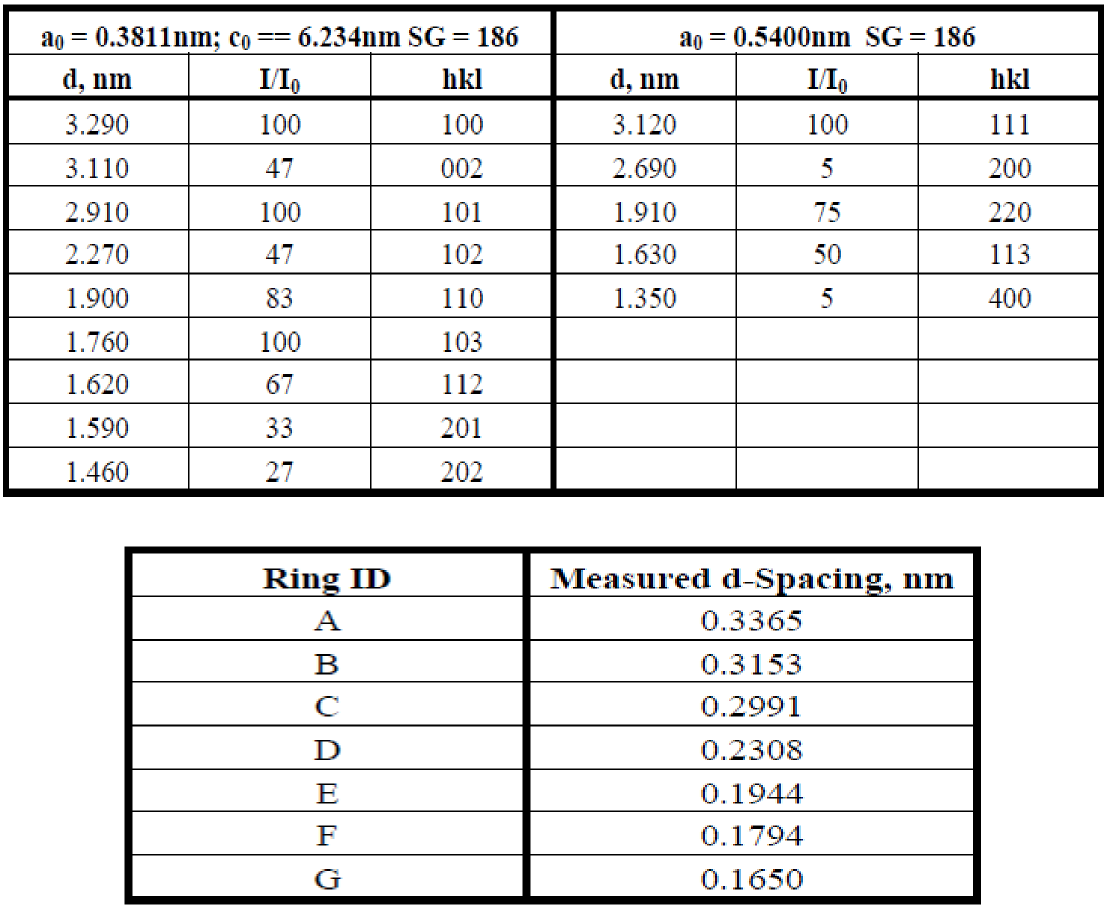

a_0 = 0.3811nm; c_0 == 6.234nm SG = 186			a_0 = 0.5400nm SG = 186		
d, nm	I/I_0	hkl	d, nm	I/I_0	hkl
3.290	100	100	3.120	100	111
3.110	47	002	2.690	5	200
2.910	100	101	1.910	75	220
2.270	47	102	1.630	50	113
1.900	83	110	1.350	5	400
1.760	100	103			
1.620	67	112			
1.590	33	201			
1.460	27	202			

Ring ID	Measured d-Spacing, nm
A	0.3365
B	0.3153
C	0.2991
D	0.2308
E	0.1944
F	0.1794
G	0.1650

Table 5.2 - Diffraction data for hexagonal (top left) and cubic (top right) phases of ZnS and the measured d-spacings for the as deposited device shown in Figure 5.11(bottom)

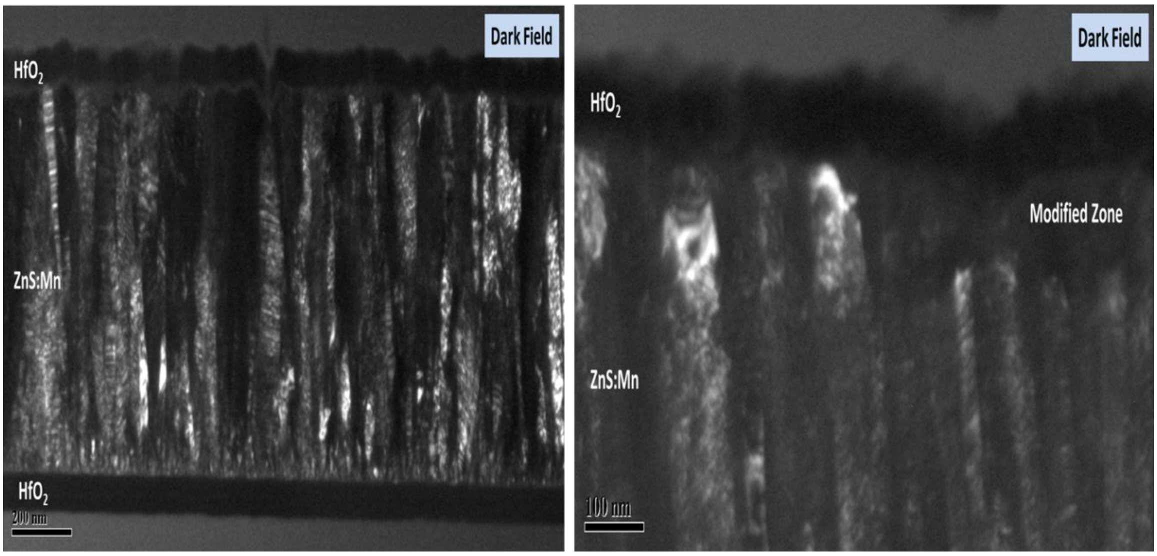

Figure 5.12 - Dark field images showing the reduction in defects from the as deposited state (left) in comparison to the laser annealed modified region (right)

5.4 Conclusion and Discussion

ACTFEL devices with a phosphor layer deposited by HiTUS and dielectrics deposited by RF magnetron sputtering have been subjected to varying number of pulses at various fluences. The results obtained in this chapter show that two pulse laser annealing at 248nm will generally yield the best results for device operation, however multiple irradiations at low fluences have achieved a higher maximum luminance. Further investigation is required in order to optimise these parameters to see if a high number of pulses at low fluences will yield devices with improved operating characteristics.

Entire ACTFEL devices have been fabricated using HiTUS on temperature sensitive substrates glass and plastic and laser annealed at various fluences at 248nm. These devices yielded very encouraging results demonstrating the feasibility of fabricating high intensity flexible displays when combining these two processes. The shallow turn-on of the devices could be improved by laser annealing at a wavelength of 193nm. The results obtained for the HiTUS devices highlights the importance of the materials used, and the dielectric layer in achieving efficient, bright devices. The hybrid device, although having one dielectric layer thermally annealed and being deposited at an elevated temperature is outperformed by the room temperature deposited nano-laminate devices in regards to maximum achievable luminance.

Laser annealing of ACTFEL devices is still very much a work in progress, but the benefits to the luminance are undisputable. Figure 5.10

shows a TEM image of a device deposited on plastic laser annealed at a fluence of 0.4 J/cm^2. The laser penetrates the phosphor layer to a depth of 120nm. The reduction in defect density and faults in just this top part of the phosphor can be attributed to the resulting 500% increase in luminance as no, if this defect reduction could be achieved throughout the entire phosphor layer a superiorly enhanced device could be realised.

6. Time Based Optimisation and Characterisation of LETFEL Devices

6.1 Introduction

The initial objective of work described in this chapter is to determine an optimum device structure of laterally emitting thin film electroluminescent (LETFEL) devices with regards to their aging characteristics and lifetime when the burn-in parameters are altered. The investigation will then continue to optimise this burn-in process. The LETFEL devices utilised were part of the sunlight readable electroluminescent device (SRELD) collaborative research project that aimed to address the necessity of sunlight readable vehicle displays in particular avionic indicators. This research did not form part of the SRELD collaboration as the project had finished prior to the onset of this body of work. The initial devices fabricated for the project demonstrated poor stability. After extensive testing of each individual layer (36), it was found to be the quality of the deposited dielectrics that was causing the issue. The initial devices were fabricated using RF magnetron sputtering at NTU and had a ZnS:Mn phosphor layer and SiON dielectric layers. The Micro and Nanotechnology Centre and Qudos Ltd at the Rutherford Appleton Laboratory (RAL) were responsible for the fabrication of the micro-mirrors and the subsequent etching. Some basic lifetime experiments were carried out on these devices for the purposes of comparison. The devices mainly utilised for this study were fabricated using ALD by Planar. The devices have a ZnS:Mn phosphor layer and Planars’

ATO dielectric which consists of Al_2O_3 and titanium oxide (TiO_2) with etching carried out at RAL. The basic steps of LETFEL fabrication and the finished tested device can be seen in Figure 6.1.

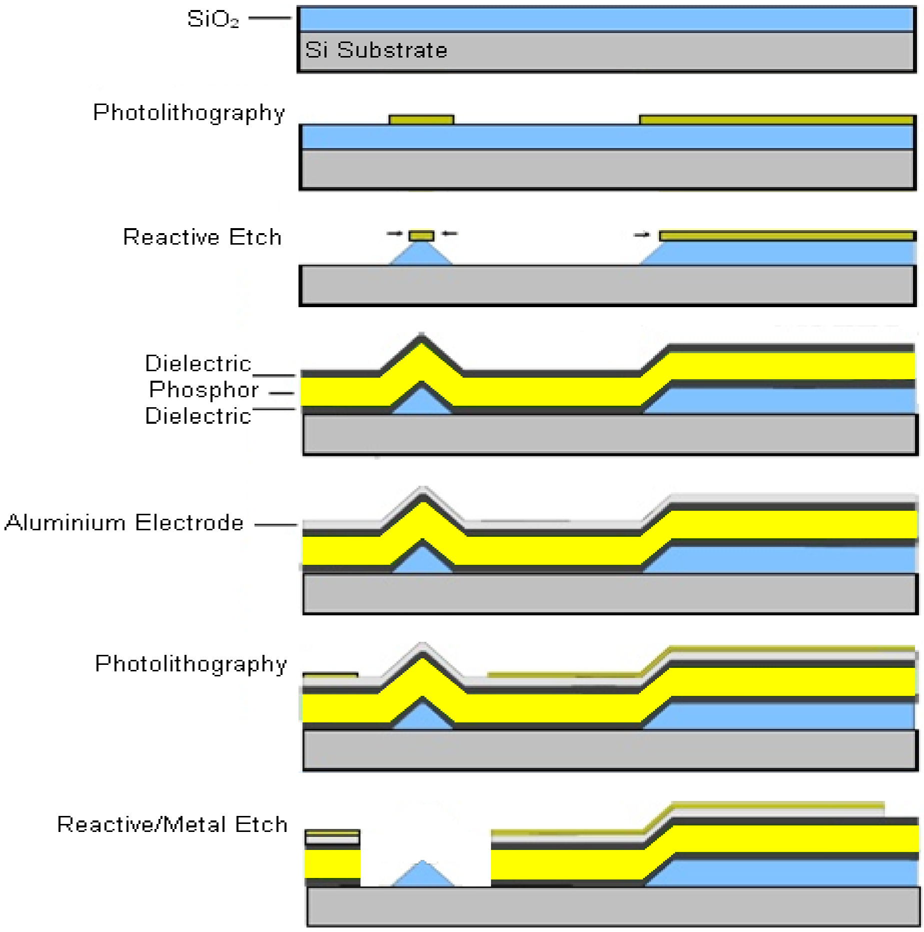

Basic steps in LETFEL fabrication (104)

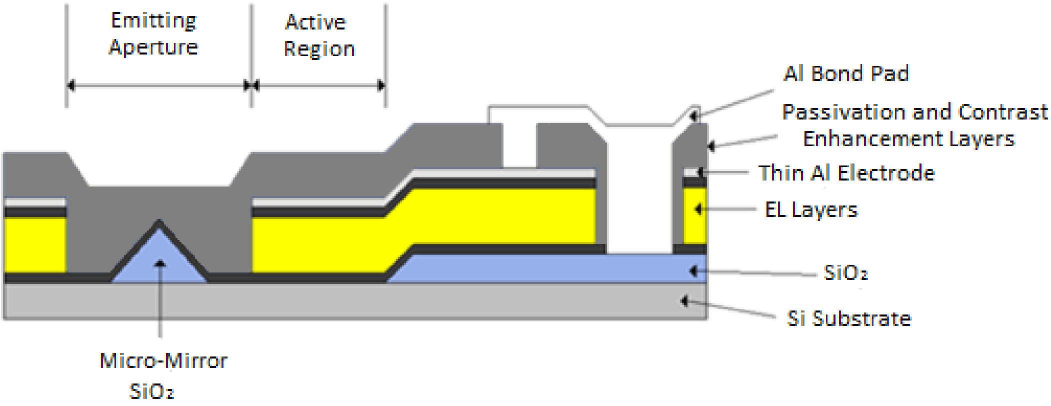

Figure 6.1 - LETFEL fabrication process and schematic of tested devices

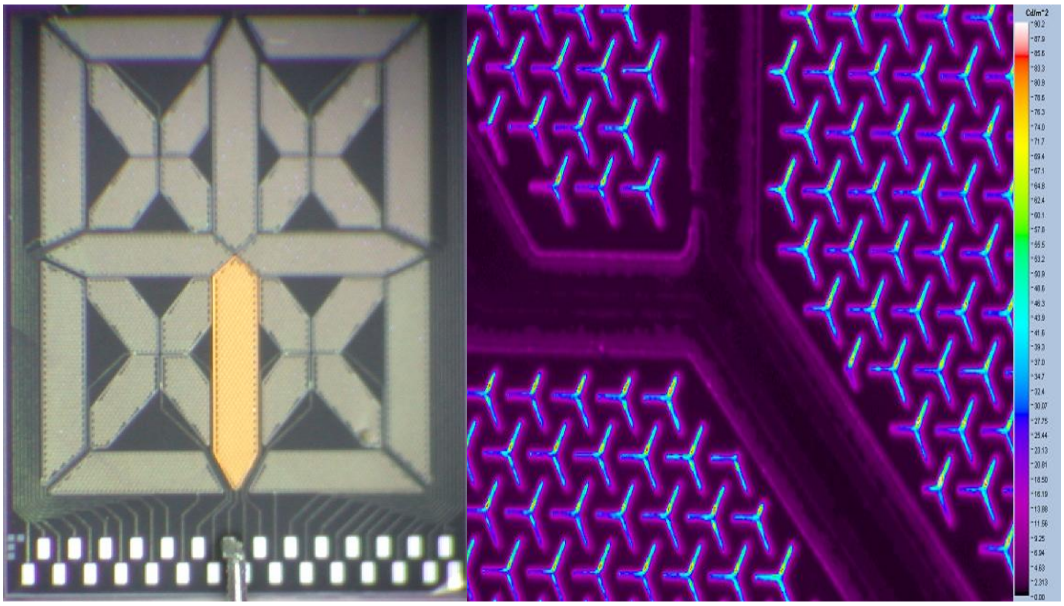

Figure 6.2 - (a) photograph of a SRELD device, (b) luminance mapping from an image photometer of a SRELD device.

The SRELD devices are comprised of 28 individually addressable light emitting pixels of various sizes, as illustrated in Figure 6.2(a). In order to ensure results are comparable, the pixels used have an area range of no greater than 0.0047mm^2. The pixels are made up of an array of micro-mirrors that are of a three pointed star design, this design was chosen as previous studies had shown that this structure yields the largest outcoupling efficiency, when compared to other designs (105). The SRELD devices exhibit good emission uniformity and high vision contrast as can be seen in Figure 6.2(b), the colour scale to the far right indicates the luminance output.

There are six different SRELD designs; the differences are associated with the micro-mirror structure and the various apertures and features on various layers. Table 6.1 details the key different design features of the six devices.

Design number	Micro- mirror width	Pull back	PSK edge stop	PSK aperture	Arm length	Pitch
D1	3.0	0.5	No	7.0	20	35
D2	3.0	1.0	No	7.0	20	35
D3	3.0	1.5	No	7.0	20	35
D4	3.0	2.0	No	7.0	20	35
D5	3.0	2.0	Yes	7.0	20	35
D6	3.0	1.5	No	7.0	40	60

Table 6.1 - LETFEL micro-mirror design dimensions (in µm)

The pullback refers to the distance of the top electrode from the edge of the active region. Devices based upon design five are the only ones to have the PSK edge stop, which consists of a micro-mirror structure around the edge of each pixel. The micro-mirror width, PSK aperture, arm length and pitch can be seen in Figure 6.3 that illustrates the micro-mirror design and dimensions.

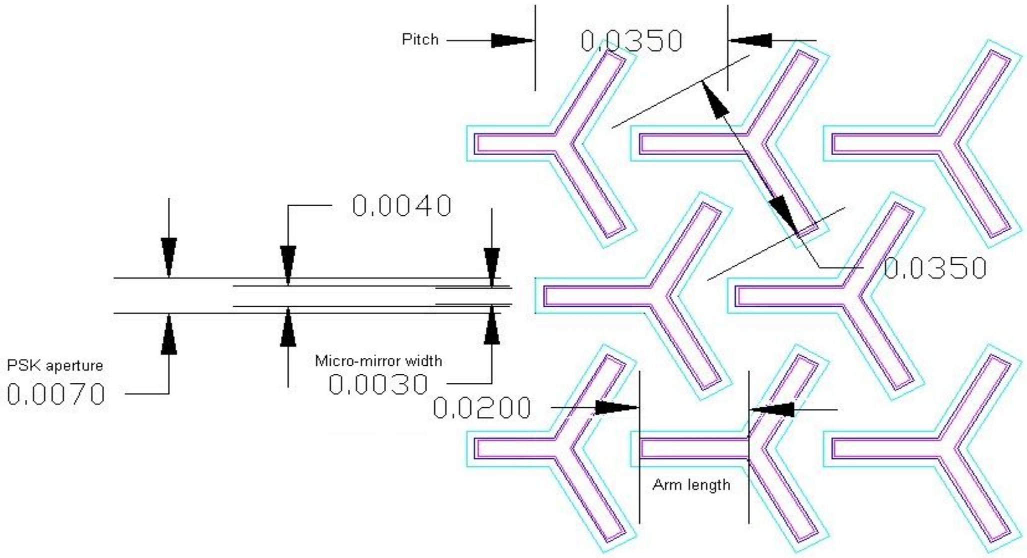

Figure 6.3 - LETFEL micro-mirror design dimensions (mm).

The exact mechanisms associated with the aging phenomena still remain partially unresolved, despite being studied since the early years of development for commercial quality devices (55). Aging of ACTFEL devices therefore remains one of the major problems to be solved in order to improve the quality of the displays (65). Previous studies have shown that the stability of the devices depends upon the structure and materials (67, 68, 106) the deposition method (69) and the driving method used (70, 107), it is the latter of these that is of interest in this study. The aim of this chapter is to investigate whether the initial burn in procedure applied to the devices has an effect on the lifetime. Whilst many previous studies have been carried out on the lifetime of ZnS:Mn ACTFEL devices, none of them have focused on the initial burn in stage (when a device is first turned on from a virgin state), and whether this crucial step effects how the device ages.

6.2 Experimental Details

The devices utilised for this chapter were fabricated on a 4inch n++ Si wafer. The active region is of the structure ATO/ZnS:Mn/ATO, with the thicknesses 300/800/300nm respectively. Note, there is no transparent electrode as no light is emitted through the surface. The ALD fabrication process was carried out at 500°C and no post deposition annealing was performed on the wafer. The precursors used for the phosphor layer were $ZnCl_2$ and H_2S for the ZnS and $MnCl_2$ for the manganese dopant.

The lifetime experiments were carried out on the purpose built probe station using the LabView program as described in Chapter 3. The program runs each device for 72 hours, recording an L-V curve every 6 hours, at the same time as recording the luminance data the voltage waveforms on both sides of the device are recorded for the purposes of electrical characterisation. For the lifetime curves the luminance is taken every 10 minutes using a printer linked to the Minolta luminance meter. The ambient light, ~ 200cd/m^2, is blocked out by a custom built tube situated between the probe card (just above the device) and the luminance meter. This reduces the ambient light measurement to 0.02cd/m^2, eliminating any effect on the lifetime measurements as these will be operating at approximately 40 – 100 cd/m^2.

The precise step time intervals and voltage increments for each investigation are detailed in the individual sections as they all differ slightly. For all experiments a 1.5kΩ series resistor was used for current protection and they were undertaken at room temperature in ambient conditions. They are aged at a voltage of 480Vp-p by a bipolar trapezoidal waveform unless otherwise stated.

Figure 6.4 illustrates where the devices are taken from on the wafer. Where possible they are taken from similar positions on the wafer in order to aid with comparison. Devices for designs one, three and five were initially tested from positions around the edge of the wafer but they suffered from poor luminance and were found to be very susceptible to failure. As a result devices from a more central position were used.

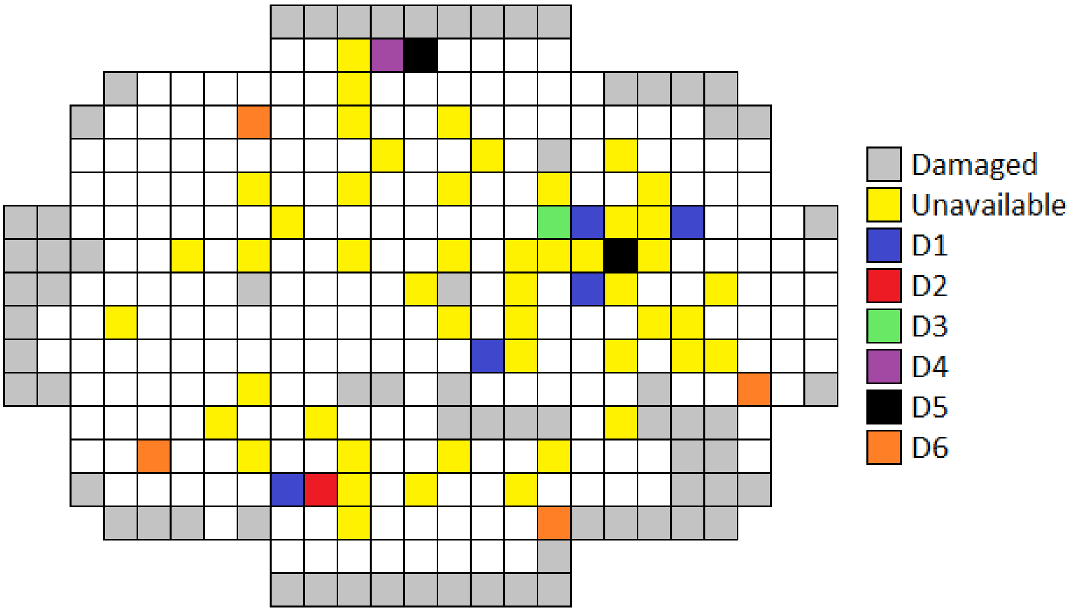

Figure 6.4 - Layout of the SRELD wafer showing locations of tested devices.

6.3 Results

6.3.1 Burn-in Time Optimisation

The following section details the lifetime and aging experiments carried out in order to determine the optimum micro-mirror design and to also conclude if the time taken in between voltage increments during the burn-in process has an effect on the lifetime and aging of the device. The devices were aged using a 1 kHz bipolar trapezoidal waveform with a 4 Vp-p increase every 3, 5, 10 or 20 seconds.

6.3.1.1 3 Seconds

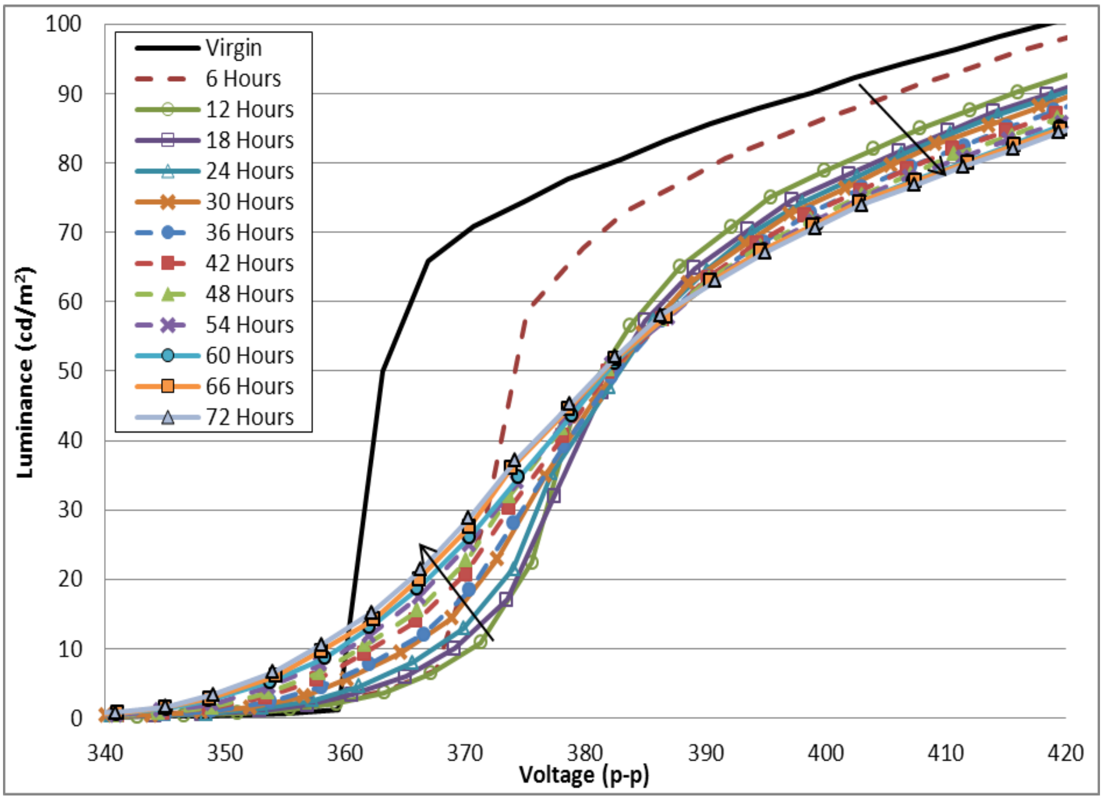

Figure 6.5 - Design one L-V curves

Figure 6.5 shows the L-V curves of a design one device. An L-V curve measurement was taken every 6 hours over the 72 hour lifetime. The results are typical for all six designs so only a single design is being shown to demonstrate the aging behaviour. The virgin L-V curve has an initial very sharp rise in luminance as a function of applied voltage over a 10Vp-p range before continuing to increase at a much slower rate. The L-V curve, after 6 hours of being stressed at 480Vp-p, primarily has quite a shallow turn on before increasing sharply over a 10Vp-p range, after which the rise becomes much shallower as with the virgin L-V. From 12 hours on wards the L-V curves become increasingly shallower and the luminance at 480Vp-p slowly decreases with each measurement. The key data contained within the graph is how the curves are softening and shifting over time which is indicated by the arrows that show the direction of movement. The biggest difference in the curves can be seen between the virgin and the aged for 6 hours L-Vs. Although there has been a negative 10Vp-p shift in the threshold voltage, shown in Figure 6.7, there is approximately a 10Vp-p shift in the positive direction in regards to the 6 hour curves voltage for a given luminance in comparison to the virgin curve. This occurs in the section where both curves are showing a sharp increase in luminance as a function of voltage. This shift is a result of the shallow initial turn on that all the curves exhibit form 6 hours onwards. There is also a large change in the shape of the 6 hour and 12 hour curves, the initial rise in luminance has become slightly shallower and the curve has softened giving it an almost S shape. Form 12 hours onwards this S shape begins to soften more and more as the gradient of the turn on curve slowly decreases as does the luminance.

The virgin and final L-V curves for all six designs are shown in Figure 6.6. Note that when the device did not last the 72 hours, the last recorded L-V curve has been used and any data that falls below the x-axis is generally noise. The virgin curves, with the exception of design two, all have a very sharp rise in luminance as a function of applied voltage and a similar softening and negative shifting. Although the L-V curves for both design two and three exhibit softening the threshold voltage shift is marginal, the likely cause for this is due to the pixels failing there is a smaller emitting area and therefore lower luminance levels.

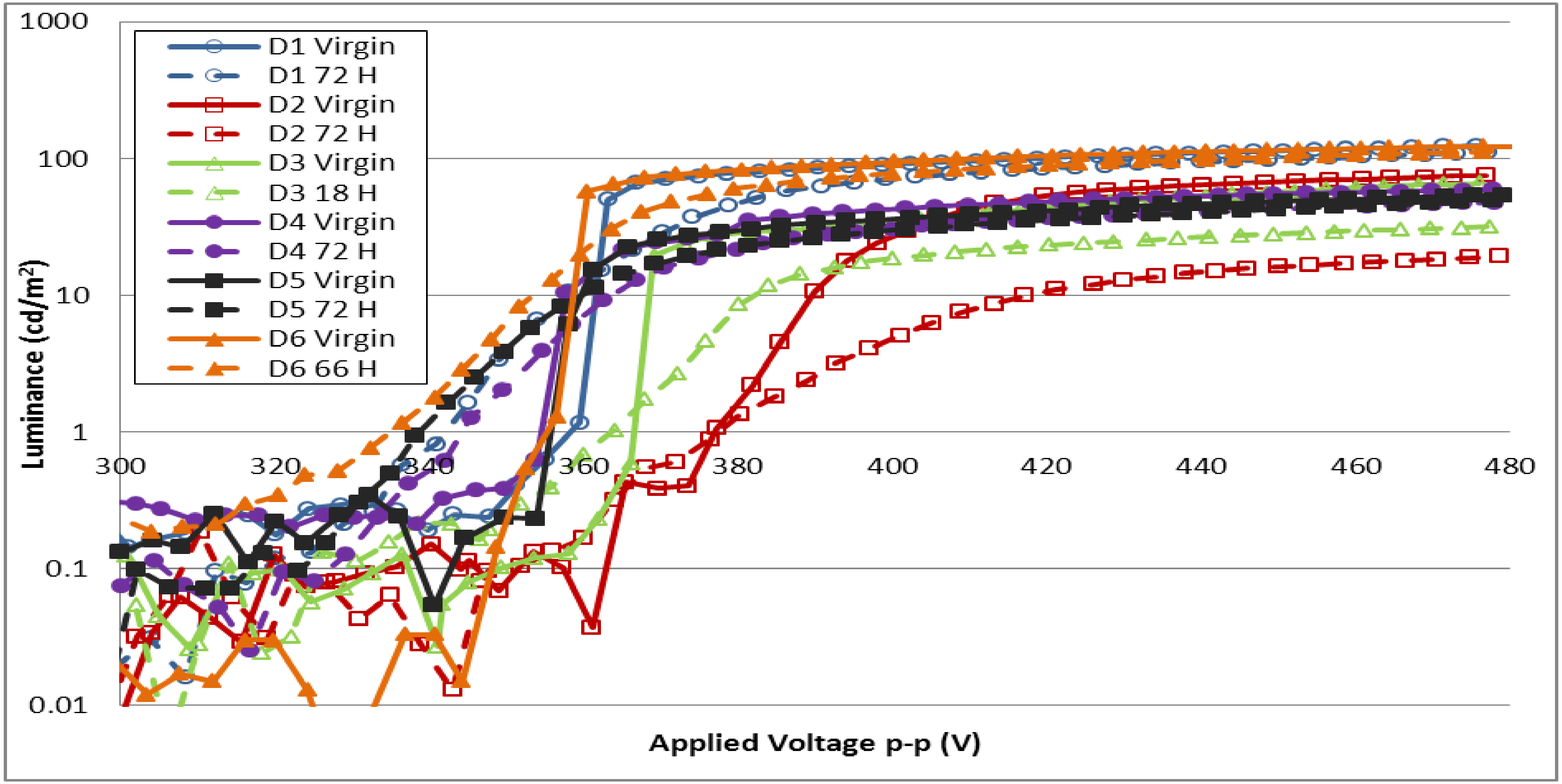

Figure 6.6 - Virgin and final L-V curves for all designs (3 seconds)

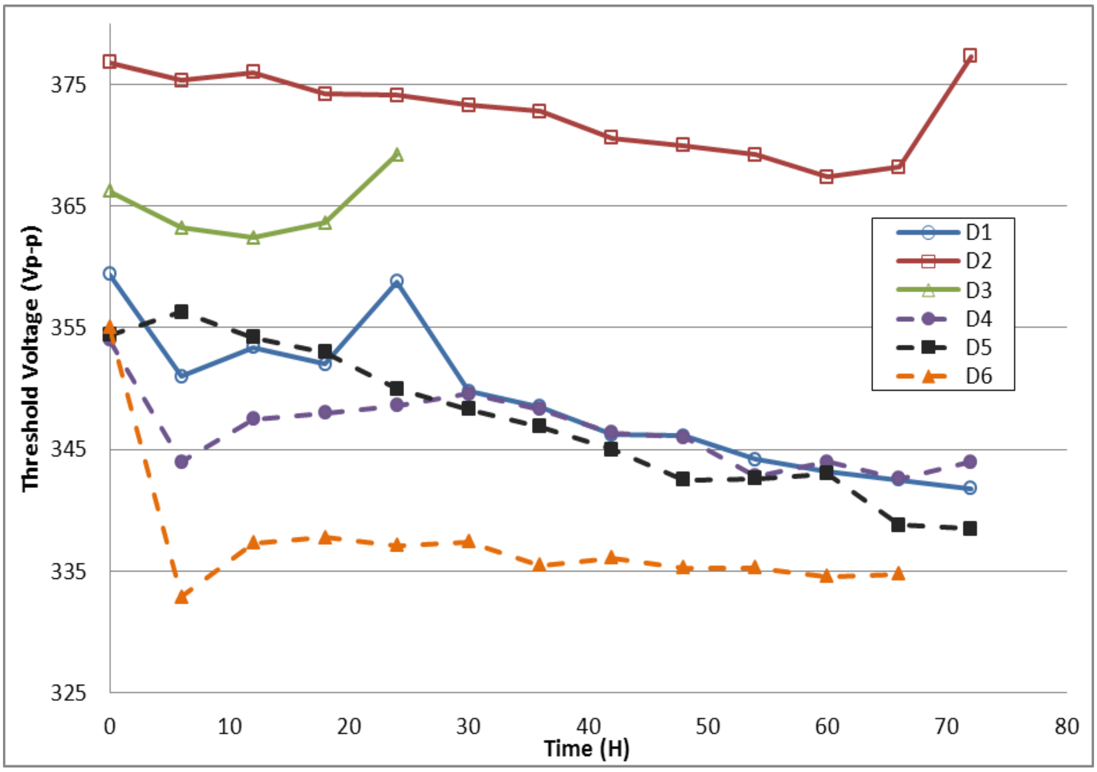

Figure 6.7 - Threshold voltage as a function of time for all designs (3 seconds)

The threshold voltage, defined as the voltage at which the luminance is 1 cd/m^2, is shown in Figure 6.7 for all six designs over the 72 hour lifetime. For designs two and three, the increase in threshold voltage at the end is due to both designs failing as previously discussed. For designs one, four and five, the threshold voltage in general gradually decreases and begins to slowly level out towards the end of the 72 hours. For design six, after a considerably large initial decrease, the difference between each interval reduces and the threshold voltage becomes very consistent from 36 hours onwards, although it does have the largest change in threshold voltage at ~20Vp-p. Designs one, four and five have a change of ~ 15Vp-p.

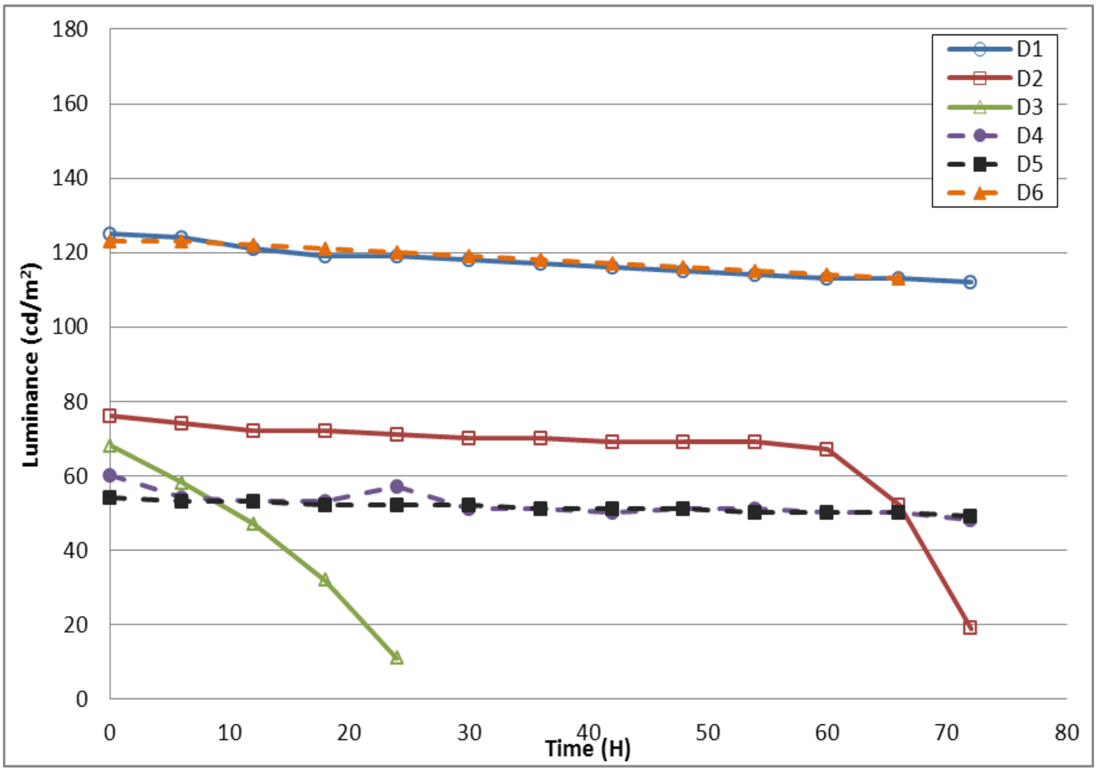

Figure 6.8 - Luminance as a function of time at an applied voltage of 480Vp-p for all designs (3 seconds).

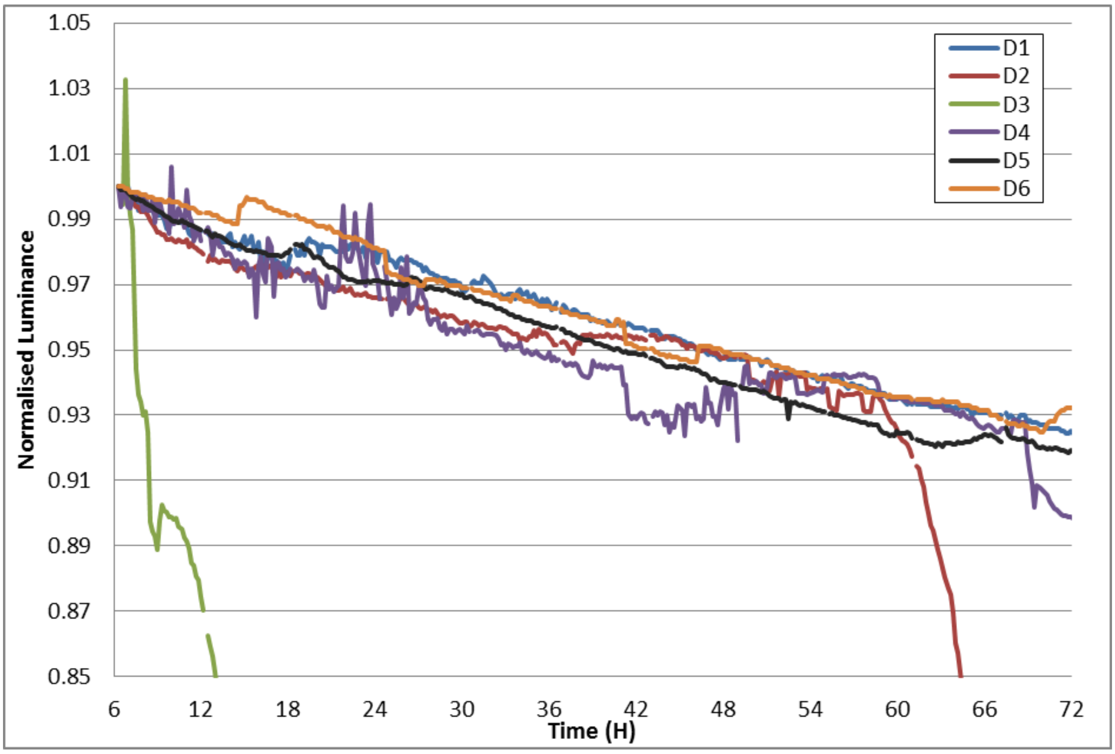

Figure 6.9 - Normalised luminance for all designs over 72 hour lifetime (3 seconds).

The luminance of all the six designs as a function of time is shown in Figure 6.8. The failure of designs two and three, which was not clearly evident in previous figures, can be seen, design six also fails before the end of the lifetime. Design three rapidly deteriorates from the start whereas designs two and six are relatively stable before failing, in the case of design six, the entire pixel fails instantly, whereas with designs two and three a small area on the pixel failed and slowly propagated across a larger area.

Figure 6.9 shows the normalised luminance of the six designs. The data is normalised to the first point after the second L-V curve measurement had been taken. This is to allow for a forming period as the device settles down. In the first 6 hours devices demonstrated one of three behaviours:

- A sharp decrease in luminance, which can be seen for some devices in the luminance as a function of time trends.
- A slow rise in luminance, usually of ~ 5 cd/m^2, which would then slowly decrease back to the original luminance before the next L-V was measured.
- Finally, the least common of the behaviours was for the pixel to exhibit minimal or no change in luminance.

The devices appear to age at very similar rates overall with designs one and six aging marginally slower. The aging is ‘fairly’ linear in that most points fall within an acceptable distance from a given line, with the exception of design four were the luminance never appears to be very stable. The spikes in luminance that can be observed in the lifetimes has been attributed to neighbouring pixels turning on and off over the three day period. This behaviour was observed for some pixels during the initial turn on and appeared to be more prominent for certain designs.

6.3.1.2 5 Seconds

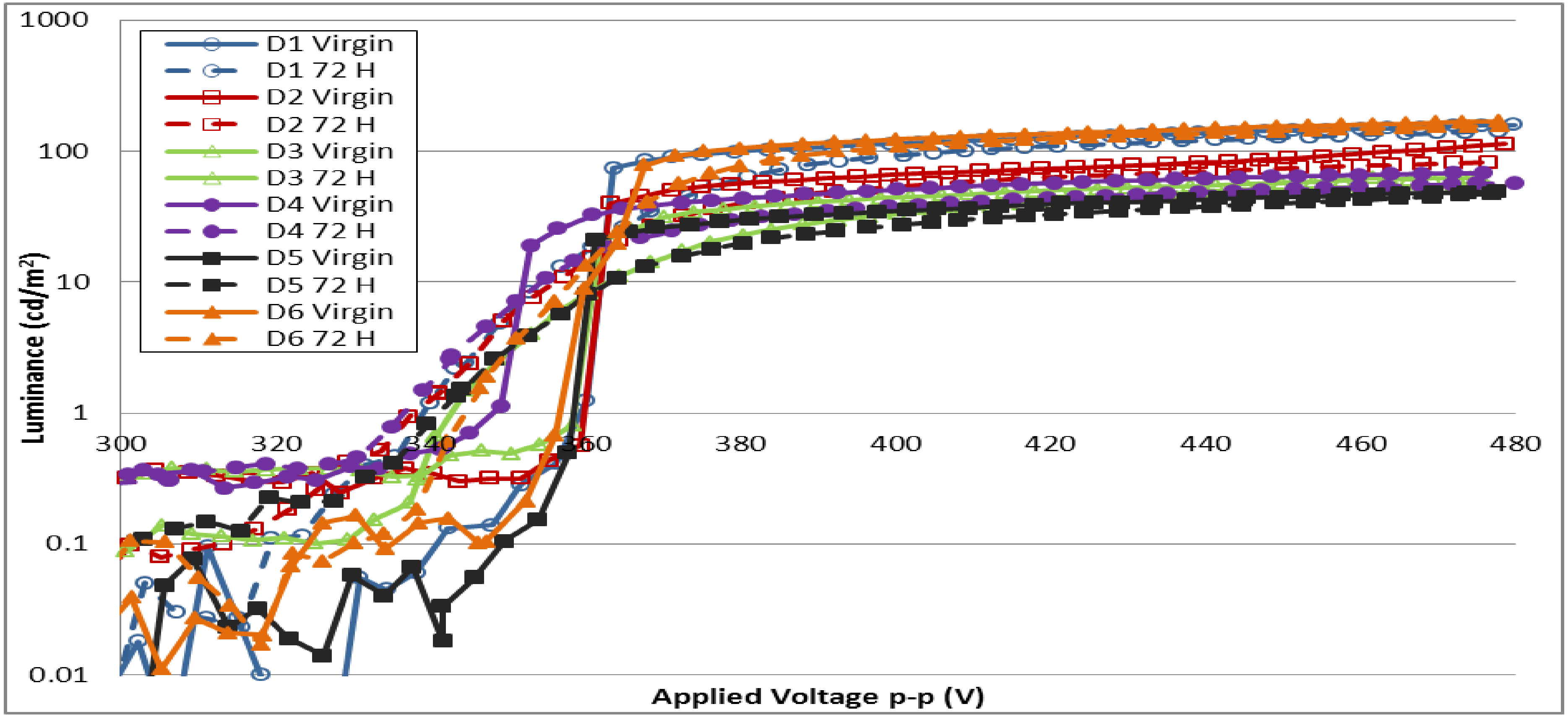

Figure 6.10 - Virgin and final L-V curves for all designs (5 seconds)

The curves for the virgin and final L-V measurements for the 5 second step interval can be seen in Figure 6.10, again data that falls below the x-axis is considered noise. The virgin L-V curves are very sharp for all six designs, and, with the exception of design four, have a very similar threshold voltage. There should be no reason for a different virgin threshold for design four, as the threshold voltage at this point is determined by the phosphor thickness. There is a similar amount of negative threshold shift after being aged for 72 hours, as with the 3 second step interval. The only exception is design six, where the shift has halved resulting in less softening of the final L-V curve.

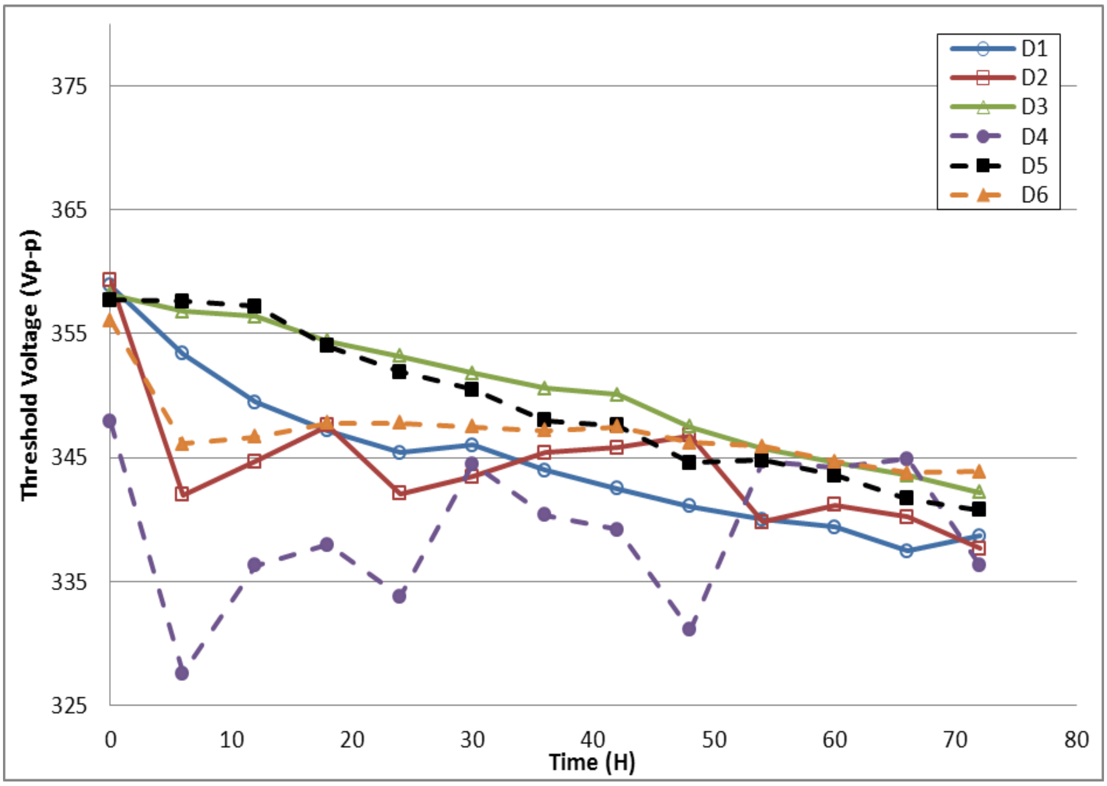

Figure 6.11 - Threshold voltages as a function of aging time of all six designs (5 seconds)

Figure 6.11 illustrates the change in threshold voltage of each of the designs over the 72 hour aging period when using a 5 second step interval during turn-on. There is a maximum 20Vp-p shift for all of the designs, even design four, which appears very erratic; after an initial large negative shift the threshold voltage shifts in both a positive and negative direction but at no point does it exceed the virgin threshold voltage. The remaining five designs all start and finish at similar voltages. With designs one, three and five, the decrease is steady over the 72 hour period, design one has an initial large decrease before jumping between positive and negative shifts, whilst slowly decreasing towards 335Vp-p. Design six has the smallest threshold voltage range at just ~12Vp-p, most of which occurs between the virgin and 6 hour time.

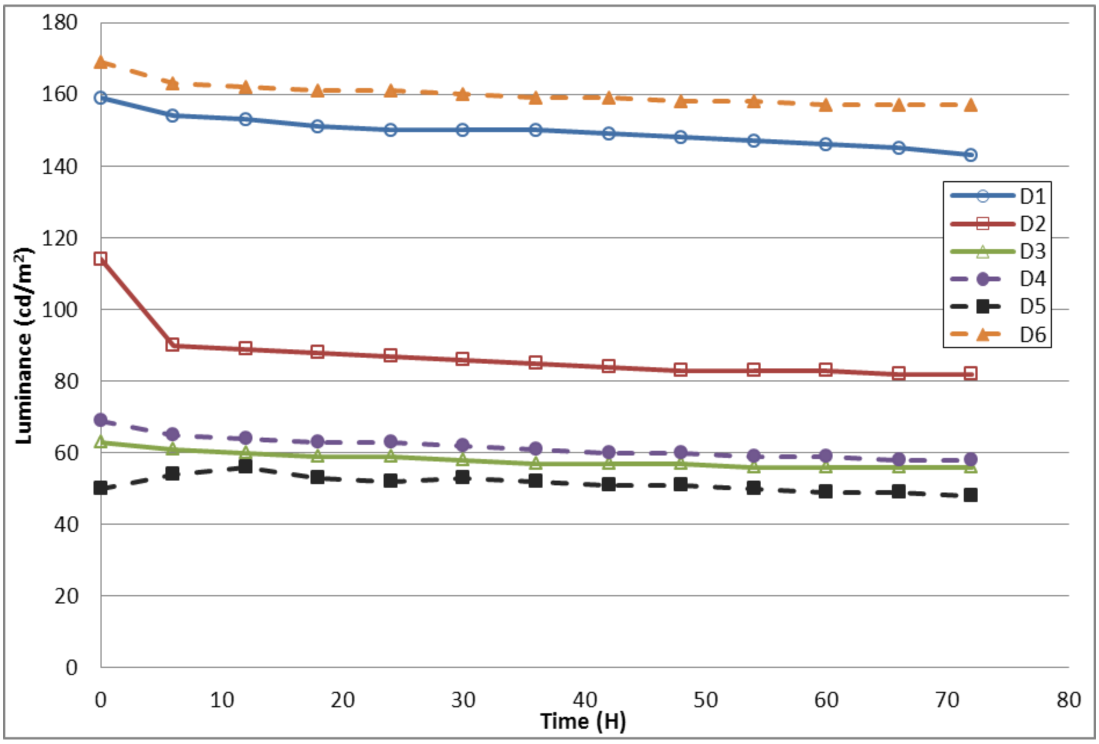

Figure 6.12 - Luminance as a function of time at an applied voltage of 480Vp-p for all designs (5 seconds)

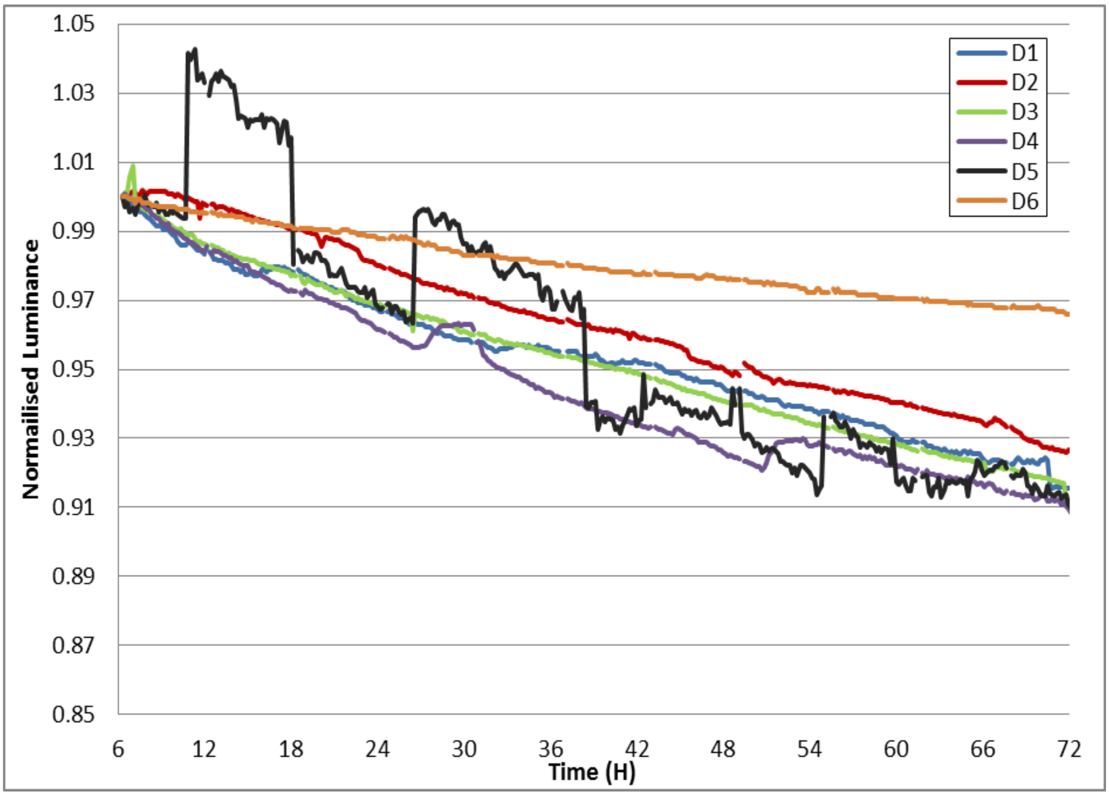

Figure 6.13 - Normalised luminance over 72 hours for all designs (5 seconds)

The luminance for the different designs over the 72 hour aging period can be seen in Figure 6.12. Design two has a large decrease in luminance over the first 6 hours, falling from 114 to 90 cd/m^2, a more than 20% decrease. For the remaining 66 hours the luminance only reduces by a further 7% from the original value. This behaviour was the reasoning behind the 6 hour forming period, so a more accurate aging rate could be determined. Design five demonstrates the opposite behaviour, as a slight increase in luminance can be observed over the first 12 hours, whilst several pixels demonstrated a similar trend, only this one was still showed any sign of an increase after 6 hours. Due to this increase, the final luminance was only 2 cd/m^2 lower than the start value, giving the smallest percentage decrease of all the experiments at just 4%. However, the L-V curves shown in Figure 6.10 did not exhibit any less softening and shifting when compared to the other designs with larger luminance decreases. The remaining four designs all have a noticeable decrease in luminance over the first 6 hours, after which the decline is very soft over the remaining 66 hours.

Figure 6.13 shows the normalised luminance data for the 5 second step interval. Unlike the 3 second lifetimes, there is a clear difference between some of the designs. Design six is clearly aging at a much slower rate to the other five designs. Design two is declining at a slightly slower rate to the other four, which are barely separable.

6.3.1.3 10 Seconds.

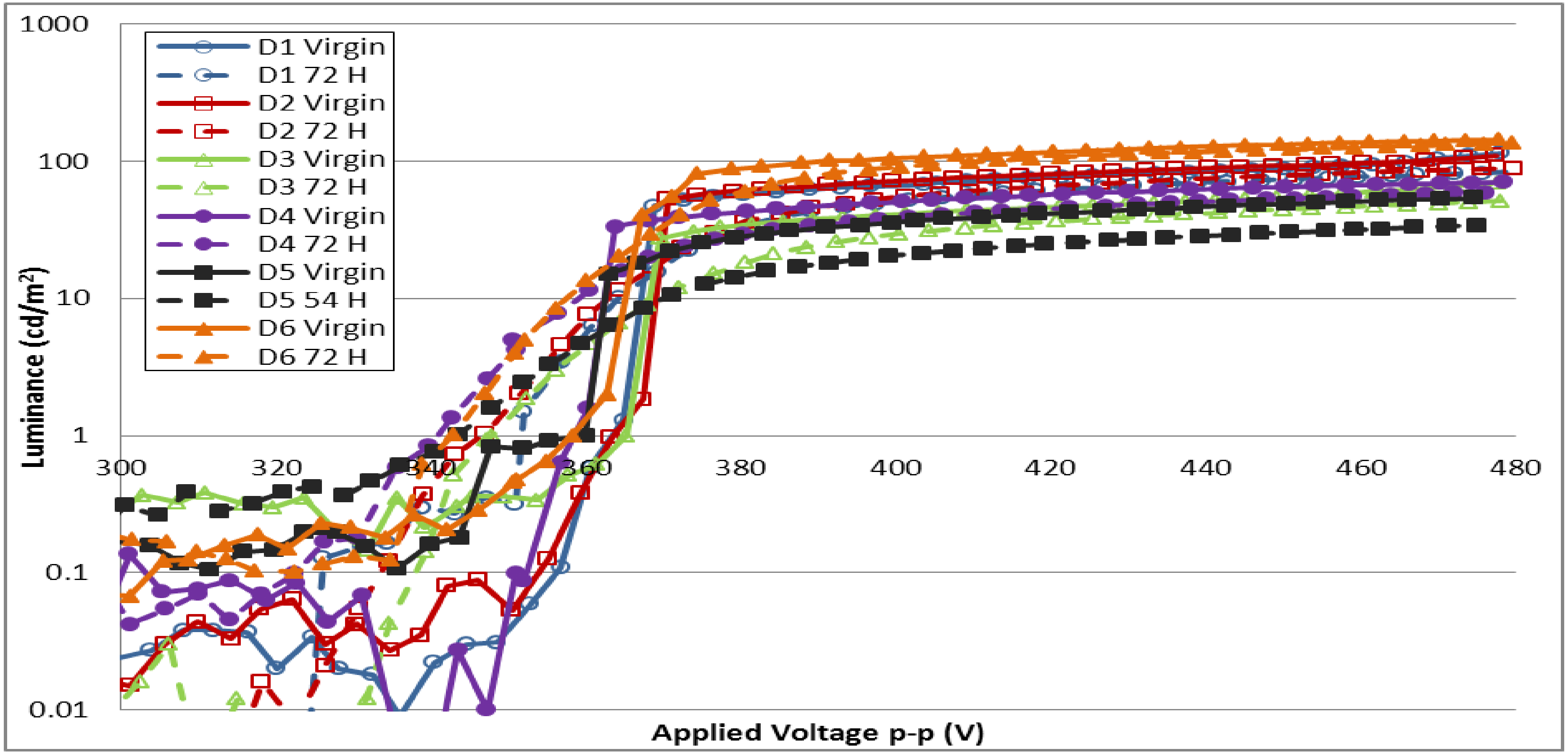

Figure 6.14 - Virgin and final L-V curves for all designs (10 seconds)

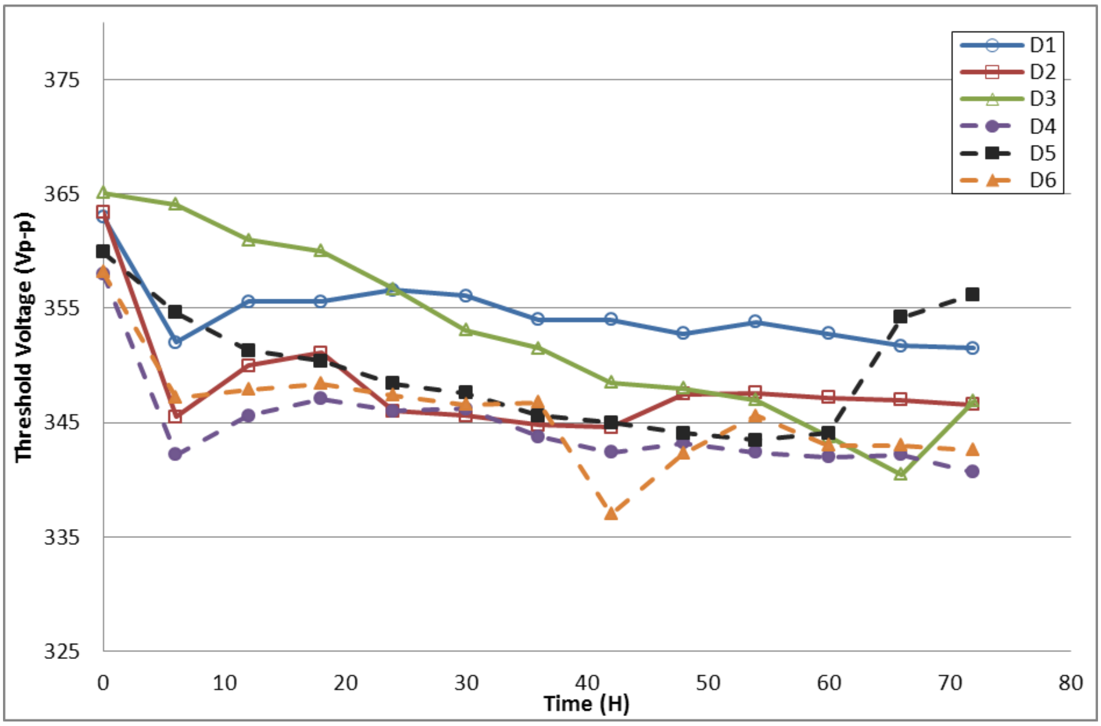

Figure 6.15 - Threshold voltage as a function of time for all designs (10 seconds)

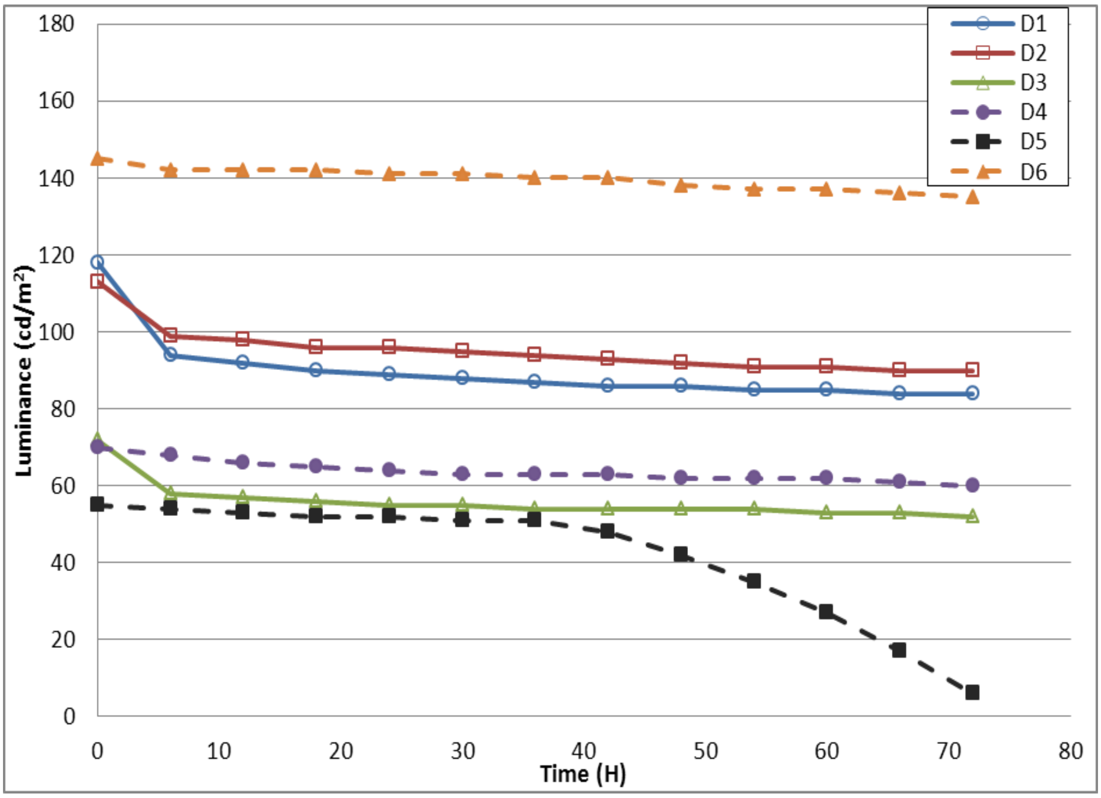

Figure 6.16 - Luminance as a function of time at an applied voltage of 480Vp-p for all designs (10 seconds).

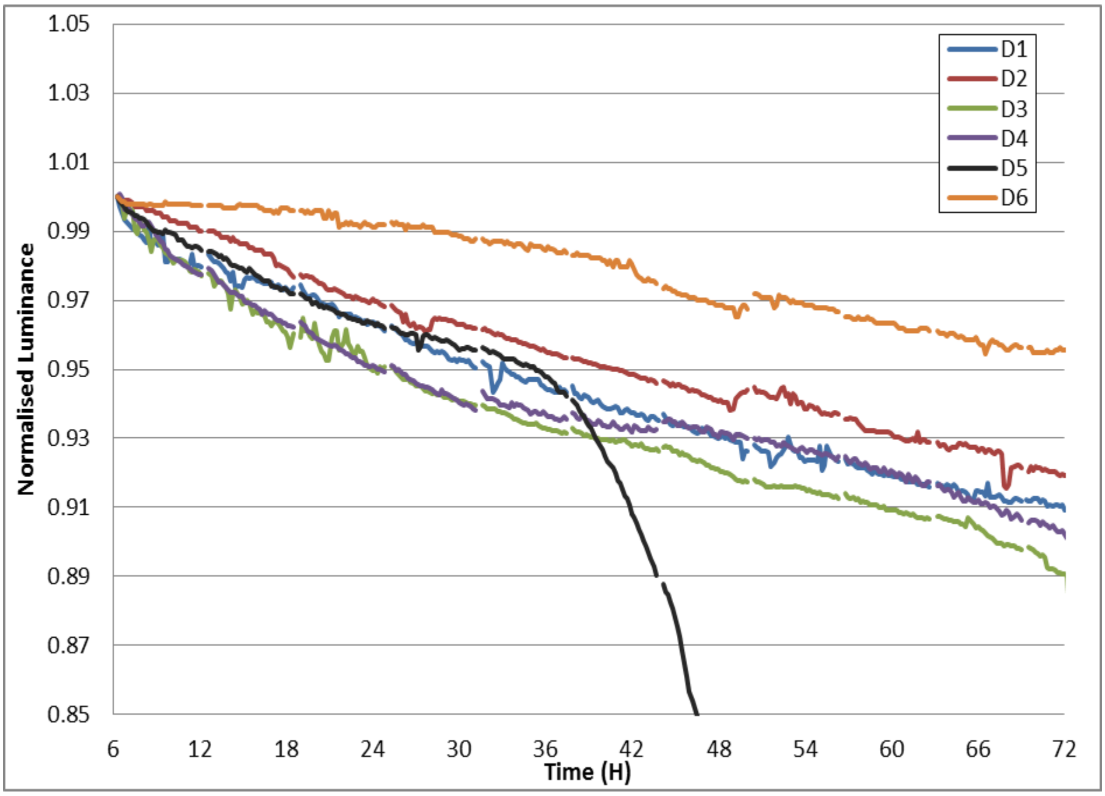

Figure 6.17 - Normalised luminance over 72 hours for all designs (10 seconds)

Figure 6.14 shows the virgin and aged L-V curves for the 10 second step interval. The grouping of the two sets of curves is the same as the previous two sets of experiments. The initial turn on for the virgin curves however have started to soften slightly around the threshold level and a small curve can be observed in this area for designs two and six.

Figure 6.15 details the threshold voltages over the lifetime. As expected, the virgin values are grouped closely together. The threshold voltages for designs three and five slowly reduce over time; the increase in design five can be attributed to the pixel failure. The other four designs all have an initial large drop in threshold voltage, after which there are marginal changes in both positive and negative directions.

Luminance as a function of time is shown in Figure 6.16. Designs one, two and three all exhibit large drops in luminance over the first 6 hours of 20%, 12% and 19% respectively. For the remaining 66 hours they only reduce by a further 11% at worse.

The normalised luminance is depicted in Figure 6.17; there is now a clear difference in the rate of deterioration between all the six designs. Design six reduces at the slowest rate, there is then a considerable gap to the next design which is design two. Designs one, four and three respectively are then approximately equal distance below the other.

6.3.1.4 20 Seconds

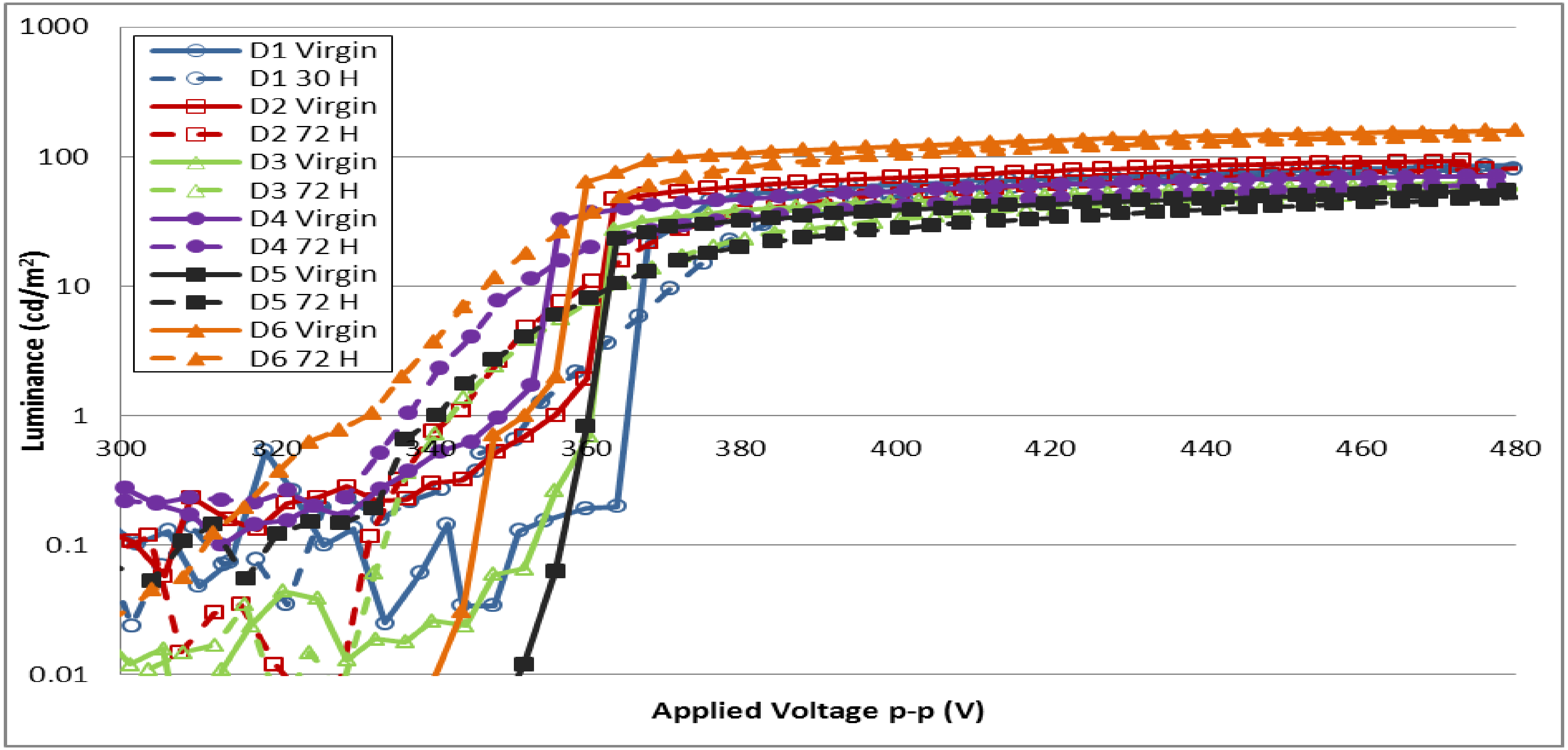

Figure 6.18 - Virgin and final L-V curves for all designs (20 seconds)

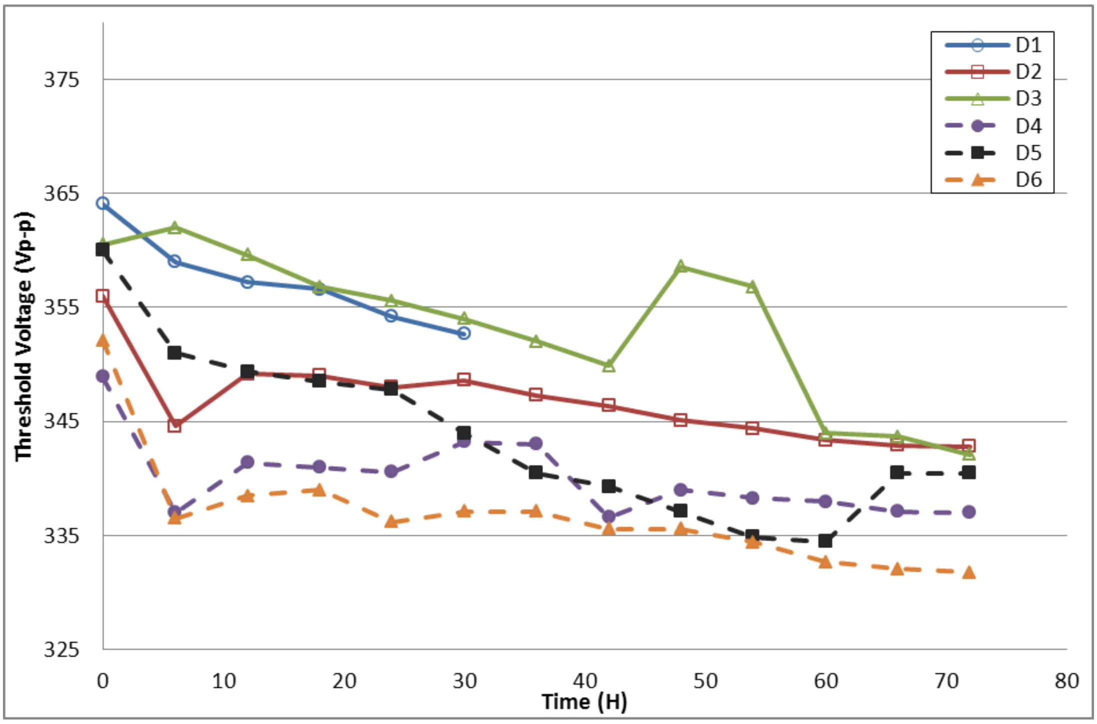

Figure 6.19 - Threshold voltage as a function of time for all designs (20 seconds)

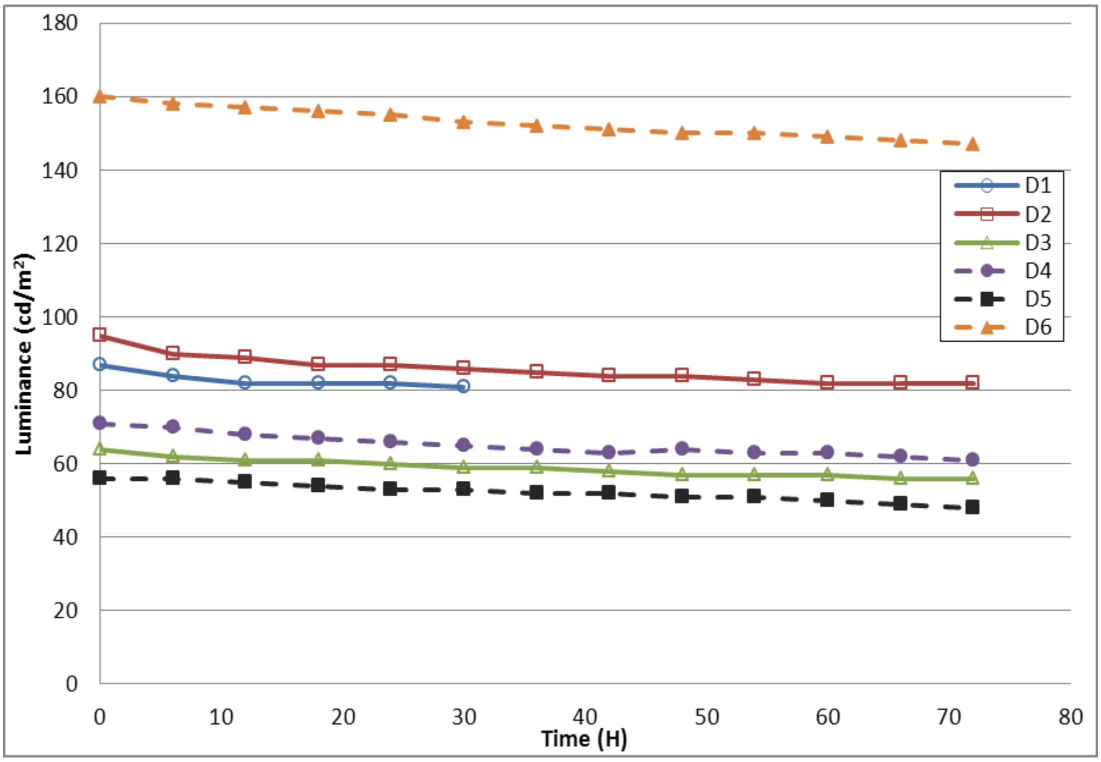

Figure 6.20 - Luminance as a function of time at an applied voltage of 480Vp-p for all designs (20 seconds).

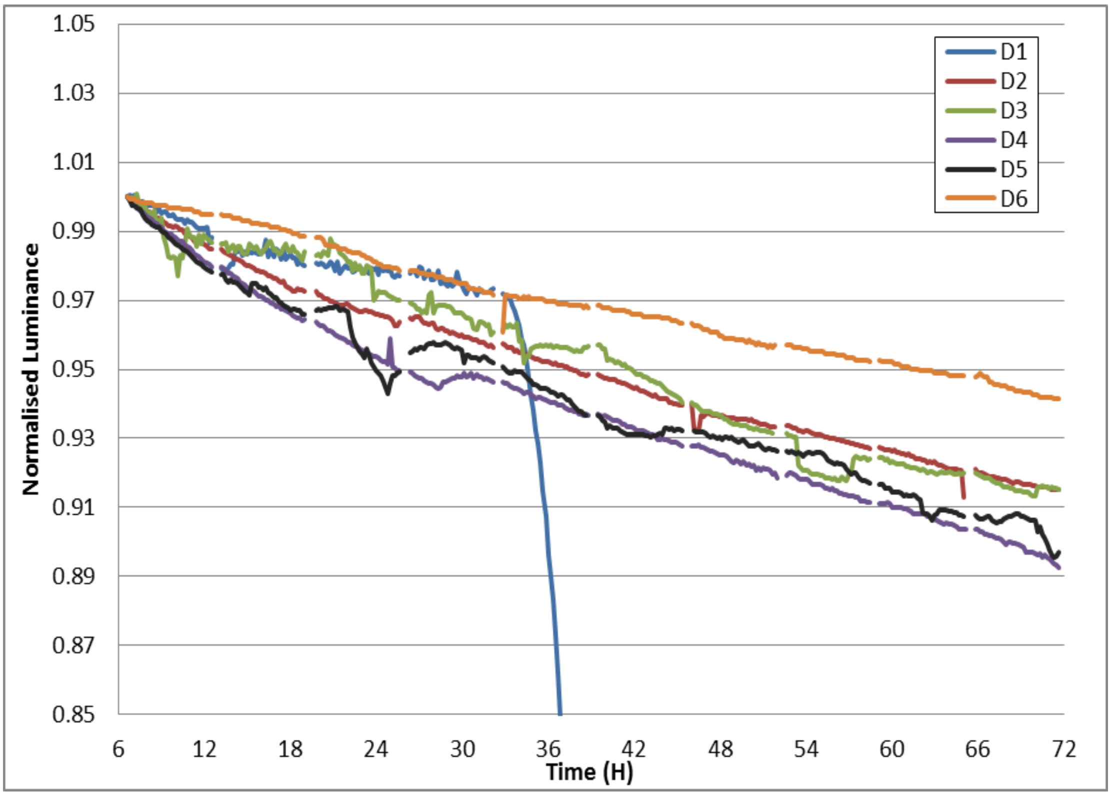

Figure 6.21 - Normalised luminance over 72 hours for all designs (20 seconds)

The L-V curves for the 20 second step interval are shown in Figure 6.18. Unlike the previous three data sets the curves are quite spread out. Similarly to the 10 second step interval, with the virgin curves there is a softening around the threshold voltage region exhibited by designs two, four and six which has become slightly more prominent. Due to the longer burn-in time between each voltage increase with the 20 second interval, this softening could be caused by the creation of space charge in the phosphor field that may not be present in the shorter burn-in times.

Figure 6.19 shows how the threshold voltage shifts over time. Designs two, four and six all exhibit a large negative threshold shift between the virgin and 6 hours, despite already having a somewhat lowered voltage due to the softening. This large negative shift however, is then followed by a shift in a positive direction before slowly reducing over time.

Figure 6.20 illustrates the luminance over the 72 hour period. All six designs are stable over the entire duration with a decrease in the first 6 hours similar to those between the remaining 6 hour periods.

The normalised lifetimes are shown in Figure 6.21. Again, design six demonstrates the slowest decrease in luminance over time with design one probably decreasing at a similar rate, had it not failed. There is then a large gap to the next two designs, two and three, that have decreased at a similar rate. An equally large gap exists to the final two designs in which luminance has again decreased at a similar rate.

6.3.1.5 Design six Comparison

The results indicate that design six has the best performance in comparison to the other five designs, the reason for which is discussed in section 6.4. The following sub-section directly compares design six over the four different step intervals.

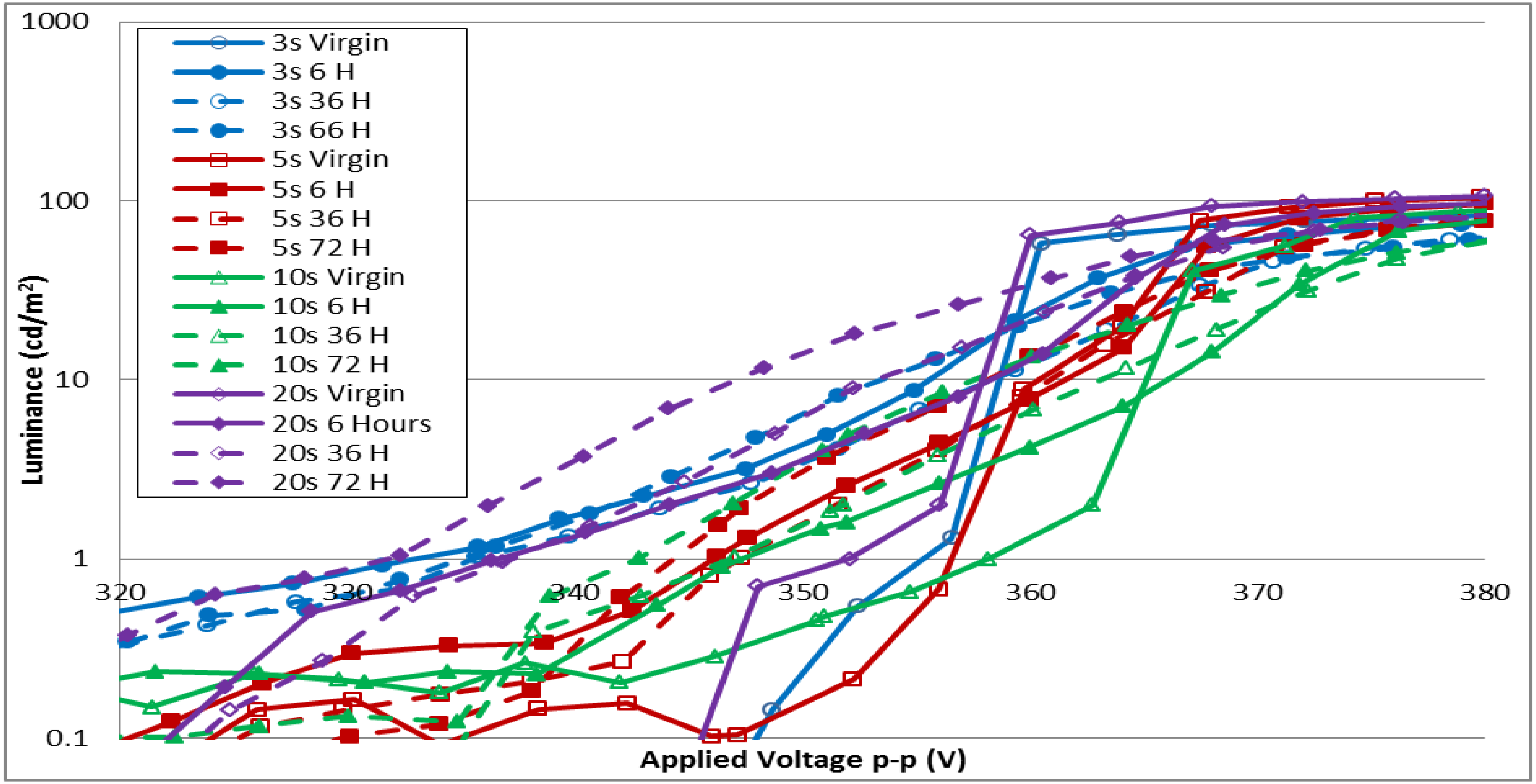

Figure 6.22 - Design six L-V curves at virgin, 6, 36 and 72 hours for 3, 5, 10 and 20 second step intervals.

Figure 6.22 shows the L-V curves for design six for the four step intervals at virgin 6, 36 and 72 hours. The 3 second virgin curve is the sharpest of the four but it also has the largest threshold shift and demonstrates the most softening. Although the L-V curve of virgin 5 seconds is not the sharpest, a kink is present towards the knee of all the curves, it exhibits the least amount of softening and shifting. 10 seconds have a similar amount of shifting to the 5 seconds but the curves are softer in comparison. The virgin 20 second curve shows softening around the threshold point as previously discussed. The negative shift is larger than for 5 and 10 seconds but marginally less than for 3 seconds. The 5 second curves exhibit the best aging behaviour.

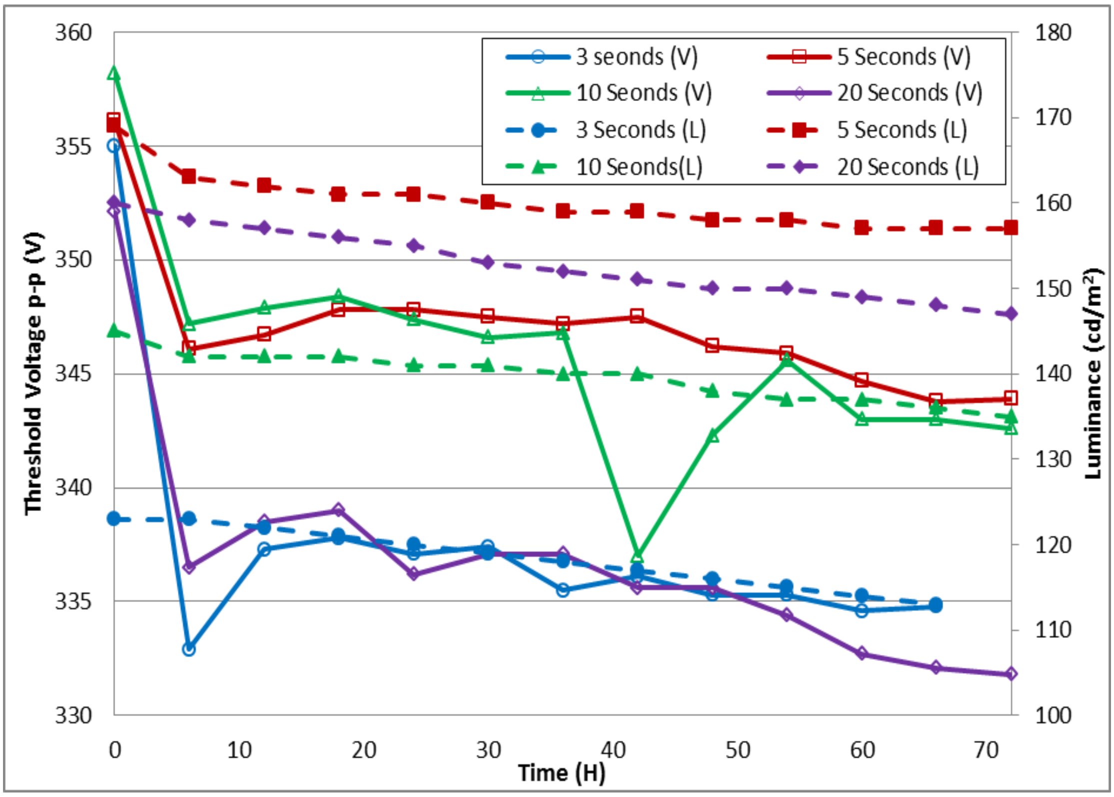

Figure 6.23 - Threshold voltage and luminance over the 72 hour lifetime period for design six.

The threshold voltage shift is shown in Figure 6.23. The 5 second interval step has the lowest threshold shift at 14Vp-p, the 10 second step is slightly larger at 16Vp-p and 3 and 20 seconds both demonstrate a 20Vp-p shift. The luminance change is also shown in Figure 6.23. Over the 72 hours, the 10 second step has a luminance drop of 6.9% followed closely by 5 seconds that has a decrease of 7.1%, half of which occurs in the first 6 hours, 3 and 20 seconds have voltage drops of 8.1% and 8.8% respectively.

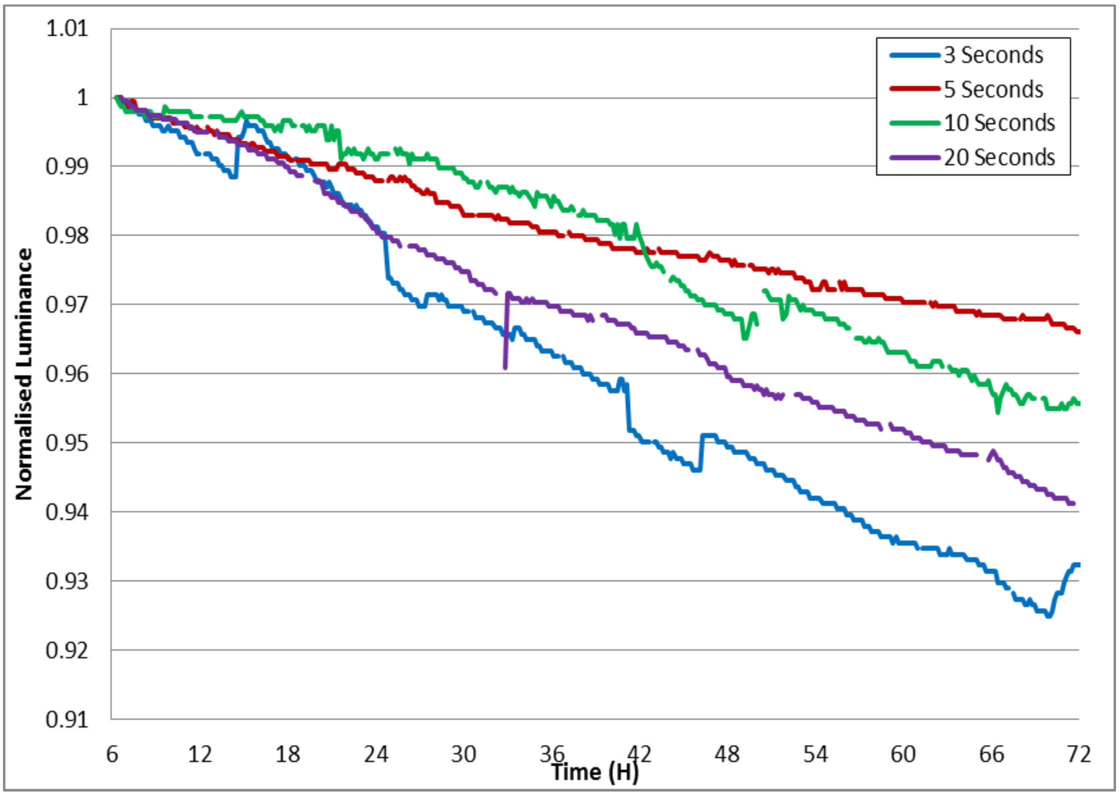

Figure 6.24 - Normalised lifetime of design six for 3, 5, 10 and 20 second step intervals.

Figure 6.24 shows the normalised luminance for the four different step intervals. A clear difference can be observed between the four timings. For the first 36 hours the 10 second lifetime reduces at the slowest rate, but a rapid decrease over a 6 hour period means overall the 5 second lifetime exhibits the best performance. The 3 second lifetime reduces at the quickest rate reaching its lifetime in just under half the time of the 5 second interval.

The charges Q_{pol}, Q_{leak}, Q_{cond} and Q_{relax} as obtained from Q-V analysis are shown in Figure 6.25 - 6.28 respectively.

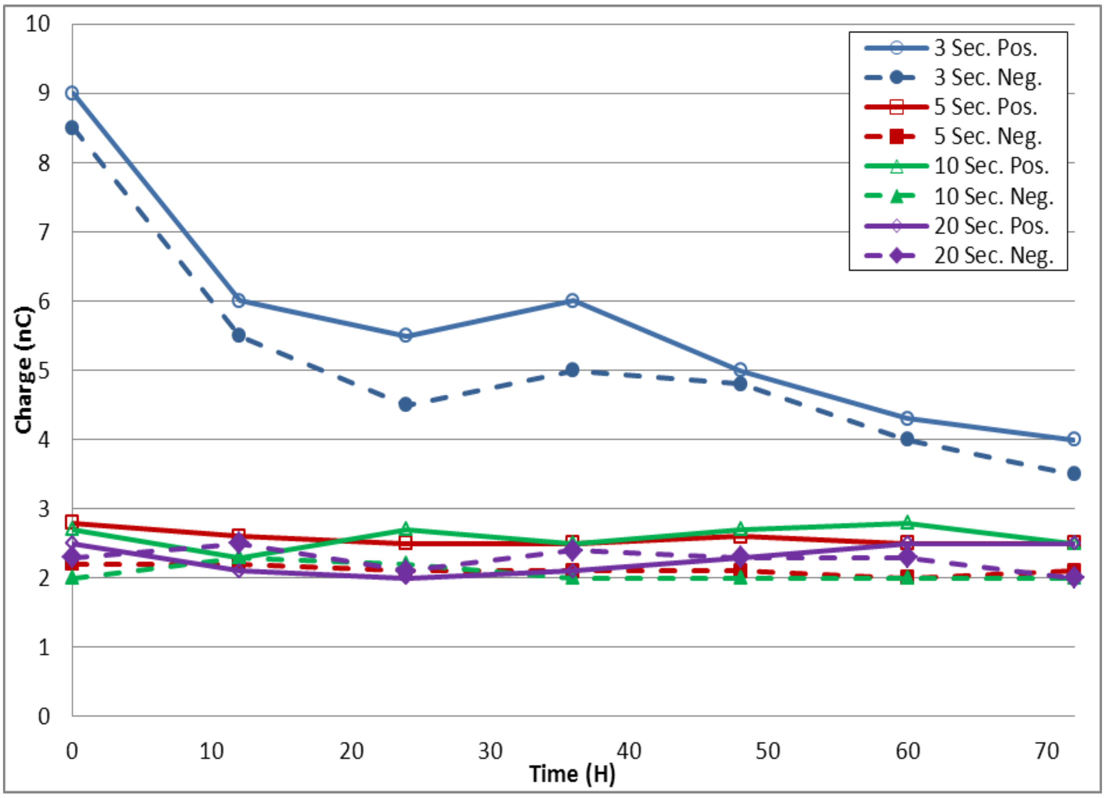

Figure 6.25 – Polarisation charge as a function of time of design 6 for 3, 5, 10 and 20 second step time intervals.

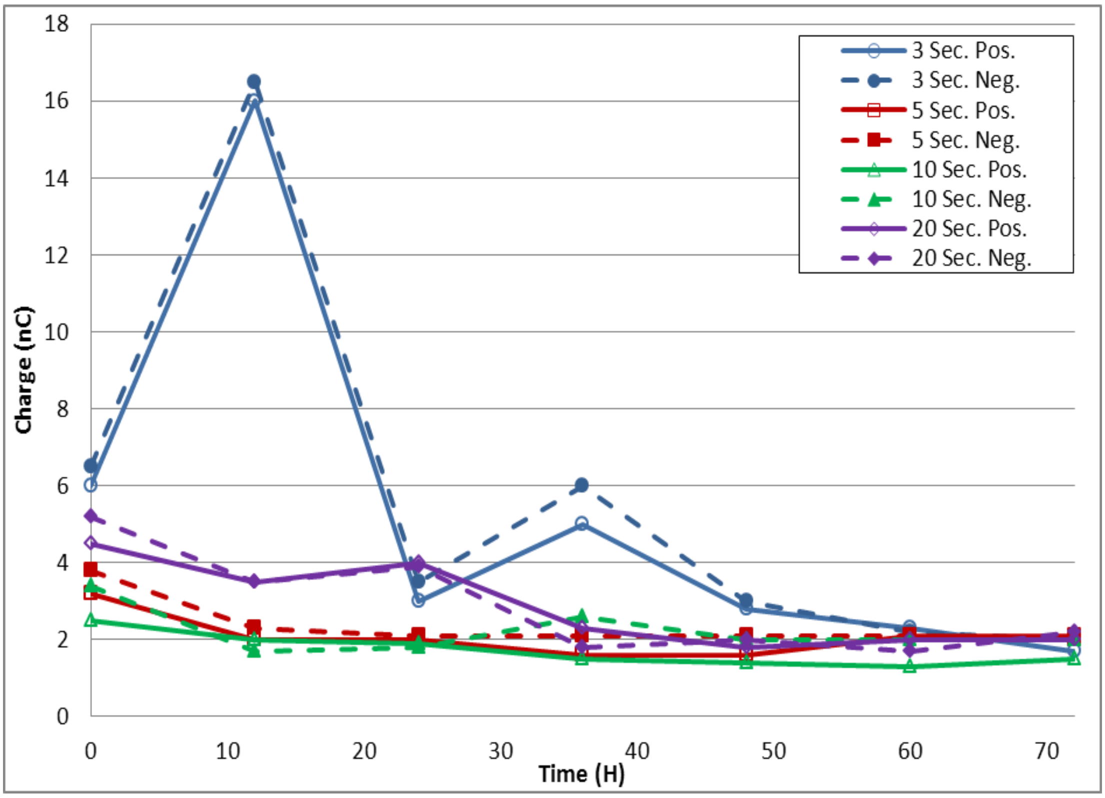

Figure 6.26 – Leakage charge as a function of time of design 6 for 3, 5, 10 and 20 second step time intervals.

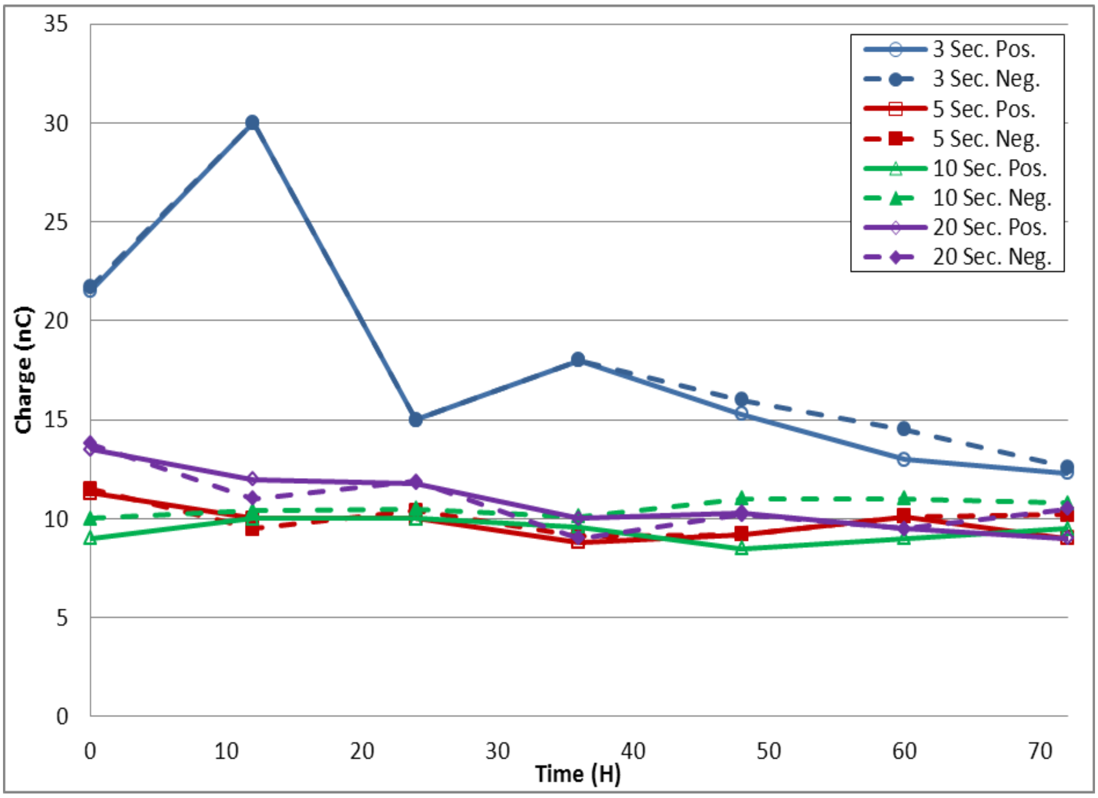

Figure 6.27 – Conduction charge as a function of time of design 6 for 3, 5, 10 and 20 second step time intervals.

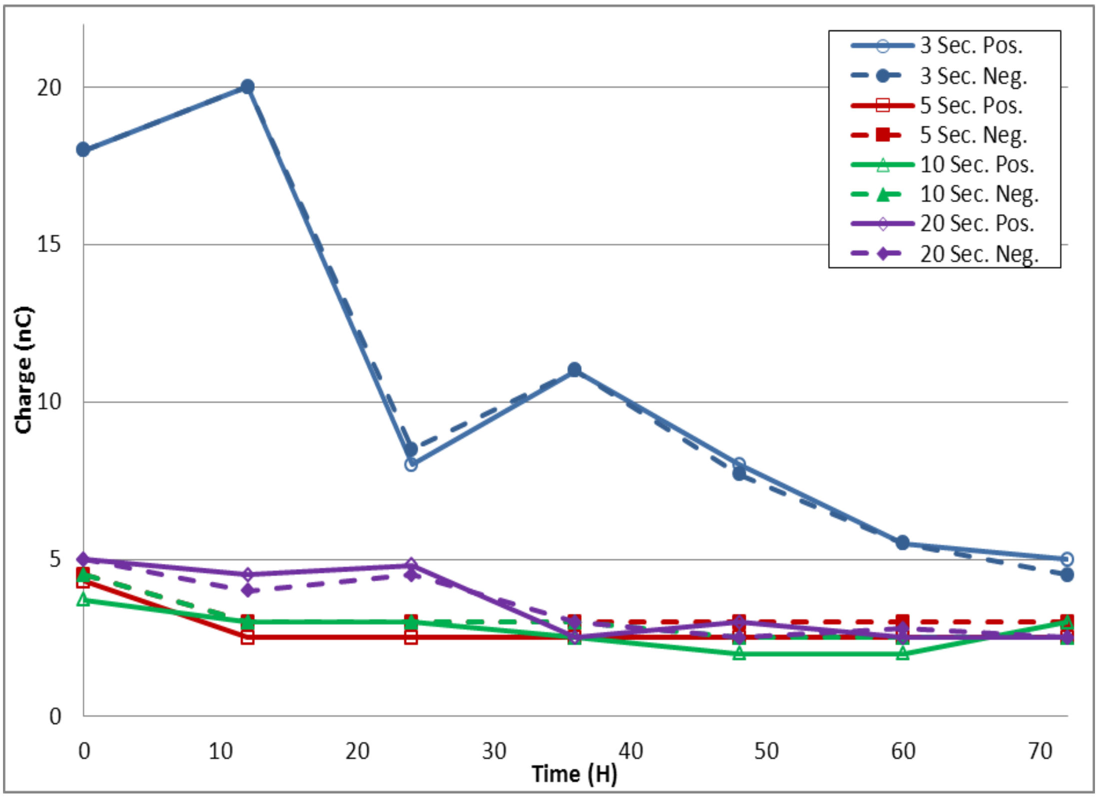

Figure 6.28 – Relaxation charge as a function of time of design 6 for 3, 5, 10 and 20 second step time intervals.

The charges for both negative and positive pulses are shown as ALD devices are known to age asymmetrically. There is little evidence of any major difference in the charges over the 72 hour aging period; this may suggest that the time window used for experimentation is not long enough for any such differences to manifest. However the transient analysis show in Figure 6.29 would suggest this is not the case, for the virgin waveform the negative pulse emits the greater luminance, after 24 hours the luminance emitted from the positive and negative pulses is equal, the final transient after 72 hours shows the positive pulse now emits the higher luminance. The transient analysis demonstrated a behaviour not often seen in ZnS:Mn thin films in that the trailing edge emission was greater than the leading edge.

This has been reported for ALD devices grown with $ZnCl_2$ as a precursor (108) as is the case with these devices. This typically observed when there is a large polarisation charge however the polarisation charge for the ZnS:Mn sputtered device seen in Figure 3.3 is greater than that of the ALD devices yet no trailing edge emission was observed.

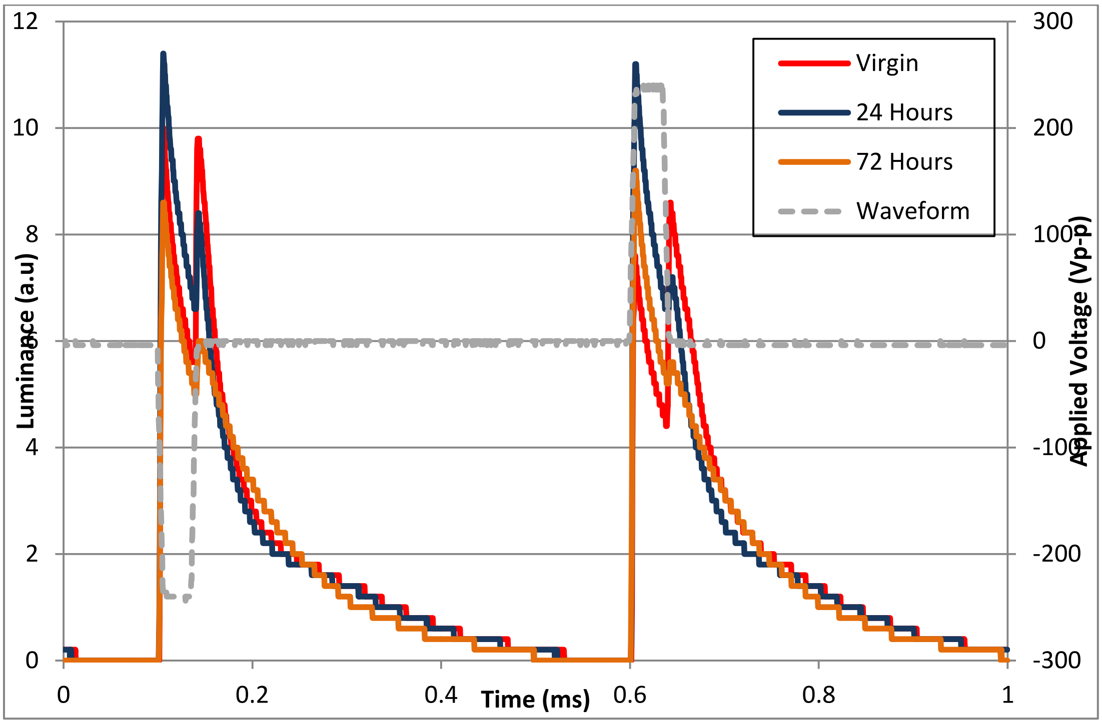

Figure 6.29 – Transient analysis of design 6 taken at virgin, 24 hours and 72 hours.

6.3.2 Step Interval and Voltage Increment Investigation

After the successful step interval trials, the next phase is to investigate the effect of the voltage increment and the time taken in between each step. Ideally design six would have been used as this provided the most conclusive results previously; unfortunately most of the unavailable devices shown in Figure 6.4 are design six which limited the number of devices available. Therefore an alternative design must be used, due to their low luminance levels designs three, four and five are ruled out leaving one and two. Due to failures to design two discussed in section 6.6, design one is used for the following investigation. The 3 second step interval is omitted from this stage of the investigation due to poor lifetime performance and high failure rates.

The devices are aged as before using a 1 kHz bipolar trapezoidal waveform with a 5, 10 or 20Vp-p increase every 5, 10 or 20 seconds. A 1.5kΩ series resistor is used for current protection at room temperature in ambient conditions. They are aged at a voltage of 480Vp-p.

Please note there are no results shown for 5Vp-p 10 seconds, 20Vp-p 5 seconds and 20Vp-p 20 seconds as these experiments did not last longer than 18 hours.

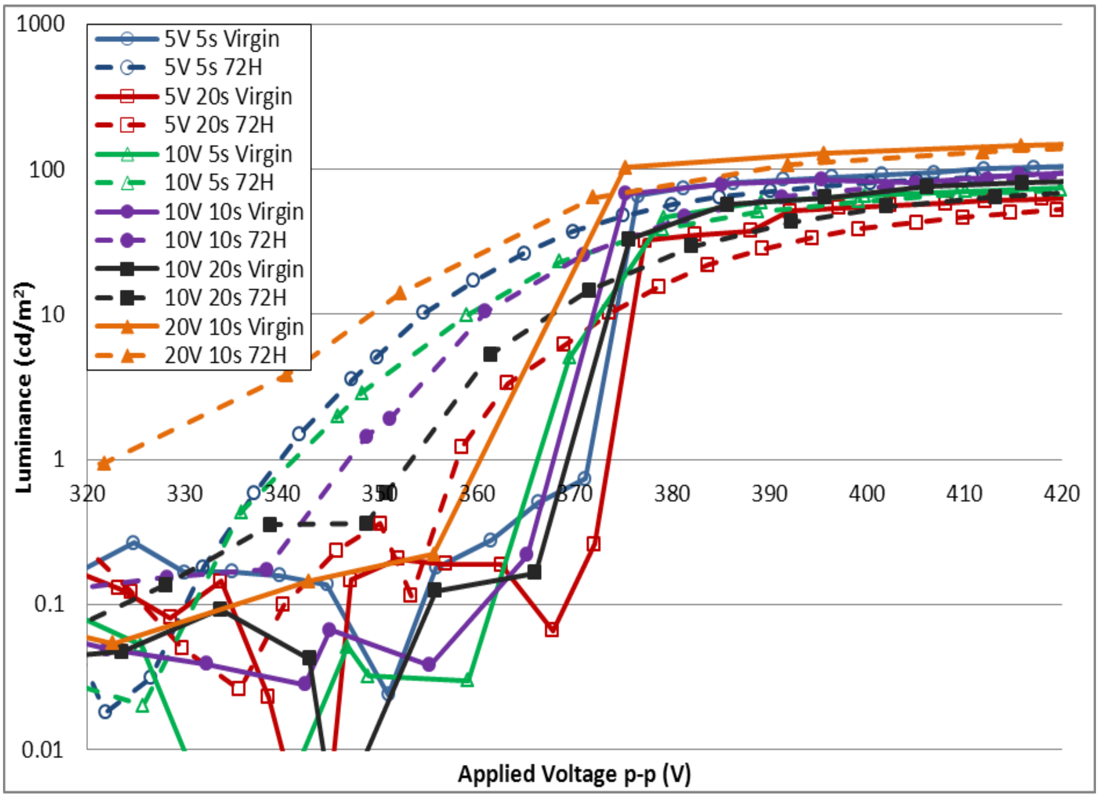

Figure 6.30 - Virgin and 72 hour L-V curves

Figure 6.30 shows the virgin and 72 hour L-V curves for design one subjected to various turn on voltage step increments and step time intervals. The least amount of threshold shift was demonstrated by the two pixels that had a 20 second step interval at 14.6Vp-p, the largest amount of negative threshold shift was seen for the pixel with the largest voltage step increment at 33.5Vp-p. Despite the low threshold shift the 5Vp-p 20 second pixel displays the most softening.

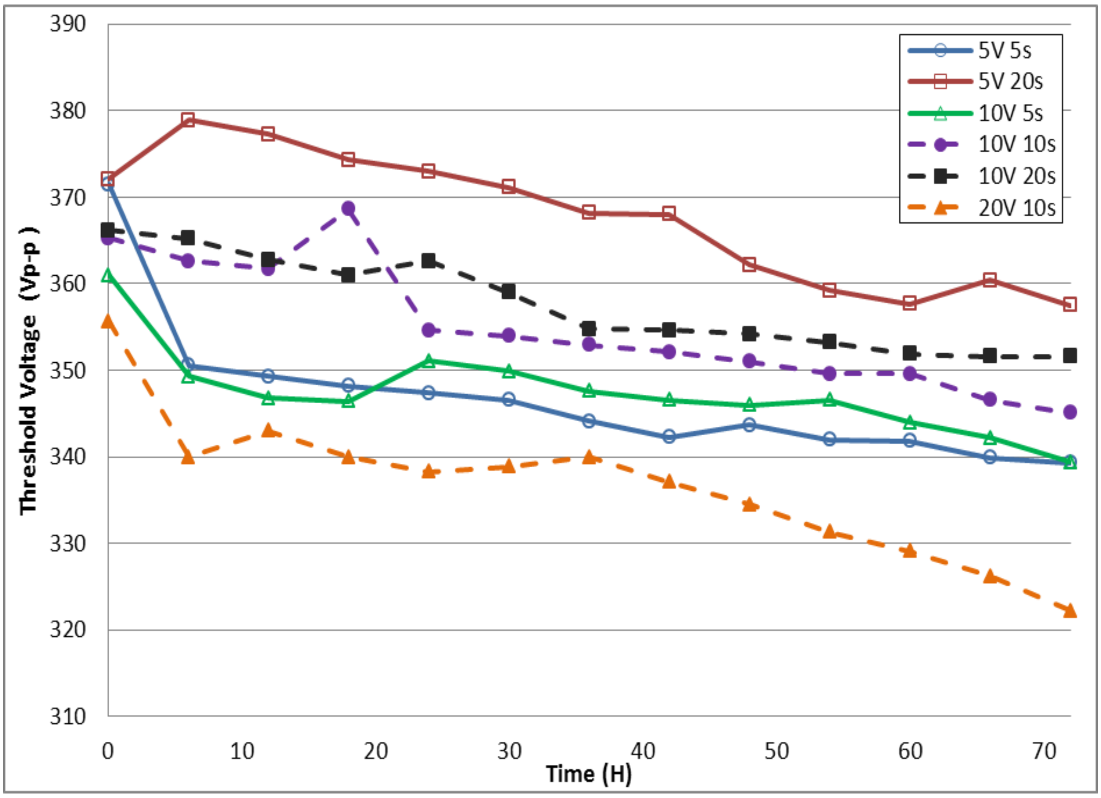

Figure 6.31 - Threshold voltages for design one subjected to various combinations of voltage and time increments.

Figure 6.31 demonstrates how the threshold voltage changes over time for pixels subjected to different combinations of voltage and time increments. The 5Vp-p 20 second pixel has an initial shift in a positive direction before a continuous negative shift, after 30 hours the threshold voltage is below that of the virgin L-V curve. It is not thought that the long burn-in time is the cause of this behaviour, as the previous 4Vp-p 20 second experiments do not demonstrate the same trend. The low luminance level compared to other pixels would indicate that there may be defects within the pixel which caused the positive shift.

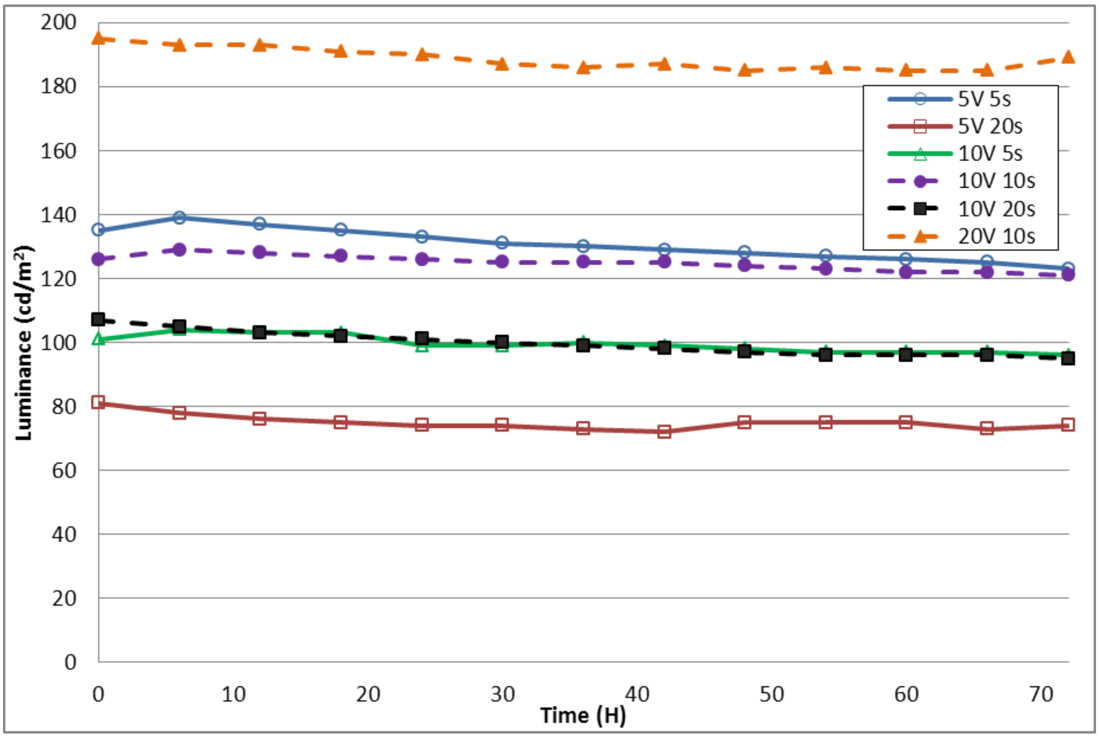

Figure 6.32 - Luminance as a function of time for design one subjected to various voltage and time increments.

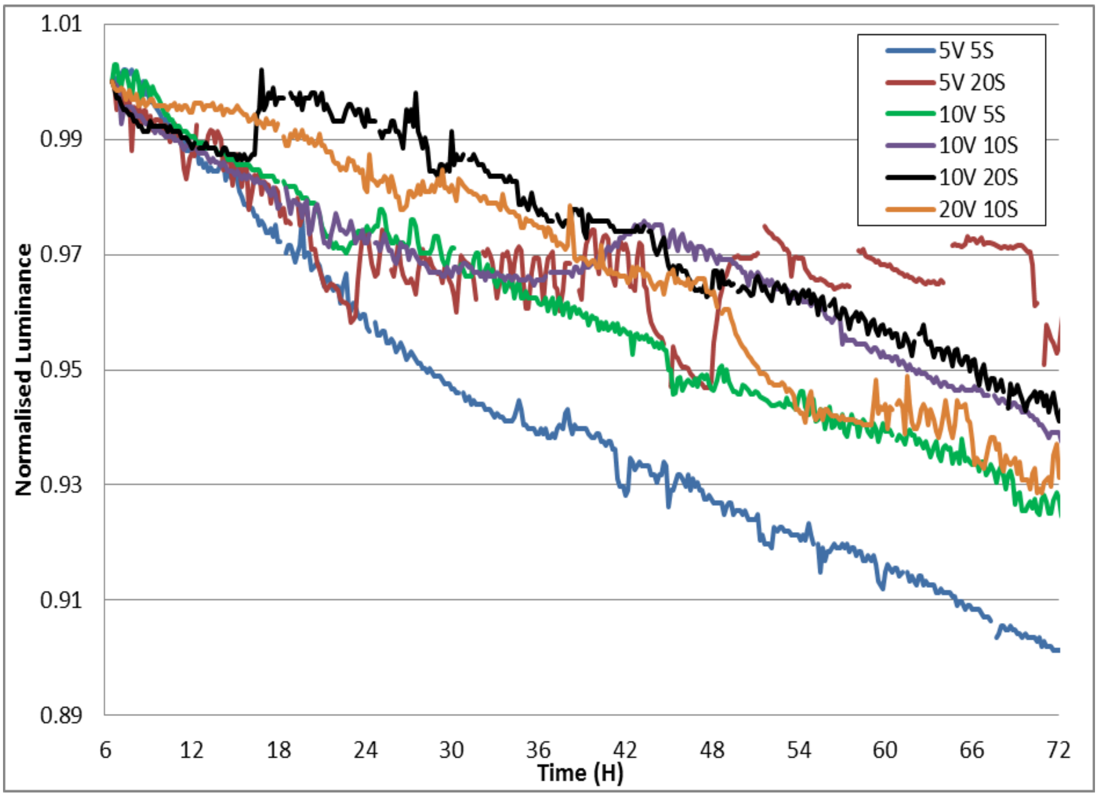

Figure 6.33 - Normalised lifetimes for design one subjected to various voltage and time increments.

Figure 6.32 show the luminance for the design one pixels, the luminance is fairly stable over the 72 hour lifetime period with the 5Vp-p 5 second pixel showing the highest decay in luminance. It is not thought that the maximum achievable luminance of the pixels is affected by the burn-in time, although there is a clear difference between some of the luminance levels. 5Vp-p 5 seconds and 10Vp-p 10 seconds are relatively similar and are both the same pixel from different displays as are 10Vp-p 5 seconds and 10Vp-p 20 seconds, 5Vp-p 20 seconds is also the same pixel but possibly from a device with defects as discussed previously.

The normalised lifetime is shown in Figure 6.33. The 5Vp-p 5 second pixel had the fastest decay rate with a predicted lifetime of 12 1/2 days, 5 days less than that of the 4Vp-p 5 second pixel, which had a slightly longer burn-in time of 7 minutes 40 seconds in comparison to 6 minutes 15 seconds. The 5Vp-p 20 second pixel had the longest predicted lifetime of nearly 28 days although it is unlikely that the pixel would last this long as it becomes very erratic half way through the lifetime period. The 10Vp-p 20 second pixel had the next best lifetime at only a day and a half less than the best performer.

6.3.3 Waveform Burn-in

An initial investigation was carried out using the remaining design six devices involving studying the effect on the lifetime of a pixel when turned on using different waveforms. 1kHz sinusoidal, square and triangular waveforms were used as an alternative to the bipolar trapezoidal waveform. The pixels were driven at a voltage 120Vp-p above the threshold voltage with the specified voltage waveform for 6 hours. After this time, a second L-V curve would be taken. The pixel would then be driven using the trapezoidal waveform for the remaining 66 hours, L-V curves were again taken every 6 hours as previously. The pixels were driven using a 4Vp-p increment every 5 seconds. The L-V curves for each of the three waveforms are shown in Figure 6.34, Figure 6.35 and Figure 6.36, where the data drops below the x-axis is considered noise and is therefore omitted. In each figure the virgin and 6 hour L-V curves are shown for the respective waveform, as well as the 6 hour and final L-V curve for the bipolar trapezoidal waveform. For reference on how the waveform affects the aging characteristics the virgin, 6 and 72 hour L-V curves from the previous 4Vp-p 5 second experiments are included in the figures.

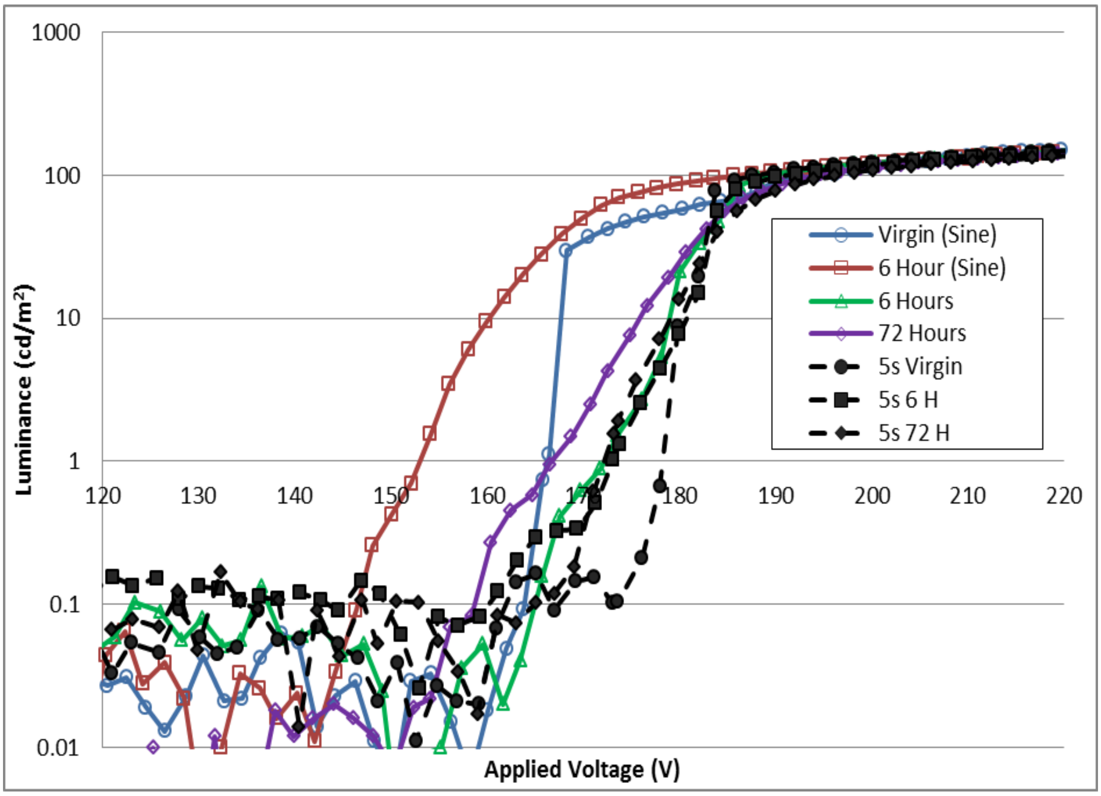

Figure 6.34 - L-V curves for 6 hour sinusoidal burn-in.

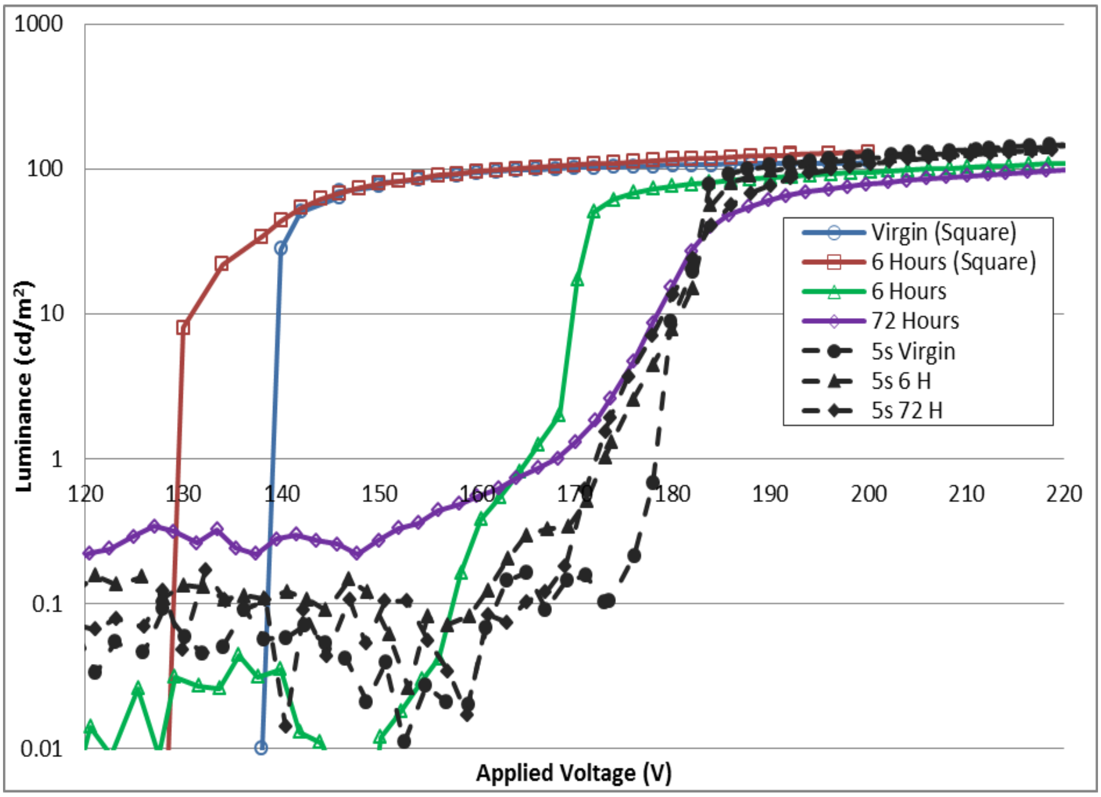

Figure 6.35 - L-V curves for 6 hour square wave burn-in.

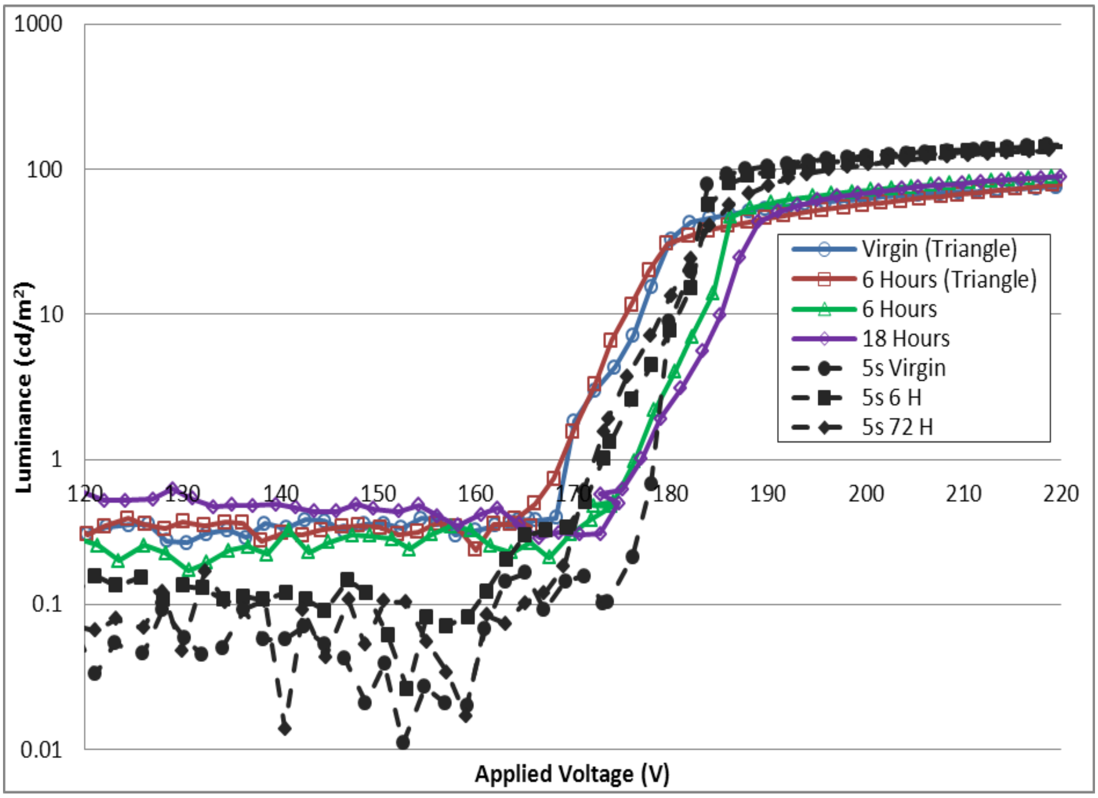

Figure 6.36 - L-V curves for 6 hour triangular waveform burn-in.

The 6 hour sinusoidal burn-in has the largest threshold shift over the first 6 hours, with a 13.6V negative shift, followed by the square wave with 9.6V; the triangular waveform resulted in just a 0.4V shift. The triangular and square waveforms also demonstrated very little softening of the 6 hour L-V curve. The 6 hour sinusoidal burn-in produced the worst aging characteristics with a large threshold shift and softening. After the 72 hours the final L-V curve demonstrated greater softening compared to the final L-V curve that had been burnt-in using the trapezoidal waveform, there was also a greater threshold shift between the 6 and 72 hours of the sinusoidal burn-in in comparison. Initially the square waveform produced very little softening but after the 72 hours the L-V curve was almost identical to the 72 hour trapezoidal burn-in curve. The Triangular waveform produced the best aging characteristics, although the final L-V curve is after only 18 hours due to failure but the virgin and 6 hour L-V curves are almost identical, very minimal softening and shifting has occurred in this time period where previously the largest changes to the curve had occurred.

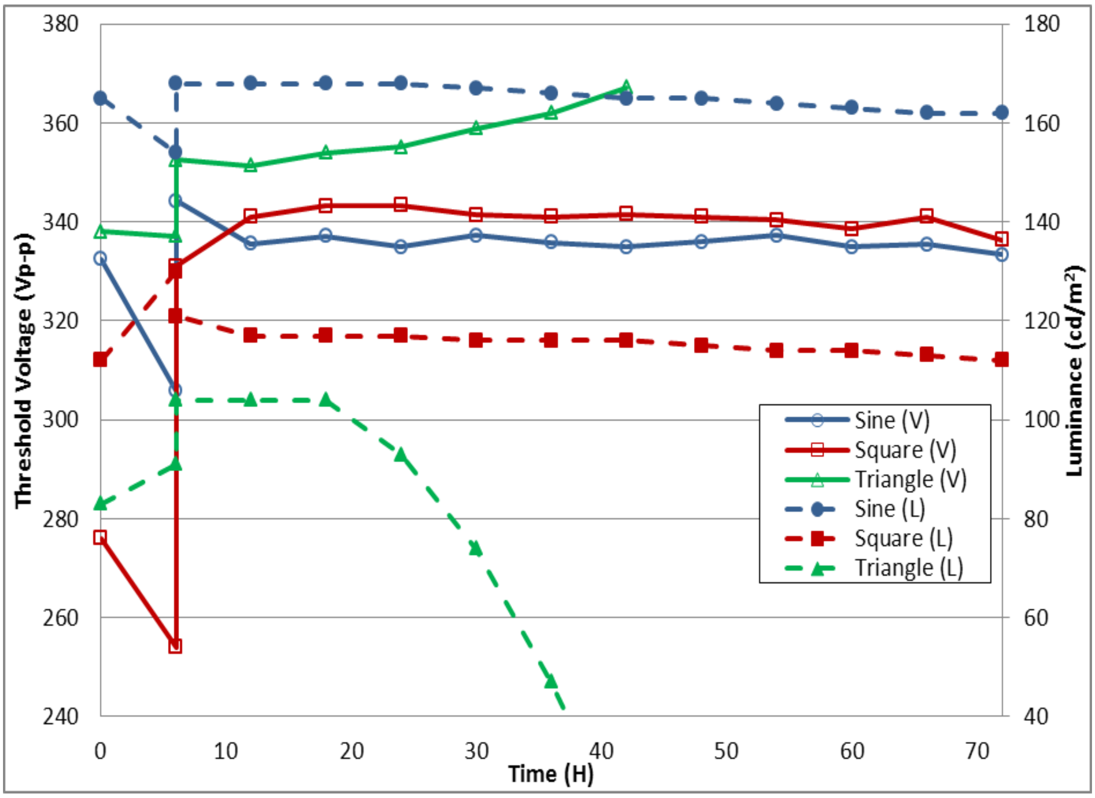

Figure 6.37 - Threshold voltage and luminance as a function of time for the three different waveforms.

The luminance and threshold voltage change of the three waveforms as a function of time are shown in Figure 6.37. During the initial 6 hours, whilst being driven by a square waveform, there is a large negative threshold shift, as previously seen with the trapezoidal waveform. After the pixel is switched to being driven by a trapezoidal waveform there is a positive threshold shift for the first 18 hours after which the threshold slowly shifts in a negative direction. The sinusoidal burnt-in pixel has large threshold shifts for the first 6 hours, for both waveforms, after which there are very minimal shifts (< 2Vp-p) in either direction. The threshold voltage is relatively stable after 12 hours. The triangular waveform resulted in minimal shifts during the first 6 hours of each waveform, and for the second 6 hour period under the trapezoidal waveform; < 1.5Vp-p. After this point the device begins to fail and as a result the threshold voltage begins to shift in a positive direction.

The luminance over the first 6 hour period showed an increase for the square and triangular waveforms with a 16.1% and 9.6% increase respectively. The trapezoidal waveform would often see a small increase in luminance, but this would usually have decreased down to the original value before the end of the 6 hour period. The 6 hour sinusoidal waveform burn-in resulted in 5.5% luminance decrease. The luminance after the pixels were switched to a trapezoidal waveform demonstrated very little decay for the first 30 hours; 1.2% sinusoidal and 0.9% square. No decrease is observed in the first 18 hours, excluding the initial 4cd/m^2 drop by the square wave pixel. After this point, for the remaining 36 hours the decay had increased to a 3.6% and 4.3% for the sinusoidal and square wave respectively. The luminance of the triangular waveform pixel remained constant at 104cd/m^2 before decreasing rapidly due to failure.

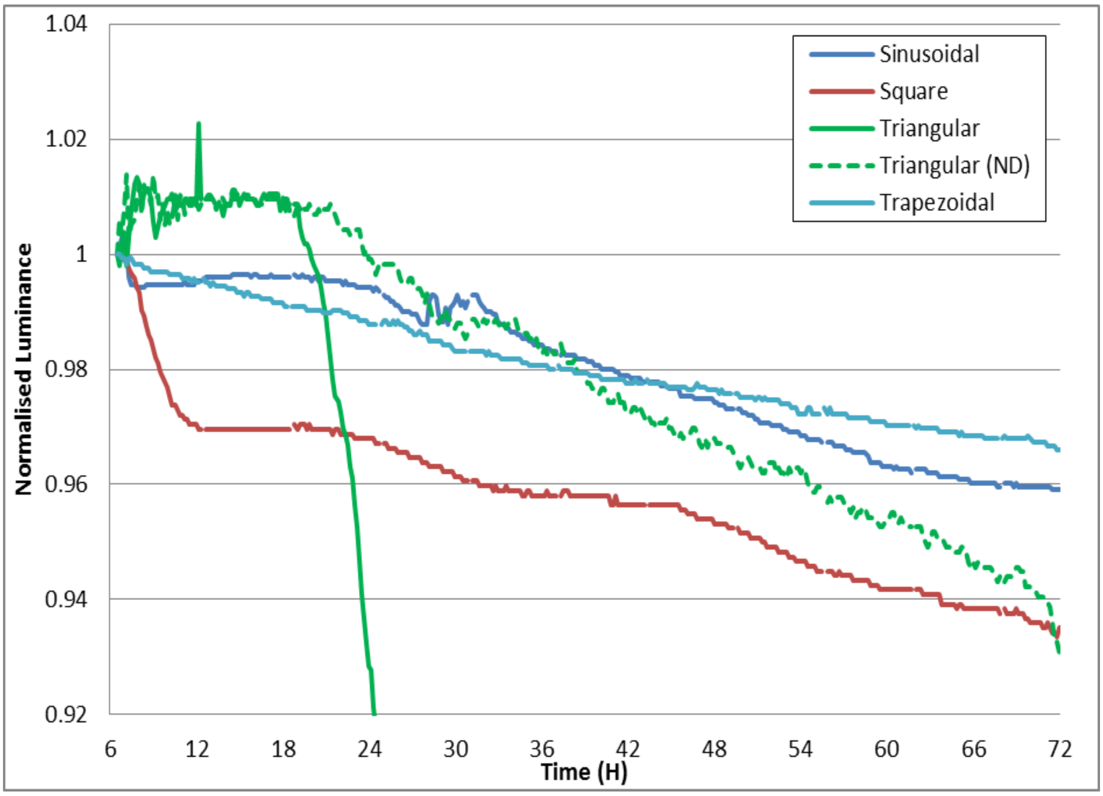

Figure 6.38 - Normalised lifetime of the 6 hour waveform burn-in pixels.

The normalised lifetimes of the different waveforms are shown in Figure 6.38 along with the best previous trapezoidal result for design six. A second triangular lifetime is shown that lasted the 72 hour period, but no other data is available for this pixel. The triangular waveform pixel shows little sign of decay over the first 12 hours but then rapidly decreases resulting in predicted lifetime of just less than 26.5 hours. The square waveform had an initial sharp decrease over the first 6 hours before remaining constant for the next 6, it then continued to decay at a steady rate resulted in a predicted lifetime of just over 17 days. The sinusoidal waveform had initial large decay rate over the first hour before settling down and increasing slightly over the next 20 hours. For the final 6 hours the decay rate had again settled and the luminance remained constant giving the pixel a predicted lifetime of 33 ½ days. None of the waveforms outperformed the trapezoidal waveform.

6.4 Discussion of Burn-in Parameters

The key results from Figure 6.6 to Figure 6.21 for the burn-in optimisation carried out on all six designs can be seen in Table 6.2. The results clearly demonstrate that design six is the optimum micro-mirror structure in regards to the luminescent emission as well as device lifetime. With the exception of the 3 seconds data set design six consistently had the highest luminance by a large margin; for 20 seconds it was almost double the next highest luminance which was design one. With regards to the predicted lifetime the design six devices were constantly the best performers with the 5 second and 10 second devices achieving almost double the next best predicted lifetime. The predicted lifetime is calculated in Excel by applying a linear trend line to the normalised three day trend and then using the accompanying equation to calculate where the three day trend crosses the y-axis at 0.5 as this would correspond to 50% of the original luminance. The lifetimes of the devices are relatively short, this is due to the fact that the devices were fabricated circa 2005 and were not stored under vacuum which can cause the devices to degrade. With regards to the micro-mirror design structure, design six's arms are twice the length of the other designs and as such the pitch is also larger, as these are the only difference between designs three and six it would appear that the longer arms aid with light output.

		L_{MAX}	L_0	L_{72}	L_{drop} %	V_{TH0}	V_{TH72}	Gradient (-negative)	Predicted Lifetime
3 Seconds	D1	130.5	125	112	7.6	359.4	341.8	0.0011959	17.6
	D2	81.98	76	19	66.9	376.8	377.3	-	2.7
	D3	67.11	68	11*	-	366.2	369.2*	-	0.9
	D4	60.13	60	48	10.2	354	344	0.0014124	14.9
	D5	55.19	54	49	8.1	354.4	338.5	0.0013706	15.4
	D6	125.9	123	113*	6.7	355	334.8*	0.0011882	17.8
5 Seconds	D1	162.9	159	143	8.3	358.9	338.7	0.0013291	15.9
	D2	112.5	114	82	7.4	339.3	337.7	0.0011238	18.8
	D3	63.07	63	56	9	358.2	342.2	0.0013755	15.4
	D4	77.52	69	58	9.6	347.9	336.3	0.0015528	13.7
	D5	55.75	50	48	9	357.7	340.8	0.0013812	15.3
	D6	171.2	169	157	3.5	356.1	343.9	0.0005583	37.6
10 Seconds	D1	127.5	118	84	8.6	363	351.5	0.0015504	13.7
	D2	118.4	113	90	8.2	363.4	346.6	0.001313	16.1
	D3	72.03	72	52	11.9	365.1	346.9	0.0018038	11.8
	D4	87.59	70	60	10.7	358	340.7	0.0016324	13
	D5	54.63	55	6	79.3	359.9	356.2	-	3.1
	D6	148.8	145	135	4.4	358.2	342.6	0.0006622	31.7
20 Seconds	D1	87.4	87	81*	-	364.1	352.7*	-	1.7
	D2	93.07	95	82	8.5	356	342.8	0.0014124	15
	D3	64.85	64	56	8.5	360.5	342.1	0.001412	15
	D4	72	71	61	12	348.9	337	0.0017422	12.2
	D5	56.85	56	48	11.1	360	340.5	0.0016711	12.7
	D6	162.3	160	147	5.9	352.1	331.8	0.0009249	22.8

*Table 6.2 – Key device results, where L_{max} is the maximum luminance achieved over the lifetime,L_0 and L_{72} are the luminances of the first and last L-V curves, L drop is the luminance percentage drop over the final 66 hours, V_{TH0} and V_{TH72} are the threshold voltages for the first and last L-V curves, Gradient is the negative slope of the linear trend line added in Excel and the predicted lifetime is the time (in days) that the pixel would take to reach 50% of its starting luminance presuming the rate of decay remains constant. All luminance measurements are in cd/m^2 and all voltage measurements are in Vp-p, * indicates the pixel died during the experiment.*

For the micro-mirror design dimensions the data would suggest that the larger the pull back the lower the luminescent emission is. Design one continually out performs design two, with the exception of the pixel that failed. Design two out performs design three and so on. The lifetimes however do not follow the exact same trend, design two, with the exception of the device that failed, out-performed design one by ~ 2 ½ days. The sole difference between designs four and five is the PSK edge stop, which is an extra micro-mirror structure around the edge of each pixel. Whilst this addition may give the pixel better definition and therefore the displayed information will be clearer, it resulted in a 20% reduction in luminance. The results suggest the luminescent performance of design six could be improved further by reducing the pull back from 1.5µm to 0.5µm.

The time taken to burn-in a virgin device has shown to have an effect on the lifetime, with the 5 second step interval being the optimum of the four times used. This effect is best seen in design six; it has the longest lifetime and demonstrates reduced aging. 5 seconds was also the only time to produce a complete data set without failures. It was thought that the longer the time taken to burn the device in the better its performance would be as there would be less stress placed on the device and more chance of any defects being able to self-heal. A 3 second step interval was clearly too quick as half the devices failed within the 72 hour period, however the lifetime of the devices that did not fail are the longest of the four time intervals. The lifetimes of all of the devices decreased as the step time interval was increased, with the exception of design three at 20 seconds which was longer than at 10 seconds but not than at 5 seconds. The lifetimes of design six follow the same trend apart from at 3 seconds; this is the lowest lifetime for the design by 5 days. Whilst the device did fail it did not appear to be a gradual failure as the luminance remained stable up until the point of catastrophic failure; however the defects that caused the device to fail could also have caused it to underperform. The results would indicate that the original hypothesis was incorrect and the shorter the time taken to burn-in a device the better the lifetime performance. With this though comes a trade-off between lifetime and stability, a shorter burn-in time gives longer lifetimes but with it comes the increased risk that the device could fail at any moment.

The n-shift shown in the threshold voltage has been attributed to the creation of static space charge within the phosphor layer (56, 57), which is known to reduce over time (109). The largest shift is seen in the first 6 hours, after which there is a slight p-shift but then a gradual n-shift for the remainder of the lifetime. No clear trends were evident within the threshold voltage data leading to the conclusion that the creation of space charge is something that cannot be controlled by the burn-in parameters. A further investigation would be required to establish a better understanding of the link between the threshold voltage shift and the space charge within the phosphor layer and to determine other possible factors that could be contributing to the reduction of the threshold voltage.

The results from the step time and voltage increment investigation showed the opposite trend from the previous study, as the overall burn-in time was increased the lifetime also increased. The timings along with the predicted lifetimes of the devices as well as the design one results from previous study are shown in table 6.3.

Voltage Increment (Vp-p)	Time Interval (Seconds)	Total Burn-in Time	Lifetime (Days)	Gradient (-)
5	5	6 min 10 sec	12.7	0.0016801
5	20	24 min 40 sec	27.9	0.0007530
10	5	3 min 10 sec	17.8	0.0011905
10	10	6 min 20 sec	23.1	0.0009106
10	20	12 min 40 sec	26.5	0.0007948
20	10	3 min 20 sec	20.6	0.0010229
4	3	4 min 39 sec	17.6	0.0011959
4	5	7 min 45 sec	15.9	0.0013291
4	10	15 min 30 sec	13.7	0.0015504
4	20	31 min	1.7	-

Table 6.3 - Total burn-in times and lifetimes for varying voltage and step time increments for design one.

The previous best lifetime result obtained for design one was 17.6 days, all bar one of the results achieved during the second study out performed this with the best result being nearly 9 days longer. Interestingly the results would indicate that it is not the time itself taken to burn-in a pixel but the parameters that are the important factor, the 5Vp-p 5 seconds and 10Vp-p 10 seconds burn-in times differ by just 10 seconds but the lifetimes differ by 11 days. A lot more work is required in this area to fully understand the impact the time and voltage increments have on the lifetime and stability of devices.

Whilst the waveform burn-in experiments produced some interesting results with regards to the luminance characteristics in the first 18 hours, none of them out-performed the trapezoidal waveform. A more detailed and comprehensive investigation is essential in this area along with the variation of the frequency of the waveform in order to produce a set of optimum burn-in parameters.

6.5 Sputtered SRELD

As a comparison of the different deposition methods, sputtering and ALD, similar lifetime experiments were planned for the six different designs for the sputtered SRELD. Previous work carried out on these devices indicated that they suffered from high failure rates when attempted to be burned-in with a high voltage increment and small time step interval, for this reason a 4Vp-p 10 second increment is used. Figure 6.39 shows the lifetime of the sputtered and ALD SRELD devices, both are aged at a voltage ~120Vp-p above the threshold voltage. No L-V curves are taken during the 20 hour lifetime period as attempts to do so results in failure of the sputtered pixels. The luminance of the sputtered devices is not as varied as that of the ALD devices and they also generally have a higher luminance. Figure 6.40 shows the normalised luminance of the six designs for the two deposition methods. The sputtered devices decay at a much quicker rate than the ALD and there is a greater variance through the four designs that are depicted. In the case of the sputtered devices design six has the shortest lifetime, contradictory to the

ALD results. Design one had the best lifetime but this was still outperformed by all of the ALD designs.

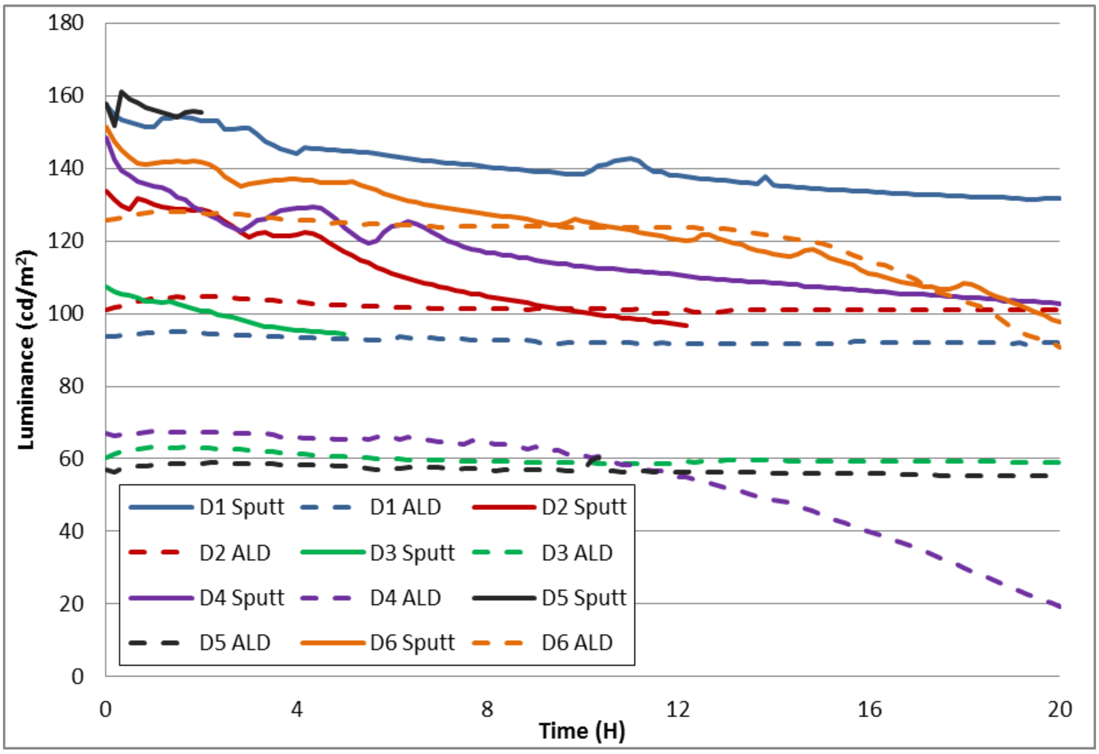

Figure 6.39 - Lifetime of all six designs fabricated using RF magnetron Sputtering and ALD.

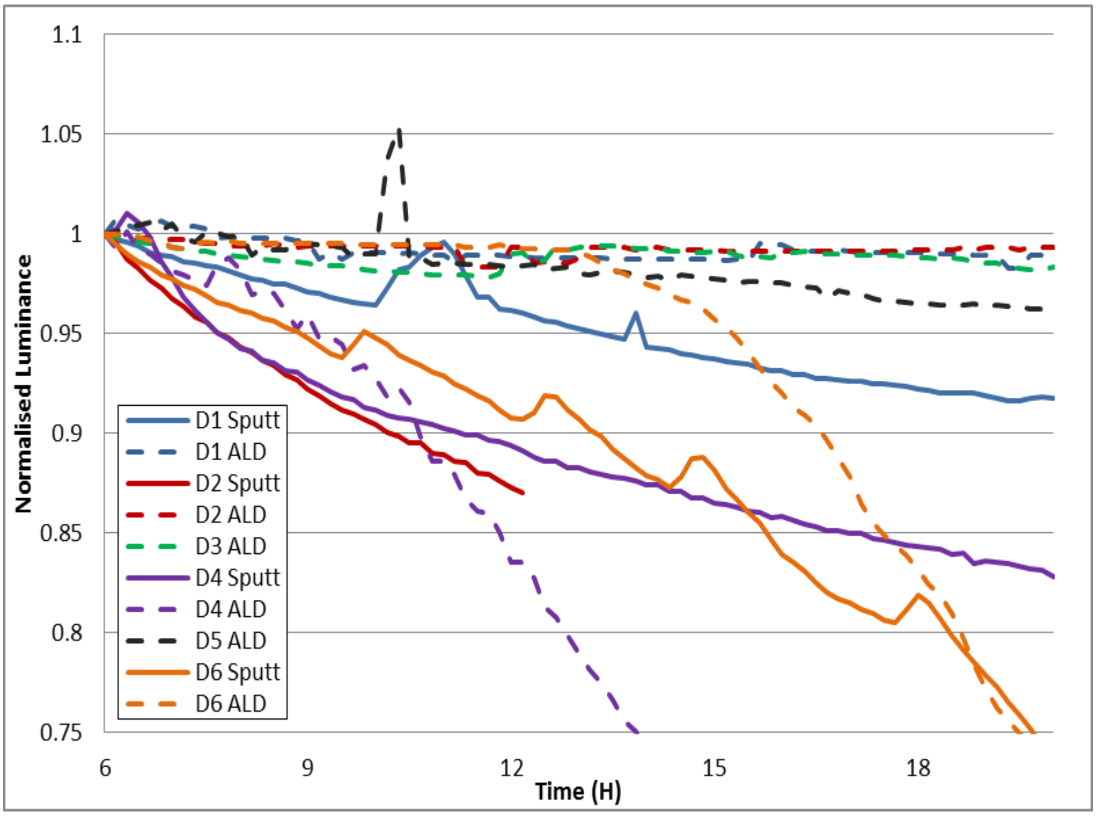

Figure 6.40 - Normalised lifetime of all six designs fabricated using RF magnetron Sputtering and ALD.

6.6 Device Failure

The two different deposition methods resulted in different failure methods of the pixels, the electrodes had similar failures but on differing scales. The ALD wafer that the tested devices were sourced from suffers from delamination around the edges; most of the damaged devices shown in Figure 6.4 are suffering from this and have started to peel. None of the devices tested showed any sign of delamination and were possible devices tested were picked from areas away from the defect.

The sputtered SRELD failed due to localised destructive breakdown defects (LDBD), this type of defect has been associated with the voltage increase during the burn-in process (110). Initial trails carried out by the author prior to this body of work demonstrated the need to burn the pixels in slowly. A 4Vp-p increase every 10 seconds was found to be sufficient in order to get an L-V curve measurement, any attempts to use a larger voltage increase or smaller step time interval resulted in breakdown during the measurement. The lifetime results obtained indicate that whilst these parameters may be sufficient for a single L-V measurement, optimisation is still required in order to achieve a successful lifetime. Figure 6.41 shows several sputtered SRELD devices that have succumbed to LDBD, this type of failure occurs at weak points in the pixel usually caused by large particles in the structure or voids. A pinhole breakdown occurs which is then followed by overheating, the dielectric layer often promotes self-healing in order to isolate the defect and repair it due to the high current melting the dielectric material and filling the hole. This will only happen though if the current is not so high that it causes catastrophic breakdown which has not been the case with the sputtered SRELD. In order to prevent catastrophic breakdown, a 100kΩ resister has been placed in series with the device. As a result, pixels have demonstrated self-healing, this work is still in its infancy but initial results have been promising.

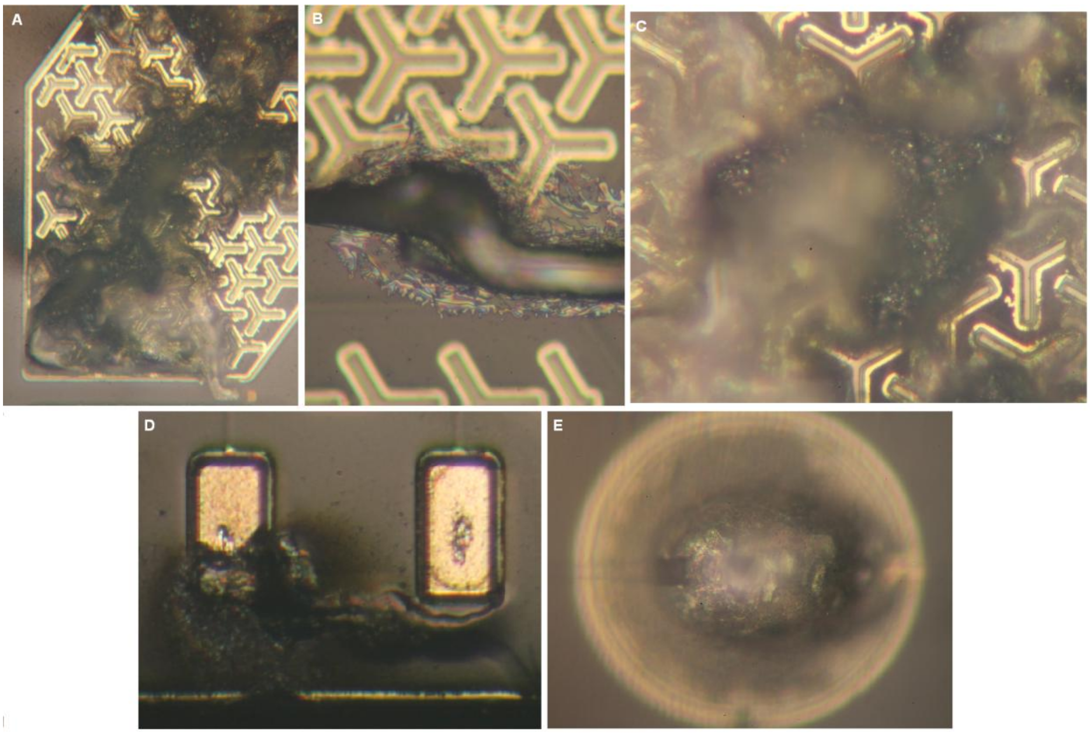

Figure 6.41 - Sputtered SRELD devices failed due to localised destructive breakdown defects.

Photographs A, B and C in Figure 6.41 depict sputtered SRELD pixels that have failed due to LDBD; for all the pixels tested that failed the origin of the failure appears to be the point at which the electrode meets the pixel, the failure then propagates out from this point across the pixel. Photograph D shows the bond pads that are used for addressing the pixels, the area behind the pad has been destroyed and has caused a short to the bottom electrode. Photograph E shows a hole that appeared on the electrode track.

The ALD SRELD pixels suffered from two different types of failure, for the first, whilst the pixel itself did not fail, the failure was in the insulating material around the electrodes. This failure is shown in Figure 6.42 photograph A. As the applied voltage reaches ~ 80Vp-p above the threshold voltage, the surrounding pixels of that currently being driven also begin to emit light. As the voltage is increased further this undesired effect propagates across the device resulting in all 28 pixels emitting light. This failure affected all of the designs with design 2 seemingly more susceptible to it. This issue occurred more frequently when using a 100Hz driving frequency subsequently this route of investigation was dropped. The second type of failure, shown in photograph B, is due to the deterioration of the insulator – semiconductor interfaces (110). The discolouration of the pixel and the way in which it was observed to have started on the edge and then gradually spread to a larger area are the fingerprints of this type of failure.

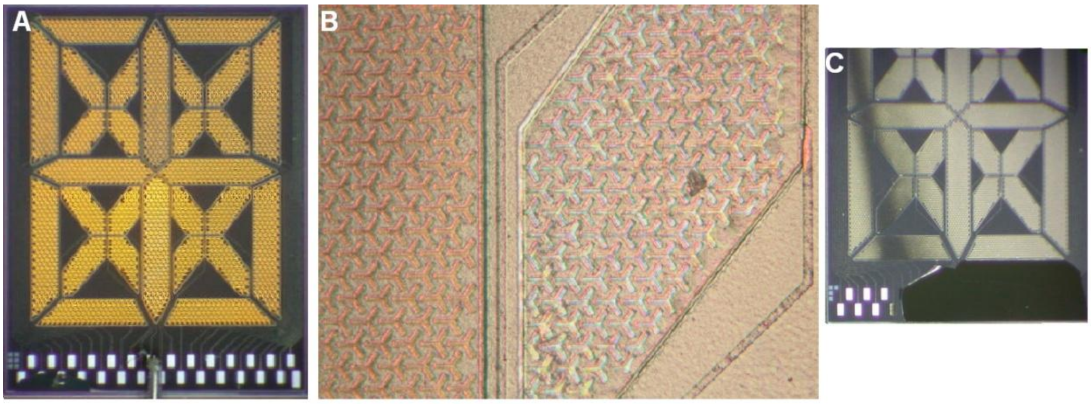

Figure 6.42 - Failed ALD SRELD devices.

Photograph A in Figure 6.42 demonstrates the failure of all the pixels emitting light when only a single pixel is being probed; in this case the lower centre pixel. Photograph B shows the discolouration of the failed pixel (pixel on the right) and photograph C shows a device that has begun to delaminate with the majority of the bond pads missing.

6.7 Conclusion

The effect the burn-in parameters have on the aging and lifetime of LETFEL displays has been presented. An investigation focusing on the time delay between each voltage increment and the size of that voltage increment has been carried out and reported upon. An optimum micro-mirror design, from the six available, has been identified and suggestions of possible improvements to this have been made.

The optimum micro-mirror design for the ALD SRELD devices was found to be design six, in which the three pointed star design legs were twice as long as the other five designs. This design yielded the highest luminance as well as the longest lifetime, but did not always produce the best aging characteristics. Results indicate that the pullback has a large effect on the luminance of the pixel, with increasing pullback resulting in lower luminance levels hence the suggestion of a smaller pullback for design 6 from 1.5µm to 0.5µm. The sputtered SRELD did not demonstrate the same trends as the ALD devices with all the designs having a similar luminance level and design six having the shortest lifetime. More work, however, is required with these devices in order to optimise the burn-in parameters, firstly in order to reduce the risk of LDBD and secondly to improve the lifetime. There is also work to be carried out with the use of a current limiting resistor in series in order to prevent failure.

Altering the burn-in parameters of the ALD LEFTEL pixels resulted in differences to the aging and lifetime characteristics. These differences varied depending upon the micro-mirror design with design six seeing the most variation. A 4Vp-p increment every 5 seconds was found to be the optimum parameters of those tested. This investigation was then taken a step further and concentrating on a single design the time and voltage were altered. This resulted in optimum parameters of 10Vp-p 20 seconds; the 5Vp-p 20 seconds has been omitted due to instability. Whilst these parameters did not result in a better performance than for the design six 4Vp-p 5 seconds, they did improve on the best previous design one performance by almost 50%. Further investigation into the waveform used and its affect when used for just a 6 hour burn-in period showed no improvement to the lifetime of the pixel. This still requires further investigation as the different waveforms may have different optimum parameters.

The modes of failure have been identified. For the sputtered devices a possible prevention method has been identified as well as the need to continue to optimise the burn-in parameters. The issues with the deterioration of the insulator – semiconductor interfaces could be due to poor layer adhesion as has already been seen with the delamination of large areas of devices. The delamination is believed to have been caused by low substrate temperature during deposition. The layer adhesion could be improved with rougher surfaces.

The work carried out in this chapter highlights the difference small changes in the burn-in parameters can make to the lifetime of a display. It has demonstrated that it is not the overall time taken to burn the device in but the voltage and step time parameters that are the important factor.

7. Conclusions and Future Work

7.1 Introduction

The main aim of this research project was to investigate the effects that the burn-in parameters have on the aging and lifetime of LETFEL devices and ACTFEL devices that had been subjected to post deposition laser annealing. In order to achieve this aim the first step was to determine the methods and techniques that were required and implement them into the pre-existing systems. Once this had been achieved the use of excimer laser processing as a post deposition heat treatment for ACTFEL devices grown by HiTUS deposition was investigated. This followed with a study into the feasibility of using a new wavelength to process thin film ZnS:Mn phosphor layers in order to increase the luminescent output. Finally an investigation into the effects of the burn-in parameters on the lifetime and aging characteristics of LETFEL devices was undertaken.

7.2 Achievements

This body of work has presented the successful results obtained during the investigation into the lifetime and aging of LETFEL displays, as well as the feasibility of laser annealing at 193nm and the use of laser annealing as a post deposition annealing method for temperature sensitive substrates. This work was carried out in order to aid in the development of novel TFEL structures and deposition and processing methods. The main achievements of this research project are summarised below.

7.2.1 ArF Laser Annealing

ZnS:Mn thin films have been successfully laser annealed using a previously unreported wavelength of 193nm. RF magnetron sputtered devices were subjected to fluences of 0.3, 0.5, 0.7, 0.9 and 1.1J/cm^2 for single and double laser irradiations. The optimum laser annealing conditions for ArF irradiation followed by thermal annealing was found to be a single pulse at 1.1J/cm^2, this gave the best performance in regards to the luminance and sharpness of the turn-on. These devices could be compared directly to those processed by KrF laser annealing followed by thermal annealing as they had been deposited on the same wafer. Whilst the maximum achievable luminance of the KrF devices was 10.5% higher than that of the ArF devices the turn-on slope was much shallower. This meant that when the devices were driven at an operational voltage of 450Vp-p the best ArF device would be 40% brighter than the equivalent KrF device, which was found to be a single pulse at 1.1J/cm2. With regards to the devices that were laser annealed only the two wavelengths yielded an almost similar maximum achievable luminance of 259cd/m^2 for the KrF and 265cd/m^2 for the ArF under the same conditions as the laser followed by thermal annealing devices.

7.2.2 Demonstrated the Feasibility of Laser Annealing Temperature Sensitive Substrates

The use of KrF laser annealing as a post deposition heat treatment of ACTFEL devices deposited at room temperature on temperature sensitive substrates, glass and plastic, has been demonstrated. The ACFTEL devices have been fabricated by HiTUS deposition at room temperature and have not been subjected to any thermal heat treatment. Laser annealing at 1J/cm^2 of the devices deposited on plastic resulted in an increase in luminance, from the as deposited device, of over 1500% from 17cd/m^2 to 281cd/m^2 when driven at 500Vp-p. The results for the devices deposited on glass were not as good but a 1400% increase in luminance from the as deposited device was still achieved when laser annealed at 1.37J/cm^2. These results are very promising and demonstrate the feasibility of producing bright, transparent flexible displays when combining the two processes of HiTUS deposition and laser annealing. It is possible that the shallow turn-on could be improved by laser annealing at 193nm.

7.2.3 Optimisation of LETFEL Displays

Laterally emitting thin film electroluminescent devices fabricated using ALD have been optimised in regards to their aging characteristics and lifetimes. Six different LETFEL designs were subjected to differing step time increments in order to determine an optimum micro-mirror design and also to optimise the drive parameters of the pixels in order to prolong their lifetime and reduce the effects of aging on the L-V curves. Design six, as described in section 6.1, was found to be the preferred device due to its long lifetime, which was more than double what was achieved by its closest rival. These initial tests showed the optimum step time interval to be 5 seconds, this along with a 4Vp-p increment and driven using a 1kHz trapezoidal waveform, these parameters ultimately turned out to produce the best lifetime of all the different parameters that were trailed. These studies demonstrated that the smallest change to the burn-in parameters can alter the lifetime and aging of a pixel and have taken a step towards optimising them in order to prolong the life of the pixel and stabilise its aging quicker.

7.3 Future Work

There are several paths in which this research can be continued as in many ways it has only just begun. Whilst identifying the optimal design and burn-in parameters of LETFEL devices was a key aim of this study any future work may benefit from using a simpler design structure.

7.3.1 Continuation of LETFEL Burn-in Parameters Optimisation

Whilst an optimum set of parameters has been found for the burn-in of LETFEL devices they have been found from a limited trial due to the time constraints of the nature of the work as well restricted equipment. There are still vast combinations of step time intervals and voltage increments that have yet to be tried along with the continuation of the work using different waveforms. The burn-in period of 6 hours could be extended as the luminance for the square and triangular waveforms was still increasing at the end of this period. The frequency of the waveform could be altered; this was attempted but resulted in failure in which neighbouring pixels also began to emit light. The effect of burning devices in under vacuum is another possibility as well as the alteration of the temperature.

7.3.2 Lifetime and Aging Studies of Laser Annealed ACTFEL Displays

Due to the failure of the ITO top electrode it was not possible to carry out any lifetime studies on laser annealed devices. An initial trial (93) carried out as part of another study showed that laser followed by thermal annealing can extend the lifetime of a device. Only a single device was tested so this could be extended to include both laser wavelengths used during this research as well as various fluences and number of pulses and also devices laser annealed and laser followed by thermal annealing. This would achieve a comprehensive study in order to find the optimum laser treatment in regards to luminescent properties and lifetime. The issue regarding the failure of the ITO could be overcome by combining an ITO electrode with an overlapping aluminium electrode and covering the ITO with protective silicon.

7.3.3 Investigation into the Effects of Combined Laser wavelengths for ACTFEL Devices

The results obtained from the comparative study of ArF and KrF laser annealing demonstrated that both wavelengths had their advantages, KrF produced higher maximum achievable luminance whilst ArF demonstrated better performances at lower voltages, around the range that a device would be driven at for operation. A combination of laser wavelengths could be investigated in regards to their luminescent properties and lifetime. Successive laser irradiations of different wavelengths and fluences could be applied to various devices grown by either HiTUS on temperature sensitive substrates or by RF magnetron sputtering on Si wafers to investigate whether the dual wavelengths would produce a device with sharp turn-on characteristics and high luminance. An ablation study in a similar vain to what Mastio (98) carried out for 248nm is required for both 193nm and for the effects of the combined wavelengths.

7.3.4 Extended Aging Period and Accelerated Aging

Whilst the three day aging period used was sufficient to show any trends that emerged from the alteration of the burn-in parameters the lifetime was a predicted one from the data obtained and assumed to continue to decay at the same rate. The use of a longer period or until the device has actually reached its lifetime could be used as it would give a more accurate picture of the aging of a device. This investigation could be used as part of a study into the use of accelerated aging and determining the parameters required in order to rapidly burn-in or age a device to reduce the time required for the device to stabilise.

7.3.5 Alternative Device Structures

The methods and protocols used during this research project could be used to characterise alternative device structures to aid in understanding the device operation and potentially how to improve it further. One such potential structure uses barrier layers within the phosphor and has shown to improve device performance (111).

7.3.6 RF Magnetron Sputtered SRELD Optimisation

The LETFEL devices that have been used as part of this study that have been deposited using RF magnetron sputtering suffered from poor lifetimes as they failed due to LDBD. The optimisation of the burn-in parameters can aid in preventing this form of failure, they have already been optimised in order to generate an L-V curve, unfortunately these are not adequate in order to promote a long lifetime. Further work is required in order to prevent failure, this would focus on two areas, the first being further optimisation of the burn-in parameters, the second being the use of a series resistor in order to limit current and prevent the catastrophic breakdown associated with LDBD.

References

1. Castellano JA. *Flat panel display handbook*. Third Edition ed. Stanford Resources; 2001.

2. Mastio EA, Cranton WM, Thomas CB. *KrF laser annealing of ZnS:Mn thin film phosphors*. 1999.

3. Cranton WM. *Emissive displays*. In press 2006.

4. Bender JP. *Manufacture and characterization of novel ACTFEL materials and devices* [dissertation]. Oregon State University; 2003.

5. Fischer AG, Shrader RE, Larach S. *Luminescence of solids (with emphasis on electroluminecence)*. In: *Photoelectronic materials and devices*. New york: D.Van Nostrand Company, Inc.; 1965. p 1.

6. Wiedermann E. *Uber fluorescenz und phosphorescenz*. Annalen der Physik and Chemie. 1888;34:446.

7. Shionoya S. *Phosphor handbook*. CRC Press; 1999.

8. Pankove JJ. *Electroluminescence*. Springer-Verlag; 1977.

9. Ono YA. *Electroluminescent displays*. World Scientific Publishing Co. Pte. Ltd; 1995.

10. Round HJ. Electrical World. 1907;19:309.

11. Destriau G. *Reserches sur les scintillations des zinc aux rayons*. Journal de Chemie Physique. 1936;33:587.

12. Vlasenko NA, Popkov YA. *The electroluminescence of sublimate phosphor ZnS:Mn*. Optika i Spektroskopiya. 1960;8:81.

13. Cranton WM, Koutsogeorgis DC, Liew S, Nassuna B, Ranson R, Thomas CB. *Laser processing of thin film phoshors for flat screen displays*. 2002.

14. Allison J. Electronic engineering semiconductors and devices. 2nd ed. McGraw-Hill Book Company; 1990.

15. Vincent G, Chantre A, Bois D. *Electric field effect on the thermal emission of traps in semicondutor junctions*. Journal of Applied Physics. 1979;50:5484.

16. Boutaud G. *Private communication*. 2009.

17. Russ MJ, Kennedy DI. *The effects of double insulating layers on the electroluminescence of evaporated ZnS:Mn films*. Journal of the Electrochemical Society. 1967;114:1066.

18. Inoguchi T, Takeda M, Yakihara Y, Nakata Y, Yoshida M. *Stable high-brightness thin-film electroluminescent devices*. Proceedings of the S.I.D. 1974(74):84.

19. Thomas CB, Stevens R, Cranton WM. *Laterally emitting TFEL for head mounted displays*. 1996 SID International Symposium. Digest of Technical Papers. First Edition. 1996:365.

20. Thomas CB, Cranton WM, McClean IP, Craven MR, Abdullah AH. *Laterally emiiting TFEL display devices*. Society for Imformation Display International Symposium. 1995:887.

21. Cranton WM. *Growth and characterisation of ZnS:Mn based latterally emitting thin film electroluminescent device structures* [dissertation]. University of Bradford; 1995.

22. Smith DH. *Modeling a.c. thin-film electroluminescent devices*. Journal of Luminescence. 1981;23:209.

23. Stevens R, Cranton WM, Thomas CB, inventors; *Laterally transmitting thin film electroluminescent device*. United States patent 5910706. 1999 .

24. Stevens R. University of Bradford; 1994.

25. Stevens R, Thomas CB, Cranton WM. *Enhancing the brightness of thin-film electroluminescent displays by improving the emission process*. IEEE Electron Device Letters. 1994;15:97.

26. Cranton WM, Thomas CB. *Material processing for thin film electroluminescent displays*. Microdisplay 2001 SID. 2001:102.

27. Alt PM. Proceedings of the S.I.D. 1984;35:123.

28. Sethu M. *Performance studies of thin film electroluminescent (TFEL) devices* [dissertation]. Nottingham Trent University; 2002.

29. Hitt J, Wager JF. *Insulator issues in alternating-current thin-film electroluminescent devices*. Journal of Applied Physics. 2001;90(6):2711.

30. Baukol B. *Alternating-current thin-film electroluminescent device fabrication and characterization* [dissertation]. Oregon State University; 2001.

31. Krasnov AN. *Selection of dielectrics for alternating-current thin-film electroluminescent device*. Thin Solid Films. 1999 6/22;347(1–2):1.

32. Craven MR, Cranton WM, Toal S, Reehal HS. *Characterisation of BaTiO3 thin films deposited by RF magnetron sputtering for use in a.c TFEL devices.*. Semiconductor Science and Technology. 1998;13:404.

33. Liu M, He G, Zhu LQ, Fang Q, Li GH, Zhang LD. *Microstructure and interfacial properties of HfO_2–Al_2O_3 nanolaminate films*. Applied Surface Science, 2006 7/15;252(18):6206.

34. Wilk GD, Wallace RM, Anthony JM. *High-k gate dielectrics: Current status and material properties considerations*. Journal of Applied Physics. 2001;89:5243.

35. Balog M, Schieber M, Michman M, Patai S. *Chemical vapour deposition and characterisation of HfO2 films from organo-hafnium compounds*. Thin Solid Films. 1977;41(3):247.

36. Boutaud G. *Growth optimisation and laser processing of thin film phosphors for electroluminescent displays* [dissertation]. Nottingham Trent University; 2010.

37. George SM, Ott AW, Klaus JW. *Surface chemistry for atomic layer growth*. Journal of Physical Chemistry. 1996;100:13121.

38. Vlasenko NA, Kononets YF, Denisova ZL, Kopytko YV, Veligura LI, Soinined EL, et al. *Aging of ZnS:Mn thin-film electroluminescent devices grown by two different atomic layer epitaxy processes*. Semiconductor Physics, Quantum Electronics and Optoelectronics. 2001;4:48.

39. Tanninen V-, Oikkonen M, Tuomi TO. *Comparative study of the crystal phase, crystallite size and microstrain in electroluminescent ZnS:Mn films grown by atomic layer epitaxy and electron beam evaporation*. Thin Solid Films. 1983;109:283.

40. Hakansson M, Helin M, Putkonen M, Jiang Q, Kotiranta M, Suomi J, et al. *Electrochemiluminescence of tb(III) chelates at optically transparent tunnel emission electrodes fabricated by atomic layer deposition*. Analytica Chimica Acta. 2005;541:137.

41. Morgan DV, Board K. *An introduction to semiconductor microtechnology*. John Wiley & Son Ltd; 1990.

42. Ko K-, Lee YK, Do YR, Huh Y-. *Structural effect of a two-dimensional SiO_2 photonic crystal layer on extraction efficiency in sputter-deposited Y_2O_3:Eu^{3+} thin-film phosphors*. Journal of Applied Physics. 2007;102:13509.

43. Mastio EA. *Materials engineering for high efficiency thin film electroluminescent devices* [dissertation]. Nottingham Trent Univerity; 1999.

44. Koutsogeorgis DC. *Investigation of laser annealing of thin film phosphors for potential luminescent devices* [dissertation]. Nottingham Trent University; 2003.

45. Poate JM, Mayer JW. *Laser annealing of semiconductors*. Academic Press Inc; 1982.

46. Reehal HS, Gallego JM, Edwards CB. *Pulsed XeCl laser annealing of ZnS:Mn thin films*. Applied Physics Letters. 1982;40(3):258.

47. Reehal HS, Thomas CB, Gallego JM, Hawkins G, Edwards CB. *Pulsed UV laser irradiation of ZnS films on si and GaAs*. *Laser-solid interactions and transient thermal processing of materials*; 1982.

48. Gallego JM, Reehal HS, Thomas CB. *DC electroluminescence*. SID proceedings; 1983.

49. Koutsogeorgis DC, Mastio EA, Cranton WM, Thomas CB. *Pulsed KrF laser annealing of ZnS:Mn laterally emitting thin film electroluminescent displays*. Thin Solid Films. 2001 2/15;383(1-2):31.

50. Mastio EA, Cranton WM, Thomas CB, Fogarassy E, de Unamuno S. *Pulsed KrF laser annealing of RF sputtered ZnS:Mn thin films*. Appl Surf Sci. 1999 1;138-139:35.

51. Mastio EA, Cranton WM, Thomas CB. *Pulsed laser annealing for high-efficiency thin film electroluminescent devices*. J Appl Phys. 2000 08;88(3):1606.

52. Reehal HS, Edwards CB. *Annual report laser facility committee*. Rutherford Appleton Labs; 1981.

53. Mastio EA, Thomas CB, Cranton WM, Fogarassy E. *The effects of multiple KrF laser irradiations on the electroluminescence and photoluminescence of rf-sputtered ZnS:Mn-based electroluminescent thin film devices*. Appl Surf Sci. 2000 3;157(1-2):74.

54. Koutsogeorgis DC. *Private communication*. 2012.

55. Ihanus J, Lankinen MP, Kemell M, Ritala M, Leskelä M. *Aging of electroluminescent ZnS:Mn thin films deposited by atomic layer deposition processes*. Journal of Applied Physics. 2005 12;98(11):113526.

56. Tornqvist R, Korpela S. *On the aging of ZnS:Mn electroluminescent thin films grown by the atomic layer epitaxy technique*. Journal of Crystal Growth, 1982;59:395.

57. Taniguchi K, Tanaka K, Ogura T, Kakihara Y, Nakajima S, Inoguchi T. *Proceeding of the 4th display research conference*. *SID84 digest*; 1984; Paris. Los Angeles: SID; 1984.

58. Howard WE, Sahni O, Alt PM. *A simple model for the hysteretic behavior of ZnS:Mn thin film electroluminescent devices*. Journal of Applied Physics. 1982;53:639.

59. Goldenblum A, Oprea A, Bogatu V. *Time behavior of currents in ZnS:Mn metal-insulator-semiconductor-insulator-metal structures*. Journal of Applied Physics 1994 05/15;75(10):5177.

60. Neyts KA, Corlatan D, De Visschere P, Van den Bossche J. *Observation and simulation of space-charge effects and hysteresis in ZnS:Mn ac thin-film electroluminescent devices*. Journal of Applied Physics. 1994;75:5339.

61. Shih S, Keir PD, Wager JF, Viljanen J. *Space charge generation in ZnS:Mn alternating-current thin-film electroluminescent devices*. Journal of Applied Physics 1995 11;78(9):5775.

62. Keir PD, Ang WM, Wager JF. *Modeling space charge in alternating-current thin-film electroluminescent devices using a single-sheet charge model*. Journal of Applied Physics 1995 10;78(7):4668.

63. Bringuier E. *Charge transfer in ZnS-type electroluminescence*. Journal of Applied Physics 1989 8;66(3):1314.

64. Bringuier E. *Tentative anatomy of ZnS-type electroluminescence*. Journal of Applied Physics 1994 5;75(9):4291.

65. Soenen B, Van den Bossche J, De Visschere P. *Kinetics and aging in atomic layer epitaxy ZnS:Mn ac thin-film electroluminescent devices*. Journal of Applied Physics 1997 11/15;82(10):5241.

66. Alt PM, Dove DB, Howard WE. *Experimental results on the stability of ac thin-film electroluminescent devices*. Journal of Applied Physics. 1982;53:5186.

67. Wang CW, Sheu TJ, Su YK, Yokoyama M. *The study of aging mechanism in ZnS:Mn thin-film electroluminescent devices grown by MOCVD*. Applied Surface Science. 1997;113/114:709.

68. Khormaei I, Wager JF, King CN. *Improved stability of ZnS:Mn ACTFEL devices*. *SID89 digest*; 1989; Baltimore. SID; 1989.

69. Mikami A, Terada K, Okibayashi K, Tanaka K, Yoshida M, Nakajima S. *Aging characteristics of ZnS:Mn electroluminescent films grown by a chemical vapor deposition technique*. Journal of Applied Physics 1992 07/15;72(2):773.

70. Flegal RT, King CN. *Differential aging effects in ACTFEL displays*. SID 86 Digest. 1986:177.

71. Soenen B, Neyts K, Van den Bossche J, De Visschere P. *Aging of ZnS:Mn ALE ac thin-film electroluminescent devices*. Journal for the Society of Information Display. 1996;4:319.

72. Krasnov AN, Bender JP, Kim WY. *Increased luminance of ZnS/mn thin-film electroluminescent displays due to ag co-doping*. Thin Solid Films. 2004 11/22;467(1–2):247.

73. Singh VP, Krishna S, Morton DC. *Electric field and conduction current in ac thin-film electroluminescent display devices*. Journal of Applied Physics 1991 8;70(3):1811.

74. Ono YA, Kawakami H, Fuyama M, Onisawa K. *Transferred charge in the active layer and EL device characteristics of TFEL cells*. Japanesse Journal of Applied Physics. 1987;26:1482.

75. Shih S, Keir PD, Hitt J, Wager JF. *Offset of the electrical characteristics of alternating-current thin-film electroluminescent devices*. Appl Phys Lett. 1996 09/23;69(13):1921.

76. Davidson JD, Wager JF, Khormaei RI, King CN, Williams R. *Electrical characterization and modeling of alternating-current thin-film electroluminescent devices*. Electron Devices, IEEE Transactions on. 1992;39(5):1122.

77. McArthur RC, Davidson JD, Wager JF, Khormaei I, King CN. *Capacitance-voltage characteristics of alternating-current thin-film electroluminescent devices*. Appl Phys Lett. 1990 05/07;56(19):1889.

78. Wager JF, Douglas AA, Morton DC. *Electrical characterization and modeling of ACTFEL devices*.

79. Wager JF, Keir PD. *Electrical characterization of thin-film electroluminescent devices*. Annual Review of Materials Science. 1997 08;27(1):223.

80. Benoit J, Barthou C, Benalloul P, Polamo K. *The electro-optical behavior of SrS:Ce electroluminescent devices under photonic excitation*. Journal of Applied Physics. 2000;87:198.

81. Wagner FX, Dhese PH, Key PH, Sands D, Jackson SR, Kirbitson R, et al. *Photo-luminesence of pulsed excimer laser annealed sb-implanted CdTe*. Applied Surface Science. 1995;86:364.

82. Miller TC. *Private communication*. 2009.

83. Hurd JM, King CN. *Physical and electrical characterization of co-deposited ZnS:Mn electroluminescent thin film structures*. Journal of Electronic Materials. 1979;8:879.

84. Mitra S, editor. *Sample preparation techniques in analytical chemistry*. John Wiley and Sons; 2003.

85. Williams DB, Carter CB. *Transmission electron microscopy: A textbook for materials science*. Kluwer Academic / Plenum Publishers; 1996.

86. Wilson SL. *Laser processing of inkjet printed and RF magnetron sputtered* SnO_2*:Sb* [dissertation]. Nottingham Trent University; 2008.

87. Runyan WR, Shaffner TJ. *Semiconductor measurements &instrumentation*. 2nd edition ed. McGraw-Hill Professional; 1998.

88. Koutsogeorgis DC, Cranton WM, Thomas CB, Hirst G, Shaikh W. *Laser annealing of micro-mirror based thin film electroluminescent devices*. 2000.

89. McClean IP, Konofaos N, Thomas CB. *Conductance technique measurements of the density of states between si and ZnS grown by molecular beam epitaxy*. Journal of Applied Physics. 1993;74:397.

90. Nakanishi Y, Mori S, Nakamura T, Tatsuoka H, Kuwabara H, Hatanaka Y. *Effect of insulating layer structural properties for thin-film electroluminescent devices*. Materials Chemistry and Physics. 1996;43:292.

91. Fuh A, Gallinger RP, Shuster P, Adolph J, Caporaletti O. *The effects of post-deposition annealing on ZnS:Mn film crystalline structure and electroluminecent characteristics*. Thin Solid Films. 1992;207(1-2):202.

92. Cranton WM, Stevens R, Thomas CB, Abdullah AH, Craven MR. *Improving the efficiency of thin film electroluminescent displays.*. IEE colloquium on materials for displays; 1995; London. ; 1995.

93. Koutsogeorgis DC, Cranton WM, Ranson R, Thomas CB. *Performance enhancement of ZnS:Mn thin film electroluminescent devices by combination of laser and thermal annealing*. Journal of Alloys and Compounds,. 2009;483:526.

94. Wakeham SJ, Tsakonas C, Cranton WM, Thwaites MJ, Boutaud G, Koutsogeorgis DC. *Laser annealing of thin film electroluminescent devices deposited at a high rate using high target utilization sputtering*. Semiconductor Science and Technology. 2011;26(4):045016.

95. Zeinert A, Benalloul P, Benoit J, Barthou C, Dreyhsig J, Gumlich H-. *On the excitation efficiency in ZnS:Mn thin-film electroluminecent devices*. Journal of Applied Physics. 1992;71:2855.

96. Cranton WM. *Private communication*. 2012.

97. Mitrofanov O, Manfra M. *Poole-frenkel electron emission from the traps in AlGaN/GaN transistors*. Journal of Applied Physics. 2004;95:6414.

98. Mastio EA, Fogarassy E, Cranton WM, Thomas CB. *Ablation study on pulsed KrF laser annealed electroluminescent ZnS:Mn/Y2O3 multilayers deposited on si*. Appl Surf Sci. 2000 2/1;154-155:35.

99. Mastio EA, Craven MR, Cranton WM, Thomas CB, Robino M, Fogarassy E. *The effects of KrF pulsed laser and thermal annealing on the crystallinity and surface morphology of radiofrequency magnetron sputtered ZnS:Mn thin films deposited on si*. Journal of Applied Physics. 1999;83:2562.

100. Wakeham SJ, Thwaites MJ, Holton BW, Tsakonas C, Cranton WM, Koutsogeorgis DC, et al. *Low temperature remote plasma sputtering of indium tin oxide flexible display applications*. Thin Solid Films. 2009;518:1355.

101. Wakeham SJ, Thwaites MJ, Tsakonas C, Cranton WM, Ranson R, Boutaud G, et al. *A new reactive sputtering technique for the low temperature deposition of transparent light emitting ZnS:Mn thin films*. Physica Status Solidi (A). 2010;207(7):1614.

102. Farrow C. *Transfer report*. In press 2009.

103. Ono YA. *Different techniques employed in deposition of TFEL devices*. Acta Polytech Scand Appl Phys Ser. 1990:41.

104. Rudiger J. *Feasability of laterally emitting thin film electroluminecence devices as an application specfic integrated display* [dissertation]. Nottingham Trent University; 2008.

105. Stevens R. *SRELD quarterly technical report*. Rutherford Appleton Laboratory; 2006.

106. Alt PM, Dove DB, Howard WE. *AC thin film electroluminescent device stability*. 1982 International Display Research Conference. 1982:55.

107. Abu-Dayah A, Wager JF, Kobayashi S. *Electrical characterization of atomic layer epitaxy ZnS:Mn alternating-current thin-film electroluminescent devices subject to various waveforms*. Journal of Applied Physics 1993 11;74(9):5575.

108. Douglas AA, Wager JF, Morton DC, Koh JB, Hogh CP. *Evidence for space charge in atomic layer epitaxy ZnS:Mn alternating-current thin-film electroluminescent devices*. Journal of Applied Physics. 1993;73(1):296.

109. Abu-Dayah A, Wager JF. *Aging studies of atomic layer epitaxy ZnS:Mn alternating-current thin-film electroluminescent devices*. Journal of Applied Physics 1994 4;75(7):3593.

110. Krasnov AN. *Alternating-current thin-film electro-luminescent devices: Effect of fabrication conditions on aging and failure defect formation*. Progress in Crystal Growth and Characterization of Materials. 1998;37(2–3):123.

111. Thomas CB, Cranton WM. *High efficiency ZnS:Mn ac thin film electroluminescent device structure*. Appl Phys Lett. 1993 12/06;63(23):3119.